Validation, Analysis of Annual Cycle, and Biogenic Sequestration of CO_2, and Modulation of CH_4

A Dissertation Presented to
the Faculty of the Department of Earth and Atmospheric Sciences
University of Houston

In Partial Fulfillment
of the Requirements for the Degree
Doctor of Philosophy

By

Abigail Corbett

May 2018

Validation, Analysis of Annual Cycle, and Biogenic Sequestration of CO_2, and Modulation of CH_4

Abigail Corbett

APPROVED:

Dr. Xun Jiang (EAS), Chairman

Dr. Liming Li (Physics), Co-Chairman

Dr. Robert Talbot (EAS)

Dr. Yunsoo Choi (EAS)

Dean, College of Natural Sciences and Mathematics

ACKNOWLEDGEMENTS

First, I would like to acknowledge and greatly thank Dr. Jiang and Dr. Li for their unwavering support and wisdom throughout my studies and research in the Earth and Atmospheric Sciences Department. Their vast experience and limitless patience was unrivaled. I could not of completed such a comprehensive dissertation, nor had as much success throughout my time as a Ph. D. student, without their advise, support, and over all helpfulness. Additionally, I thank my committee, Dr. Choi and Dr. Talbot, and also our research group, Jason La and Aaron Studwell, for their advice and guidance during my research.

Second, I would like to thank and acknowledge my parents, Sharon and David Corbett, whose support and own academic and professional accomplishments inspire and continue to encourage me. I know having a daughter in school for this long was draining financially, emotionally, and, at some points, even physically; however, you never stopped supporting and encouraging me to make the most of all opportunities. I'd also like to thank my sisters, Emma and Lauren, and brother-in-laws, Nathan and Max, who encouraged me and supported me in a way only siblings can throughout my studies. Finally, a few honorable mentions (in no particular order): Katelyn, Kristin, and Noodle.

This project is supported by NASA grants NNX13AC04G, NNX13AK34G, NNX16AG46G, and NNX15AI85G.

Validation, Analysis of Annual Cycle, and Biogenic Sequestration of CO_2, and Modulation of CH_4

An Abstract of a Dissertation
Presented to
the Faculty of the Department of Earth and Atmospheric Sciences
University of Houston

In Partial Fulfillment
of the Requirements for the Degree
Doctor of Philosophy

By

Abigail Corbett

May 2018

Abstract

Greenhouse gases, such as carbon dioxide (CO_2) and methane (CH_4), play a critical role in the processes of global warming and climate change. Retrieved CO_2 from satellites (e.g., OCO-2, GOSAT, AIRS, TES) offer a fresh opportunity to understand the variability of CO_2 over the global domain that was unattainable before due to sparse *in situ* measurements. First, two innovative satellite data sets, Orbiting Carbon Observatory (OCO-2) and Greenhouse Gases Observing Satellite (GOSAT), which have vertical sensitivities in the lower atmosphere were compared, with ground-based measurements to validate the new retrievals. This established that the GOSAT and OCO-2 CO_2 data sets are close to the *in situ* measurements. The overall GOSAT CO_2 uncertainty was -0.63 ppm; whereas, OCO-2 uncertainty was 0.23 ppm. Second, the long-term trend and annual variability of CO_2 using satellite retrievals were explored. A multiple regression method was used to estimate CO_2 seasonal cycle from the satellite CO_2 retrievals and *in situ* CO_2 measurements to better understand surface, mid-tropospheric, and column CO_2 seasonal cycles. Third, novel satellite-retrieved Solar-induced Fluorescence (SIF) datasets were studied to investigate the contributions of the biosphere to CO_2. This analysis allows for a better understanding of how the biosphere acts as a source and also a sink for global CO_2, yielding a better understanding of the CO_2 global cycle. An inverse relationship was found between atmospheric CO_2 and SIF. During each hemisphere's summer season, SIF values are high because there is more photosynthesis, which leads to a low levels of atmospheric CO_2. Finally, the influence of El Niño-Southern Oscillation on mid-

tropospheric methane was studied. Enhanced rising air in the central Pacific during El Niño months advects lower surface concentrations of CH_4 over the ocean to the middle troposphere, with less CH_4 over the central Pacific than the western Pacific. Furthermore, rising air can transport low surface concentrations of CH_4 to the middle troposphere over the western Pacific in La Niña months, contributing to lower CH_4 concentrations over the western Pacific than the central Pacific during La Niña months.

Table of Contents

List of Figures

PAGE

List of Tables

PAGE

Chapter 1: Introduction

Carbon dioxide (CO_2) is an important greenhouse gas that has great warming potential [*Dickinson and Cicerone,* 1986]. Human activities, including fossil fuel combustion and land use change, are anthropogenic sources of atmospheric CO_2. On average, about 40% of these anthropogenic emissions stay in the atmosphere, while the oceans and terrestrial biosphere absorb the remaining 60% of the anthropogenic CO_2 emissions [*Le Quere et al*., 2002]. Anthropogenic CO_2 emissions contribute to the positive trend in atmospheric CO_2, which has been increasing at about 2 ppm (parts per million) per year from pre-industrial level of 280 ppm to more than 388 ppm, as of June 2010 [*Keeling et al*., 1995; *Sarmiento and Wofsy*, 1999; *Tans and Keeling*, 2014]. The increasing atmospheric CO_2 concentration will have serious impacts on global warming and therefore, global climates, habitats and societies, due to an increase of 1.66 ± 0.17 Wm^{-2} global radiative forcing resulting from the increased CO_2 concentration [*Forster et al*., 2007]. Atmospheric CO_2 also has an annual cycle that reflects the interaction of the biosphere [*Pearman and Hyson*, 1980, 1981; *Cleveland et al*., 1983; *Bacastow et al*., 1985; *Keeling et al*., 1996; *Buermann et al*., 2007]. This annual cycle due to vegetation uptake and release is seen in greater amplitudes in the Northern Hemisphere than the Southern Hemisphere [*Pearman and Hyson*, 1980].

Atmospheric CO_2 also demonstrates intra-seasonal and inter-annual variability, in addition to the seasonal cycle and positive trend [*Bacastow*, 1976;

Enting, 1987; *Feely et al.*, 1987; *Keeling and Revelle*, 1985; *Keeling et al.*, 1995; *Dargaville et al.*, 2000; *Dettinger and Ghil*, 1998; *Keppel-Aleks et al*., 2011; *Wang et al.*, 2011; *Jiang et al.*, 2013]. Recent studies have even suggested that certain atmospheric processes have an effect on the temporal variability of atmospheric CO_2 [*Li et al.*, 2010; *Jiang et al*., 2010; *Wang et al*., 2011; *Jiang et al.*, 2012; *Jiang et al*. 2013]. In these studies, satellite and *in situ* CO_2 observations were combined with model simulations. It was found the Madden-Julian Oscillation (MJO) and semi-annual oscillation (SAO) signals could influence CO_2 concentrations in the middle troposphere [*Li et al.*, 2010; *Jiang et al.*, 2012; *Li*, 2018]. Jiang et al. (2011) studied the SAO signal of CO_2 at different latitudes using satellite CO_2 retrievals and found SAO amplitudes decrease with increasing altitudes. Within this work, Jiang et al. demonstrated a relationship between the SAO signal and CO_2 exchange between the biosphere and the atmosphere.

El Niño-Southern Oscillation (ENSO) is an important interannual variability in the tropical region and has important influence on tracers. It is a dominant mode of interannual climate variability observed all over the world [*Philander,* 1990]. and also has environmental and socioeconomic impacts worldwide [*McPhaden et al.,* 2006]. ENSO is also a driving force that modulates rainfall, surface air temperature, river flow, agricultural production, ecosystems, tropical cyclones, and disease [*Ropelewski and Halpert 1987*, 1989; *Allan et al.,* 1996; *Power et al.,* 1998, 1999; *Kahya and Dracup,* 1993; *Merendo,* 1995; *Nicholls,* 1985; *Phillips et al.,* 1998; *Hammer et al.,* 2000; *Holmgren et al.,* 2001; *Nicholls,* 1984; *Solow and Nicholls,* 1990; *McDonnell*

and Holbrook, 2004a,b; *Werner and Holbrook,* 2011; *Werner et al.,* 2011; *Callaghan and Power*, 2012; *Nicholls,* 1993; *Bouma and Dye,* 1997]. ENSO is generally characterized by interannual changes in tropical ocean sea level and temperature. During El Niño events, warm, surface ocean temperatures migrate from the usual location on the western edge of the Pacific to the central Pacific. This movement of warm ocean water changes the location of atmospheric convection from the western edge of the Pacific to the central Pacific, causing a usually single cell convective system to split into two cells with convection in the central Pacific, as shown in Figure 1.

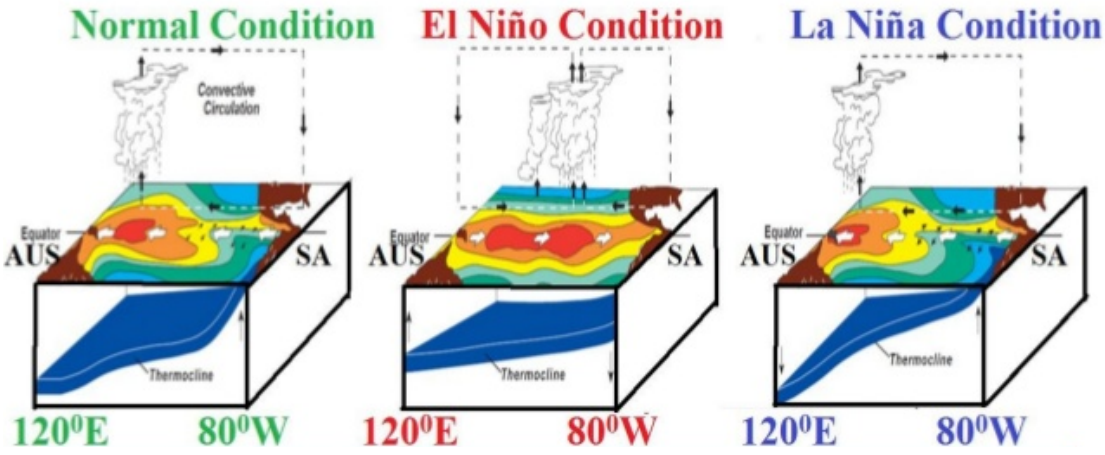

Figure 1. Diagram depicting sea-surface temperatures (on a scale where red equates to warm temperatures and blue to average temperatures), winds, rising air, and the thermocline (shown in royal blue) in the tropical Pacific during El Niño, La Niña and normal events. [NOAA/PMEL/TAO]

Another important greenhouse gas, methane (CH_4), is ~28 times stronger as a greenhouse gas than carbon dioxide and therefore, is a larger contributor to the heating of the atmosphere [*Myhre et al*., 2014; IPCC 2013]. CH_4 plays an important

role in atmospheric chemistry [*Myhre et al*., 2014]. Anthropogenic sources of CH_4 include fossil fuel production and distribution, agriculture and livestock, biomass burning, and landfills, while wetlands are the largest natural source [*Myhre et al*., 2014].

Similar to CO_2, global CH_4 ground-based measurements have been recorded since the early 1980s, but due to the inconsistent spatial grid and extremely difficult measurement conditions, ground-based measurements are limited spatially and cannot adequately represent the global concentrations [*Dlugokencky et al*., 1994]. Additionally, ground-based measurements left many locations all over the globe unmeasured, particularly over oceans [*Dlugokencky et al*., 1994; *Dlugokencky et al*., 1995]. NOAA/GMD operated forty surface measurement stations of CH_4 worldwide, which yielded in a global average CH_4 concentration ~1,774.62±1.22 ppb [*Dlugokencky et al.,* 2005]. Measurements of atmospheric CH_4 concentration suggest that atmospheric CH_4 concentrations have increased over twenty years, however the rate of increase of CH_4 concentration was not constant [*Dlugokencky et al*., 2003].

Global space-borne measurements allow the study of global variations of CO_2 and CH_4 with a better spatial coverage than ever before. Currently, satellites collect global measurements of atmospheric CO_2 with unprecedented precision, spatial resolution, and coverage to characterize CO_2 sources and sinks on regional scales, as well as CO_2 concentration transport around the world [*Yokata et al.,* 2009; *Boesch et al.,* 2011]. It is particularly important to identify and quantify the spatiotemporal patterns of variability of CO_2 to further study global CO_2 sources and sinks associated

with anthropogenic events. Continuous and globally distributed CO_2 data gives scientists the opportunity to explore CO_2 variability at different time scales, as well as identify how well the models simulate the CO_2 variability. Additionally, satellite measurements allow a better understanding of the altitudinal variation of CH_4. More knowledge of this vertical mode of variation of CH_4 can help us better understand its impacts on current and future climate change.

1.1 Motivation

This research yields a validation of new satellite data and allows a quantitative study of how to use satellite CO_2 and *in situ* measurements to better understand the annual cycle and interaction between the biosphere and the atmosphere. Understanding how the biosphere acts as a carbon sink could aid in future mitigation for climate change, as well as to help us understand seasonal variability of CO_2 accumulations. Quantifying the biosphere's sink capabilities has not been possible until now; however, satellite-retrieved Solar-induced Fluorescence (SIF) offers this new possibility. The answers discovered by this research yield a better understanding of global CO_2 satellite retrievals, as well as contributions of the ecosystem to the CO_2 budget and variability of CO_2 concentrations. Our results could help diagnose current inaccuracies in the models and thereby lead to their improvement. Additionally, understanding the carbon dioxide annual cycle allows for greater understanding of the carbon budget. These results can be used to better understand the vertical structures for the CO_2 annual cycle and semiannual cycle and help identify deficiencies in the models, which are crucial to understanding of the global carbon budget.

Additionally, this research can help us understand how concentrations of CH_4 originating in the central Pacific Ocean are transported to other locations. Understanding greenhouse gas transport will potentially aid in a new generation of anthropogenic interaction with the climate, and could possibly influence the development of legislation that limits greenhouse gas emissions and resultant impacts. Fully understanding the effects of emissions is the first step in mitigating actions and being able to reduce the tangible impacts and the negative effects caused by these emissions. Previously, it was not understood how El Niño-Southern Oscillation affected CH_4 in the central Pacific region, and so it was difficult to understand its effects on atmospheric chemistry and radiation; however, with this research, a greater understanding of the CH_4 transport is achieved.

1.2 Dissertation Overview

Greenhouse gases, such as carbon dioxide and methane, play a critical role in global warming and climate change. Retrieved concentrations from satellites measurements (e.g., OCO-2, GOSAT, AIRS, TES) offer a new opportunity to understand the variability of CO_2 and CH_4 over the global domain. First, innovative OCO-2 CO_2 data and GOSAT CO_2 data were validated with *in situ* Total Carbon Column Observing Network (TCCON) CO_2 data. Second, the annual variability of CO_2 was explored using satellite retrievals. A multiple regression method was used to estimate the CO_2 seasonal cycle from the satellite CO_2 retrievals and *in situ* CO_2 measurements, in order to better understand surface, mid-tropospheric, and column

CO_2 seasonal cycles. Third, pioneering satellite-retrieved Solar-induced Fluorescence (SIF) datasets were utilized to investigate the contributions of biosphere to CO_2. This analysis allows for a better understanding of how the biosphere acts as a source and as a sink for global CO_2; and furthermore, leads to a better understanding of the CO_2 global cycle. Finally, the potential of El Niño-Southern Oscillation to transport surface methane to the mid-troposphere was studied as a means of advecting methane to other regions. Rising air mass over the central Pacific during El Niño months brings low surface concentrations of CH_4 over the ocean to the middle troposphere, leading to lower mid-tropospheric CH_4 over the central Pacific than the western Pacific. Similarly, rising air can bring low surface concentrations of CH_4 to the middle troposphere over the western Pacific during La Niña months, contributing to lower mid-tropospheric CH_4 concentrations over the western Pacific than the central Pacific.

Chapter 2: The validation of OCO-2 CO_2 and GOSAT CO_2 with TCCON CO_2

2.1 Introduction

As previously mentioned, CO_2 is an important greenhouse gas that has enormous global warming potential. In order to understand the possible effects on anthropogenic emissions and activities, the data quality of CO_2 must first be understood. In this chapter, satellite-retrieved CO_2 concentration retrievals were validated by comparing them with ground-based measurements.

Satellites offer a revolutionary advance in scientific understanding by enabling a remotely acquired global understanding of atmospheric gases on an previously unachievable time scale [*Chahine et al*., 2008; *Kulawik et al*., 2010; *Yokata et al*., 2009; *Boesch et al*., 2011; *Reuter et al*., 2011; *Pagano et al*., 2014]. Previously, climate scientists and atmospheric chemists were limited to the sparse ground-based *in situ* measurements, and sporadic aircraft missions, to understand the transport and global concentrations of atmospheric gases. However, even satellites are further advancing in vertical sensitivity, allowing researchers to better understand air masses that are closer to the surface, and thus closer to the surface sources and sinks. Greenhouse Gases Observing Satellite (GOSAT) and Orbiting Carbon Observatory (OCO-2) provide a column estimate of atmospheric CO_2 with more emphasis on the lower troposphere. It has also been shown in previous studies that these space-based

CO_2 column observations can be utilized to estimate surface fluxes if they are acquired globally with precisions in the range of 1-10 ppm (0.3-3.0%) and without significant biases [*Baker et al.,* 2006; *Baker et al.,* 2010; *Feng et al.,* 2009; *Chevallier et al.,* 2007; *Houweling et al.,* 2005; *Rayner et al.,* 2001].

Atmospheric Infrared Sounder (AIRS) on the Aqua satellite retrieve mid-tropospheric CO_2 retrievals with precision of around 1-2 ppm in the tropics that have been validated by aircraft data [*Masueda et al*., 2002; *Chahine et al*., 2008]. However, AIRS lacks the sensitivity to retrieve near-surface CO_2 [*Chevallier et al.,* 2005].

The OCO-2 and GOSAT missions were developed specifically to deliver space-based X_{CO2} data with the precision, temporal and spatial resolution, and coverage needed to characterize the variability of CO_2 sources and sinks on regional spatial scales and seasonal to interannual timescales [*Public Release of Concentration Data,* 2010; *Miller et al.,* 2007]. To achieve these goals, the OCO-2 and GOSAT instrument design were optimized to measure the SWIR absorption bands of CO_2 at 1.61 and 2.06 μm, and the O_2 A-band at 0.765 μm, with high spectral resolution and high signal-to-noise [*Boesch et al.,* 2011].

2.2 Methodology and Data

In this section, GOSAT and OCO-2 column CO_2 retrievals were compared to *in situ* column CO_2 measurements to validate these new data sets. GOSAT, OCO-2

Satellite CO_2 data and TCCON column CO_2 data are described in the following sections.

2.2.1 GOSAT Column CO_2

Greenhouse Gases Observing Satellite (GOSAT) TANSO-FTS is a joint effort of the Ministry of the Environment, the National Institute of Environmental Studies, and the Japan Aerospace Exploration Agency. This satellite is the first to be completely dedicated to greenhouse gas monitoring. It collects high-resolution spectroscopic observations of reflected sunlight in the CO_2 bands near 1.6 and 2.06 μms and by the 0.765 μm O_2 A band. GOSAT uses optimal estimate approach developed by the Orbiting Carbon Observatory (OCO) [*Boesch et al*., 2006; *Connor et al*., 2008] to retrieve column CO_2.

GOSAT is sun synchronous with a local overpass time of about 13:00. Its circular, 0.0157-radian diameter, instantaneous field of view yields 10.5 km diameter footprints in nadir. Over land, and over the ocean at latitudes greater than 20^o from the subsolar latitude, its two-axis (along track and cross track) pointing mechanism soundings are separated by about 155 km (five-point mode) or about 273 km (three-point mode) [*Shiomi et al*., 2008; *Watanabe el al*., 2008; *Kuze et al*., 2009]. Over the ocean, and at latitudes less than 20^o from the subsolar latitude, the pointing mechanism targets a glint spot to provide adequate sensitivity for X_{CO2} estimates. In glint mode, it collects soundings at about 28 km intervals along the apparent path of the glint mode. It repeats its global coverage every 3 days. GOSAT version B3.4

X_{CO2} is available from June 2009 to December 2016 and can be downloaded from http://disc.sci.gsfc.nasa.gov/acdisc/data-holdings/acos-data-holdings. GOSAT column CO_2 retrieved by OCO-2 science team are validated in this chapter.

2.2.2 OCO-2 Column CO_2

Orbiting Carbon Observatory (OCO-2) was launched in July 2014, after OCO-1 failed to make orbit. OCO-2 joined the front of the Afternoon Constellation (A-Train) at an altitude of 705 km. It samples the data at a local time of 1:30 pm. The OCO-2 collects eight spatially resolved radiance spectra of reflected sunlight in three narrow wavelength bands three times per second [*Eldering et al*., 2017]. The total column of carbon dioxide is estimated from the spectra using a physics-based retrieval method [*Bosch et al*., 2006; *O'Dell et al*., 2002; *Conner et al*., 2008; *Boesch et al*., 2011]. OCO-2 provides CO_2 with precision, resolution, and coverage needed to characterize CO_2 sources and sinks on the regional scale [*Crisp et al*., 2004; *Miller et al*., 2007]. It employs high-resolution spectra of reflected sunlight taken simultaneously in the near-infrared (NIR). The band from 1.58 μms to 2.06 μms is used to get column averaged CO_2 dry air volume-mixing ratio X_{CO2} from space [*Kuang et al*., 2002; *Crisp et al*., 2004]. When looking straight down, OCO-2 has a 3 km^2 footprint; additionally, OCO-2 has a 16-day repeat cycle. The OCO-2 column CO_2 are available at http://disc.sci.gsfc.nasa.gov/uui/dataset?keywords=OCO%20ACOS. OCO-2 version 7 X_{CO2} is available from September 2014 to December 2016. OCO-2 column CO_2 are validated in this chapter.

2.2.3 TCCON Column CO_2 Measurements

To validate the satellite CO_2 data sets, precise *in situ* column CO_2 measurements from TCCON [*Washenfelder et al*., 2006; *Macatangay et al*., 2008; *Wunch et al*., 2011]. TCCON stations use a high spectral resolution Fourier-transform infrared spectroscopy (FTS) to record the absorption of direct sunlight by CO_2, O_2, and other gases. Under clear sky conditions, measurement precision for the TCCON column CO_2 is ~0.1% [*Washenfelder et al*., 2006]. There are twenty operational sites between Ny Alesund, Norway (79°N), and Lauder, New Zealand (45°S) (http://www.tccon.caltech.edu/). Table 2.1 summarizes time periods and spatial coverage for all datasets used in this chapter.

Type	Data	Time Period	Latitude Range
Satellite CO_2	OCO-2 X_{CO2} [Eldering *et al.*, 2017]	Jul 2014 – Dec 2016	60°S - 80°N
	GOSAT X_{CO2} [Crisp *et al.*, 2012]	Jun 2009 – Dec 2016	50°S - 82°N
Surface CO_2	TCCON CO_2 [Washenfelder *et al.*, 2006]	Different time periods for different stations	45°S - 79°N

Table 2.1: Summary of time periods and spatial coverage for different CO_2 datasets.

2.2.4 Methodology

OCO-2 and GOSAT column CO_2 retrievals were compared with TCCON column CO_2 when the satellite CO_2 data are within a circle with a radius of 100 km of the surface site. Differences were estimated between satellite CO_2 retrievals and *in situ* CO_2 measurements (TCCON CO_2). Standard deviations of CO_2 differences

(Satellite CO_2 – TCCON CO_2) were also estimated. A least squares fit method was used to calculate the fitted regression line between satellite CO_2 and TCCON CO_2. The R^2 coefficients of determination were also calculated to measure how close the real data were to the fitted regression line. By comparing the satellite CO_2 retrievals with surface measurements, a better understanding of the errors and uncertainties in GOSAT and OCO-2 column CO_2 data was achieved.

2.3 Results

GOSAT and OCO-2 column CO_2 retrievals were compared to TCCON column CO_2 at twelve stations. The twelve stations were chosen at locations where the TCCON data records were relatively long and overlapped with the satellite CO_2 data, resulting in twelve stations. The twelve stations are as follows: Bialystok, Bremen, Orleans, Garmisch, Parkfalls, Rikubetsu, Lamont, Armstrong, Ascension, Darwin, Reunion, and Lauder. CO_2 differences between OCO-2 CO_2 and TCCON CO_2, standard deviations of CO_2 differences, slopes and intercepts of fitted regression lines, and R^2 values are shown in Table 2.2. When all stations were averaged together, the difference between OCO-2 column CO_2 retrievals and TCCON column CO_2 data is 0.228 ppm with a standard deviation of 0.921 ppm.

Station	Latitude	Longitude	CO_2 Difference	CO_2 std	Slope	Intercept	R^2
Bialystok	53.231	23.021	0.223	0.808	0.898	40.833	0.957
Bremen	53.116	8.847	0.544	1.162	0.903	39.395	0.888
Orleans	47.990	2.109	0.537	1.269	1.185	-73.249	0.915
Garmisch	47.496	11.062	0.803	0.994	0.942	23.896	0.885
Parkfalls	45.940	-90.261	-0.524	0.976	0.956	17.423	0.950
Rikubetsu	43.461	143.757	-0.249	1.232	0.831	67.545	0.909
Lamont	36.600	-97.498	0.093	0.712	0.980	7.882	0.959
Armstrong	34.960	-117.876	0.265	0.841	1.030	-11.930	0.925
Ascension	-7.918	-14.333	0.408	0.691	0.807	77.498	0.912
Darwin	-12.430	130.881	0.143	0.732	0.805	77.952	0.920
Reunion	-20.900	55.489	0.274	0.748	0.874	50.467	0.872
Lauder	-45.040	169.674	-0.016	0.561	0.891	43.447	0.938
All Stations			0.228	0.921	0.934	26.807	0.917

Table 2.2 Comparison of OCO-2 column CO_2 retrievals and TCCON column CO_2 at twelve stations. Locations of twelve stations, CO_2 differences between GOSAT column CO_2 and TCCON column CO_2, standard deviations of CO_2 differences, Slopes and intercepts of fitted regression lines, and R^2 for the regression lines.

Station locations, CO_2 differences between GOSAT CO_2 and TCCON CO_2, standard deviations of CO_2 differences, slopes and intercepts of fitted regression lines, and R^2 values are shown in Table 2.3. When all stations were averaged together, the difference between GOSAT column CO_2 retrievals and TCCON column CO_2 data is -0.632 ppm with a standard deviation of 1.349 ppm.

Station	Latitude	Longitude	CO_2 Difference	CO_2 std	Slope	Intercept	R^2
Bialystok	53.231	23.021	-0.273	0.928	0.969	11.639	0.979
Bremen	53.116	8.847	0.289	1.293	1.028	-10.829	0.958
Orleans	47.990	2.109	-0.181	1.046	0.984	6.284	0.964
Garmisch	47.496	11.062	0.291	1.006	1.010	-3.710	0.969
Parkfalls	45.940	-90.261	-0.524	1.108	0.959	15.699	0.966
Rikubetsu	43.461	143.757	0.162	0.955	0.933	26.934	0.954
Lamont	36.600	-97.498	-1.718	0.999	0.995	0.347	0.969
Armstrong	34.960	-117.876	-0.366	1.107	0.978	8.251	0.904
Ascension	-7.918	-14.333	-1.613	0.853	1.033	-14.655	0.915
Darwin	-12.430	130.881	-1.254	0.780	0.945	20.223	0.976
Reunion	-20.900	55.489	-1.925	1.075	0.999	-1.378	0.930
Lauder	-45.040	169.674	-0.738	1.781	0.965	12.919	0.872
All Stations			-0.632	1.349	0.977	8.343	0.942

Table 2.3 Comparison of GOSAT column CO_2 retrievals and TCCON column CO_2 at twelve stations. Locations of twelve stations, CO_2 differences between GOSAT column CO_2 and TCCON column CO_2, standard deviations of CO_2 differences, Slopes and intercepts of fitted regression lines, and R^2 for the regression lines.

In Figure 2.1, time series of co-located OCO-2 column CO_2 (shown in blue dots) and TCCON column CO_2 (shown in red dots) for Bialystok (Panel a), Bremen (Panel c), Orleans, (Panel e) and Garmisch (Panel g) demonstrated good match between OCO-2 column CO_2 and TCCON column CO_2. Co-located OCO-2 column CO_2 was estimated within a circle with a radius of 100 km around the surface TCCON CO_2 station, so a fair comparison could be conducted between satellite OCO-2 CO_2 and TCCON column CO_2. The differences of OCO-2 column CO_2 and TCCON column CO_2 are about 0.223±0.808 ppm, 0.544±1.162 ppm, 0.537±1.269 ppm, and 0.803±0.994 ppm for Bialystok, Bremen, Orleans, and Garmisch,

respectively. Additionally, in all time series, both OCO-2 column CO_2 and TCCON column CO_2 data demonstrated the seasonal cycle of CO_2 as well as the increasing trend of CO_2.

Scatter plots for the co-located OCO-2 column CO_2 and TCCON column CO_2 are shown in Figure 2.1b, Figure 2.1d, Figure 2.1f, and Figure 2.1h. Linear fitting lines were estimated by the least-square fit from the co-located OCO-2 column CO_2 and TCCON column CO_2, which are shown as red lines in Figure 2.1b, Figure 2.1d, Figure 2.1f, and Figure 2.1h. The slopes for the linear-fitting lines (red lines) are 0.898, 0.903, 1.185, and 0.942 for Bialystok, Bremen, Orleans, and Garmisch, respectively. The slopes are a little lower than 1 at Bialystok, Bremen, and Garmisch and a little higher than 1 at Orleans. The R^2 coefficients of determination were also calculated and are close to 1, which suggested that the data are close to the fitted regression lines.

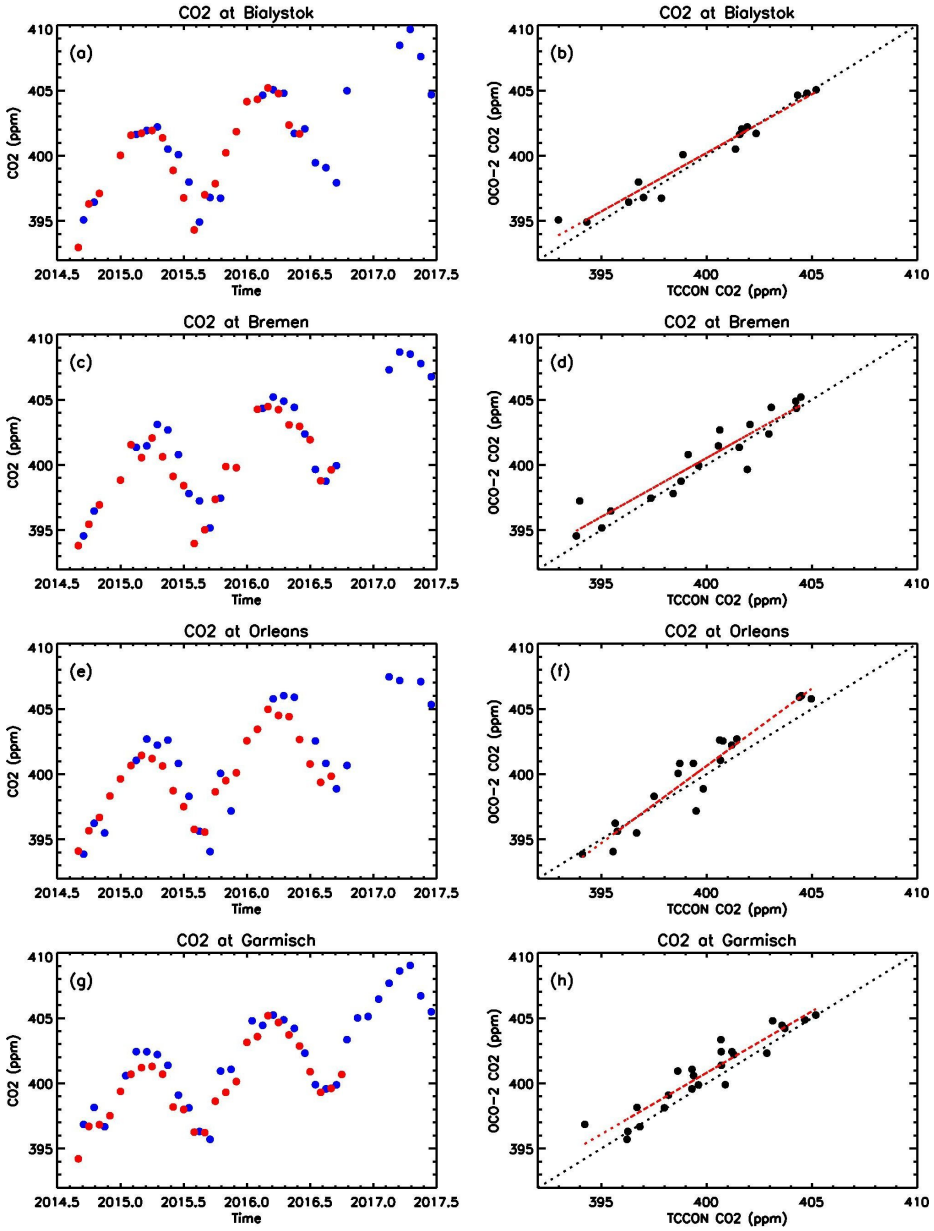

Figure 2.1: (a) Time series of OCO-2 CO_2 (blue dots) and TCCON CO_2 (red dots) at Bialystok (53.23°N, 23.02°E). (b) Scatter plot of OCO-2 CO_2 and TCCON CO_2 at Bialystok. Red line is the linear fitting line of the data. Black dotted line is a reference line with a slope of 1. (c) and (d) are for CO_2 data at Bremen (53.12°N, 8.85°E). (e) and (f) are for CO_2 data at Orleans (47.99°N, 2.11°E). (g) and (h) are for CO_2 data at Garmisch (47.50°N, 11.06°E). Units are ppm.

In Figure 2.2, time series of co-located OCO-2 CO_2 (shown in blue dots) and TCCON CO_2 (shown in red dots) for Parkfalls (Panel a), Rikubetsu (Panel c), Lamont (Panel e) and Armstrong (Panel g) demonstrate a good match between OCO-2 column CO_2 and TCCON column CO_2. The differences of OCO-2 column CO_2 and TCCON column CO_2 are about -0.524±0.976 ppm, -0.249±1.232 ppm, 0.093±0.712 ppm, and 0.265±0.841 ppm for Parkfalls, Rikubetsu, Lamont, and Armstrong, respectively. Scatter plots for the co-located OCO-2 column CO_2 and TCCON column CO_2 are shown in Figure 2.2b, Figure 2.2d, Figure 2.2f, and Figure 2.2h. The slopes for the linear-fitting lines (red lines) are 0.956, 0.831, 0.980, and 1.030 for Parkfalls, Rikubetsu, Lamont, and Armstrong, respectively. The slopes are a little lower than 1 at Parkfalls, Rikubetsu, Lamont and a little higher than 1 at Armstrong. The R^2 coefficients of determination for these scatter plots are close to 1, which suggests that the data are close to the fitted regression lines.

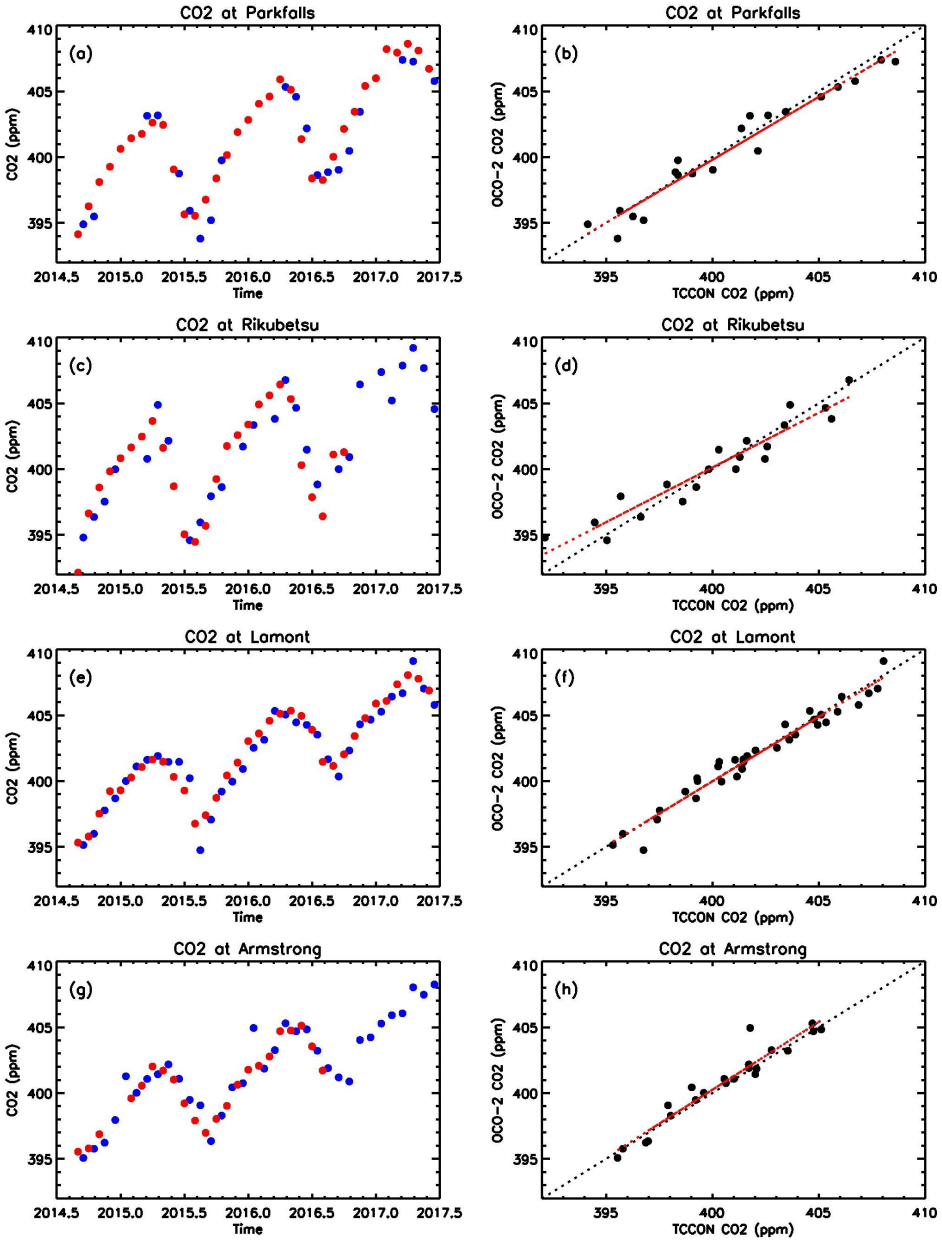

Figure 2.2: (a) Time series of OCO-2 CO_2 (blue dots) and TCCON CO_2 (red dots) at Parkfalls (45.94°N, 90.26°W). (b) Scatter plot of OCO-2 CO_2 and TCCON CO_2 at Parkfalls. Red line is the linear fitting line of the data. Black dotted line is a reference line with a slope of 1. (c) and (d) are for CO_2 data at Rikubetsu (43.46°N, 143.76°E). (e) and (f) are for CO_2 data at Lamont (36.6°N, 97.50°W). (g) and (h) are for CO_2 data at Armstrong (34.96°N, 117.88°W). Units are ppm.

In Figure 2.3, time series of co-located OCO-2 CO_2 (shown in blue dots) and TCCON CO_2 (shown in red dots) for Ascension (Panel a), Darwin (Panel c), Reunion (Panel e) and Lauder (Panel g) shows a good match between OCO-2 column CO_2 and TCCON column CO_2. The differences of OCO-2 column CO_2 and TCCON column CO_2 are about 0.408±0.691 ppm, 0.143±0.732 ppm, 0.274±0.748 ppm, and -0.016±0.561 ppm for Ascension, Darwin, Reunion, and Lauder, respectively. Scatter plots for the co-located OCO-2 column CO_2 and TCCON column CO_2 are shown in Figure 2.3b, Figure 2.3d, Figure 2.3f, and Figure 2.3h. The slopes for the linear-fitting lines (red lines) are 0.807, 0.805, 0.874, and 0.891 for Ascension, Darwin, Reunion, and Lauder, respectively. The R^2 coefficients of determination for these scatter plots are close to 1, which suggested that the data are close to the fitted regression lines. Both CO_2 seasonal cycle and trend are demonstrated in the time series of Figures 2.1-2.3. The CO_2 seasonal cycle amplitudes are larger in the Northern Hemisphere than those in the Southern Hemisphere. Further exploration of CO_2 seasonal cycle amplitudes over the global domain will be discussed in Chapter 3.

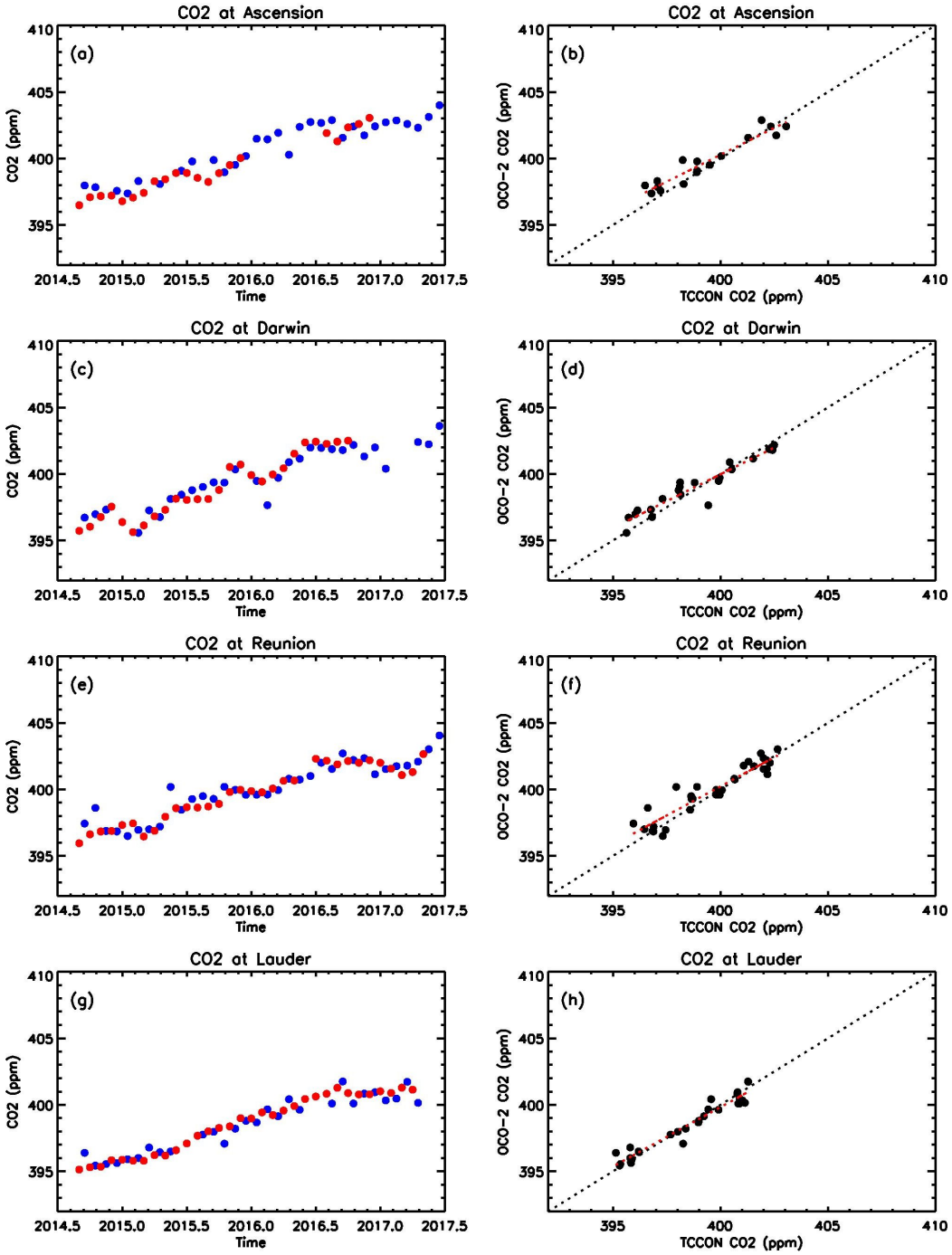

Figure 2.3: (a) Time series of OCO-2 CO_2 (blue dots) and TCCON CO_2 (red dots) at Ascension (7.92°S, 14.33°W). (b) Scatter plot of OCO-2 CO_2 and TCCON CO_2 at Ascension. Red line is the linear fitting line of the data. Black dotted line is a reference line with a slope of 1. (c) and (d) are for CO_2 data at Darwin (12.43°S, 130.88°E). (e) and (f) are for CO_2 data at Reunion (20.9°S, 55.49°E). (g) and (h) are for CO_2 data at Lauder (45.04°S, 169.67°E). Units are ppm.

OCO-2 CO_2 and TCCON CO_2, were compared at twelve stations. Results are shown in Figure 2.4. The red line is the linear fit line, and the black dotted line is a reference line with a slope of 1. The slope for the red line is 0.934, which is close to the reference line, which suggests that the OCO-2 CO_2 measurements match the in situ TCCON CO_2, reasonably well. Difference of CO_2 between OCO-2 CO_2 and TCCON CO_2 at all twelve stations is 0.228 ppm with a standard deviation of 0.921 ppm.

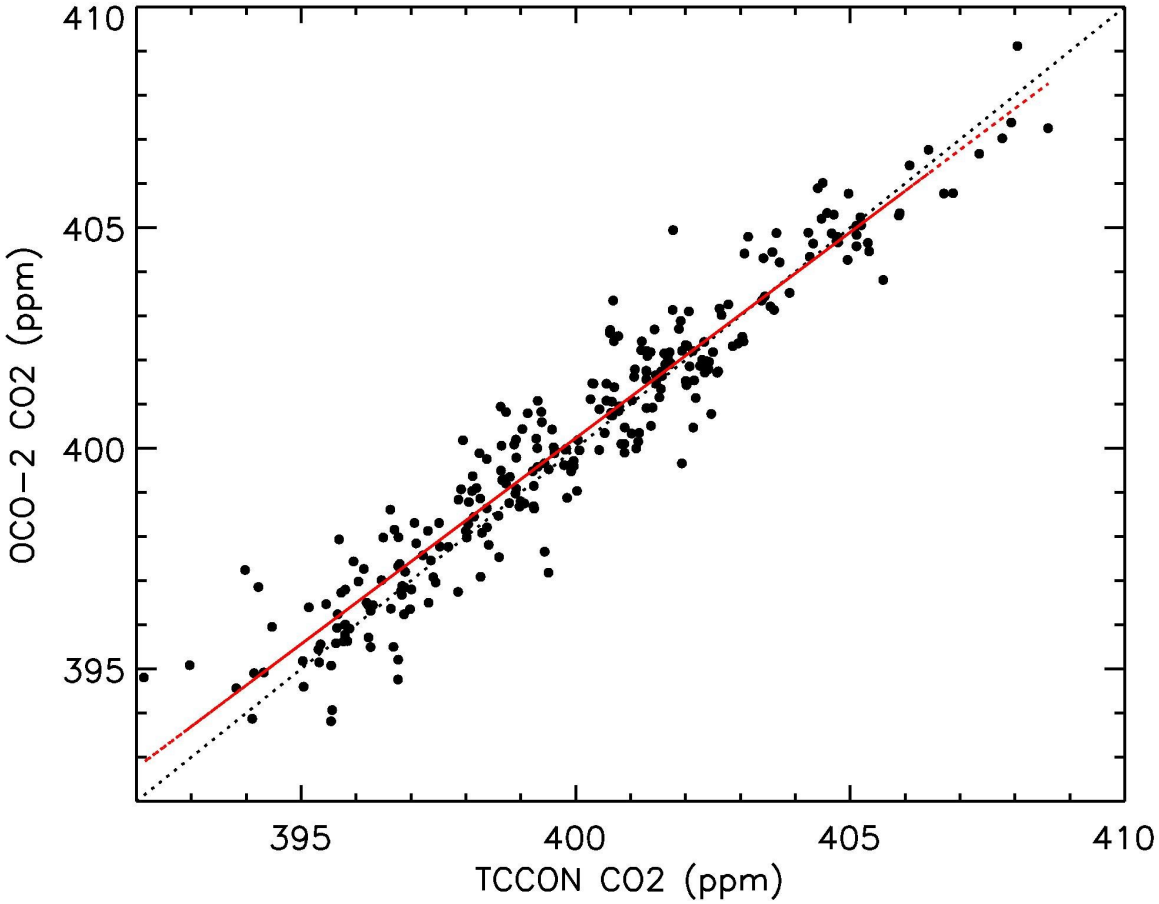

Figure 2.4: Scatter plot of OCO-2 CO_2 and TCCON CO_2. Red line is the linear fitting line of the data. Black dotted line is a reference line with a slope of 1. Units are ppm.

As shown in Figure 2.4, the CO_2 difference between OCO-2 CO_2 and TCCON CO_2 can be positive or negative. To explore if the CO_2 difference were random and follow the normal distribution, the probability density functions of CO_2 differences between OCO-2 CO_2 retrievals and TCCON CO_2 were estimated. The probability density function of CO_2 differences is plotted as the black solid line, and the Gaussian probability density function is plotted as the red dashed line in Figure 2.5. As shown in Figure 2.5, the differences of OCO-2 CO_2 retrievals and TCCON CO_2 follow a Gaussian distribution, which suggests that the errors in OCO-2 CO_2 are random errors. Random errors are errors moving in opposite directions and have a tendency to cancel each other. When the number of observations increases, the errors will decrease.

A comparison of co-located GOSAT column CO_2 to TCCON column CO_2 was also executed Time series of co-located GOSAT column CO_2 (blue dots) and TCCON column CO_2 (red dots) for Bialystok (Panel a), Bremen (Panel c), Orleans, (Panel e) and Garmisch (Panel g) are shown in Figure 2.6. As shown in Figure 2.6, GOSAT column CO_2 agree with TCCON column CO_2 reasonably well. The differences of GOSAT column CO_2 and TCCON column CO_2 are -0.273±0.928 ppm, 0.289±1.293 ppm, -0.181±1.046 ppm, and 0.291±1.006 ppm for Bialystok, Bremen, Orleans, and Garmisch, respectively.

Scatter plots for the co-located GOSAT column CO_2 and TCCON column CO_2 are shown in Figure 2.6b, Figure 2.6d, Figure 2.6f, and Figure 2.6h. The slopes for the linear-fitting lines (red lines) are 0.969, 1.028, 0.984, and 1.010 for Bialystok,

Bremen, Orleans, and Garmisch, respectively, which are close to 1. The R^2 coefficients of determination were also calculated and are close to 1, which suggest that the data are close to the fitted regression lines. Both GOSAT and OCO-2 CO_2 retrievals are close to TCCON CO_2 at these four stations.

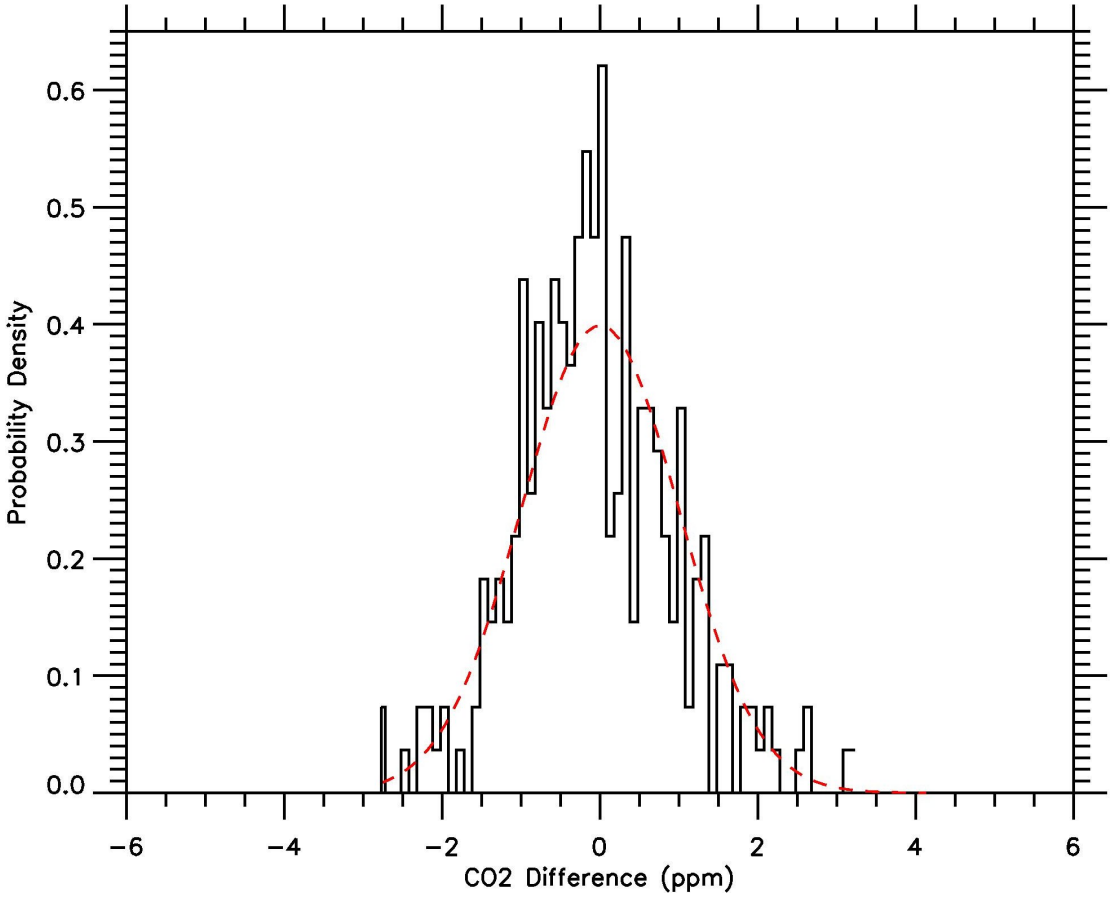

Figure 2.5: Probability density function of CO_2 difference between OCO-2 CO_2 retrievals and TCCON CO_2 (black solid line). Gaussian probability density is plotted as the red dashed line.

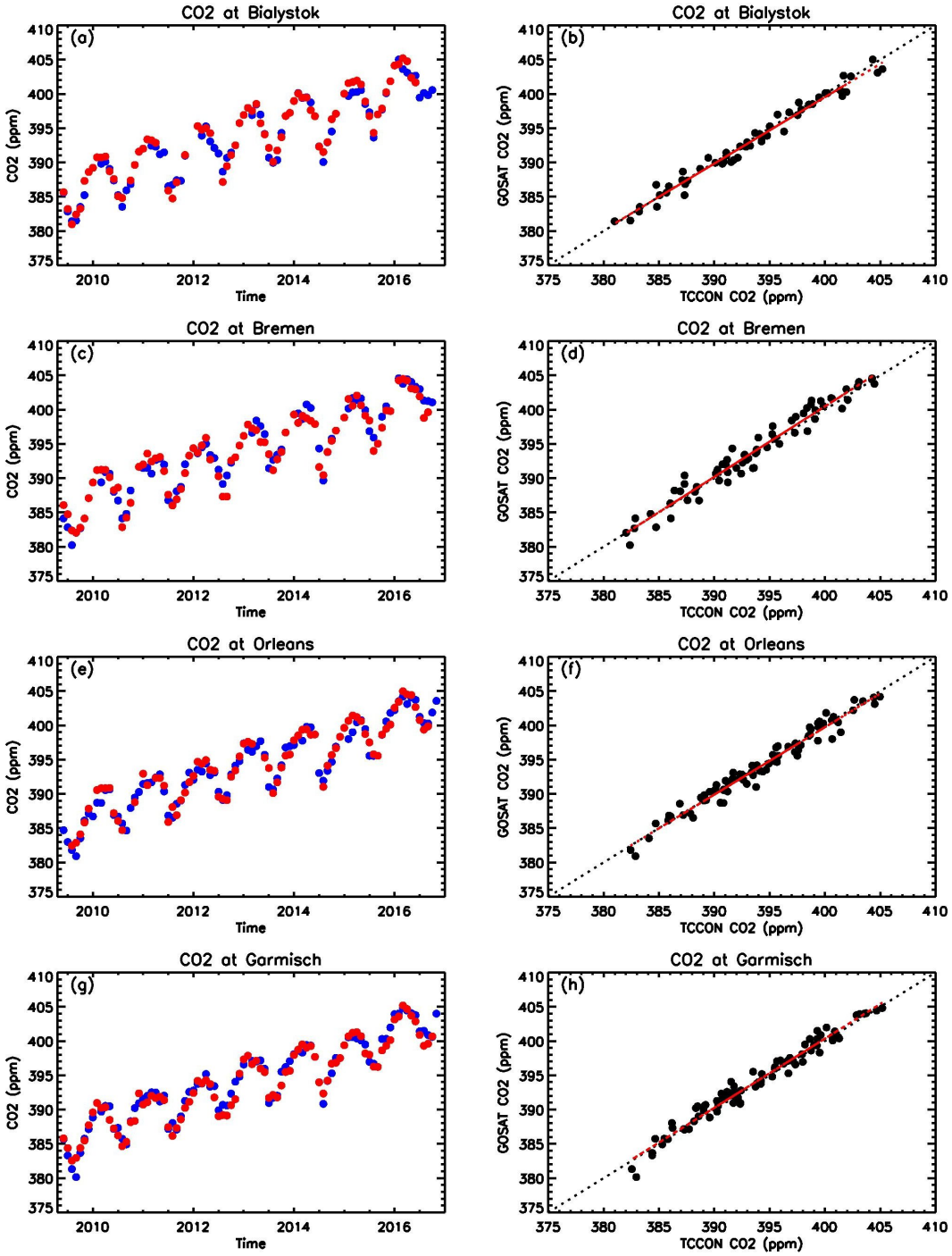

Figure 2.6: (a) Time series of GOSAT CO_2 (blue dots) and TCCON CO_2 (red dots) at Bialystok (53.23°N, 23.02°E). (b) Scatter plot of GOSAT CO_2 and TCCON CO_2 at Bialystok. Red line is the linear fitting line of the data. Black dotted line is a reference line with a slope of 1. (c) and (d) are for CO_2 data at Bremen (53.12°N, 8.85°E). (e) and (f) are for CO_2 data at Orleans (47.99°N, 2.11°E). (g) and (h) are for CO_2 data at Garmisch (47.50°N, 11.06°E). Units are ppm.

In Figure 2.7, time series of GOSAT column CO_2 (blue dots) and TCCON column CO_2 (red dots) for Parkfalls (Panel a), Rikubetsu (Panel c), Lamont (Panel e) and Armstrong (Panel g) show a good match between GOSAT CO_2 and TCCON CO_2. The differences of GOSAT column CO_2 and TCCON column CO_2 are about -0.524±1.108 ppm, 0.162±0.955 ppm, -1.718±0.999 ppm, and -0.366±1.107 ppm for Parkfalls, Rikubetsu, Lamont, and Armstrong, respectively. In the scatter plots in Figure 2.7, TCCON column CO_2 are compared with GOSAT CO_2 and the red lines are the linear fit lines. The black dotted lines are reference lines with a slope of 1. The slopes for the linear-fitting lines (red lines) are 0.959, 0.933, 0.995, and 0.978 for Parkfalls, Rikubetsu, Lamont, and Armstrong, which are close to 1. These results suggest GOSAT CO_2 data are close to TCCON CO_2 in these locations.

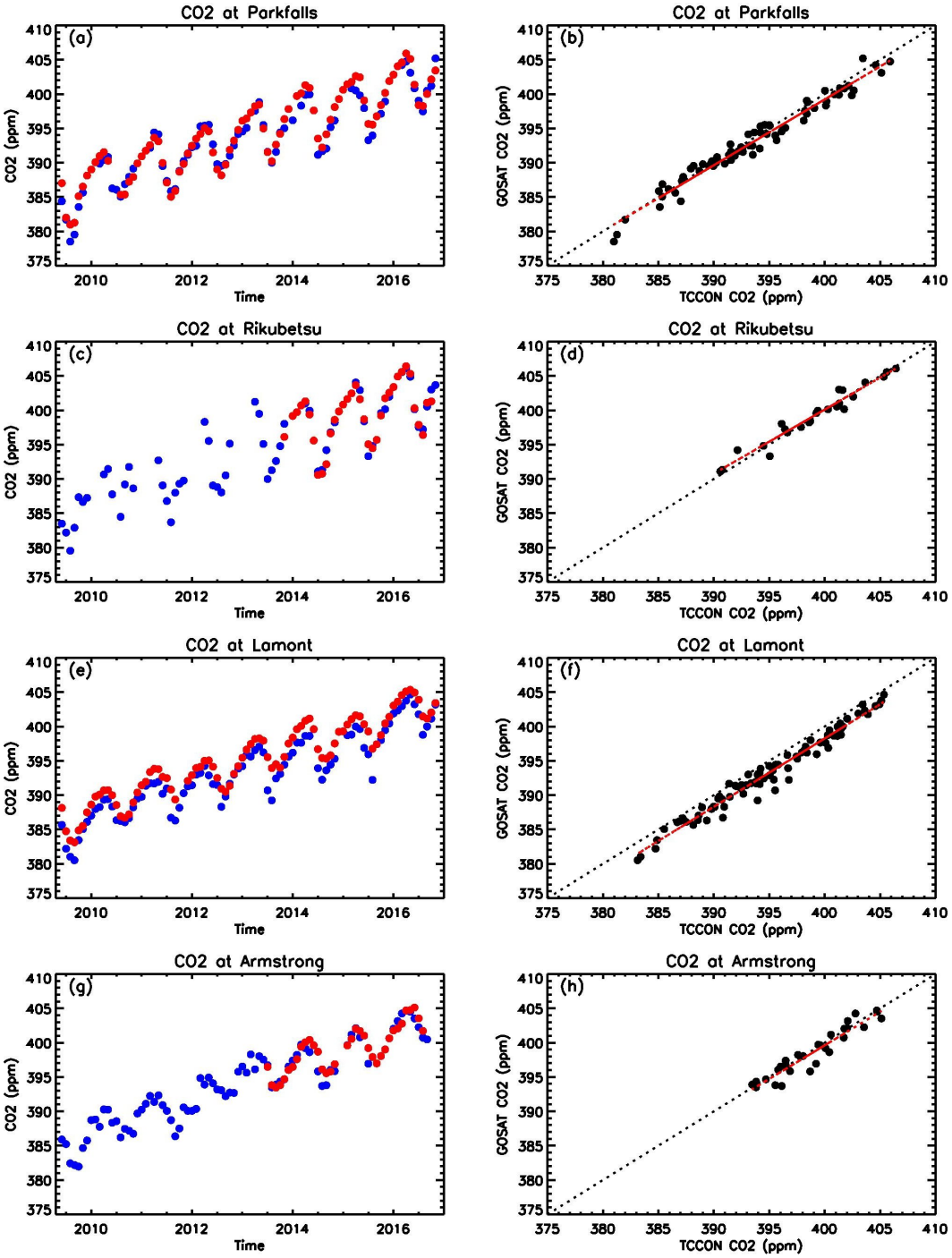

Figure 2.7: (a) Time series of GOSAT CO_2 (blue dots) and TCCON CO_2 (red dots) at Parkfalls (45.94°N, 90.26°W). (b) Scatter plot of GOSAT CO_2 and TCCON CO_2 at Parkfalls. Red line is the linear fitting line of the data. Black dotted line is a reference line with a slope of 1. (c) and (d) are for CO_2 data at Rikubetsu (43.46°N, 143.76°E). (e) and (f) are for CO_2 data at Lamont (36.6°N, 97.50°W). (g) and (h) are for CO_2 data at Armstrong (34.96°N, 117.88°W). Units are ppm.

In Figure 2.8, time series of GOSAT column CO_2 (blue dots) and TCCON column CO_2 (red dots) for Ascension (Panel a), Darwin (Panel c), Reunion (Panel e) and Lauder (Panel g) shows consistent trends between GOSAT and TCCON column CO_2. These four stations are in the Southern Hemisphere. GOSAT column CO_2 concentrations are lower than TCCON column CO_2 concentrations at these stations. The differences of GOSAT column CO_2 and TCCON column CO_2 are -1.613±0.853 ppm, -1.254±0.780 ppm, -1.925±1.075 ppm, and -0.738±1.781 ppm for Ascension, Darwin, Reunion, and Lauder, respectively. GOSAT column CO_2 also demonstrates larger variations than TCCON column CO_2 at Reunion and Lauder. Scatter plots for the co-located GOSAT column CO_2 and TCCON column CO_2 are shown in Figure 2.8b, Figure 2.8d, Figure 2.8f, and Figure 2.8h. The slopes for the linear-fitting lines (red lines) are 1.033, 0.945, 0.999, and 0.965 for Ascension, Darwin, Reunion, and Lauder, respectively. The R^2 coefficients of determination for these scatter plots are close to 1, which suggest that the data are close to the fitted regression lines. A comparison of GOSAT and OCO-2 column CO_2 to TCCON column CO_2 at these four stations suggest that the data quality of OCO-2 column CO_2 is better than the GOSAT column CO_2 in the Southern Hemisphere.

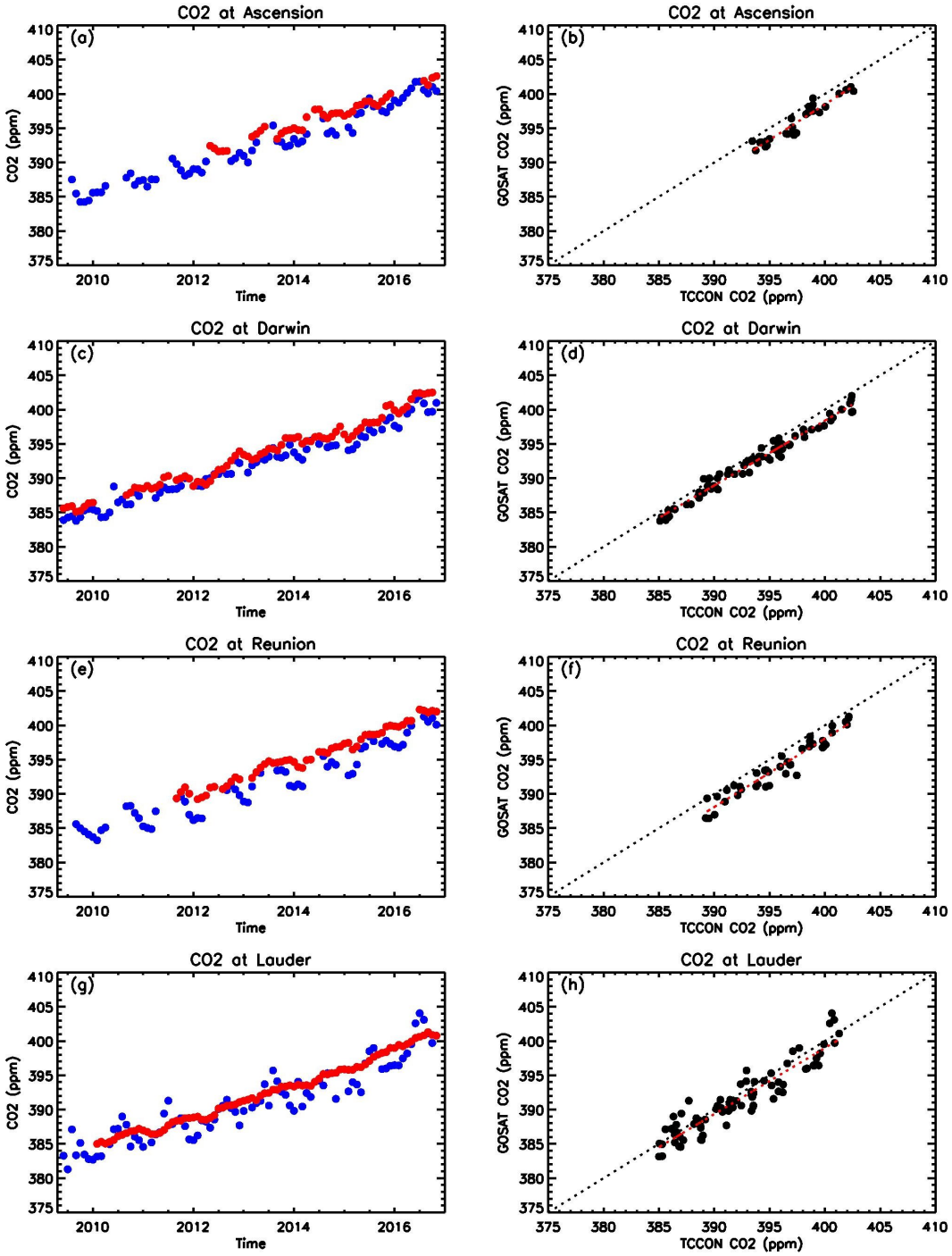

Figure 2.8: (a) Time series of GOSAT CO_2 (blue dots) and TCCON CO_2 (red dots) at Ascension (7.92°S, 14.33°W). (b) Scatter plot of GOSAT CO_2 and TCCON CO_2 at Ascension. Red line is the linear fitting line of the data. Black dotted line is a reference line with a slope of 1. (c) and (d) are for CO_2 data at Darwin (12.43°S, 130.88°E). (e) and (f) are for CO_2 data at Reunion (20.9°S, 55.49°E). (g) and (h) are for CO_2 data at Lauder (45.04°S, 169.67°E). Units are ppm.

Figure 2.9 shows a scatter plot of GOSAT column CO_2 and TCCON column CO_2 at twelve stations. The red line is a linear fit line, and the black dotted line is a reference line with a slope of 1. The slope for the red line is 0.977, which is close to 1. Difference of GOSAT column CO_2 and TCCON column CO_2 at all twelve stations is -0.632 ± 1.349 ppm, which is a little larger than the errors of the OCO-2 column CO_2 (0.228±0.921 ppm).

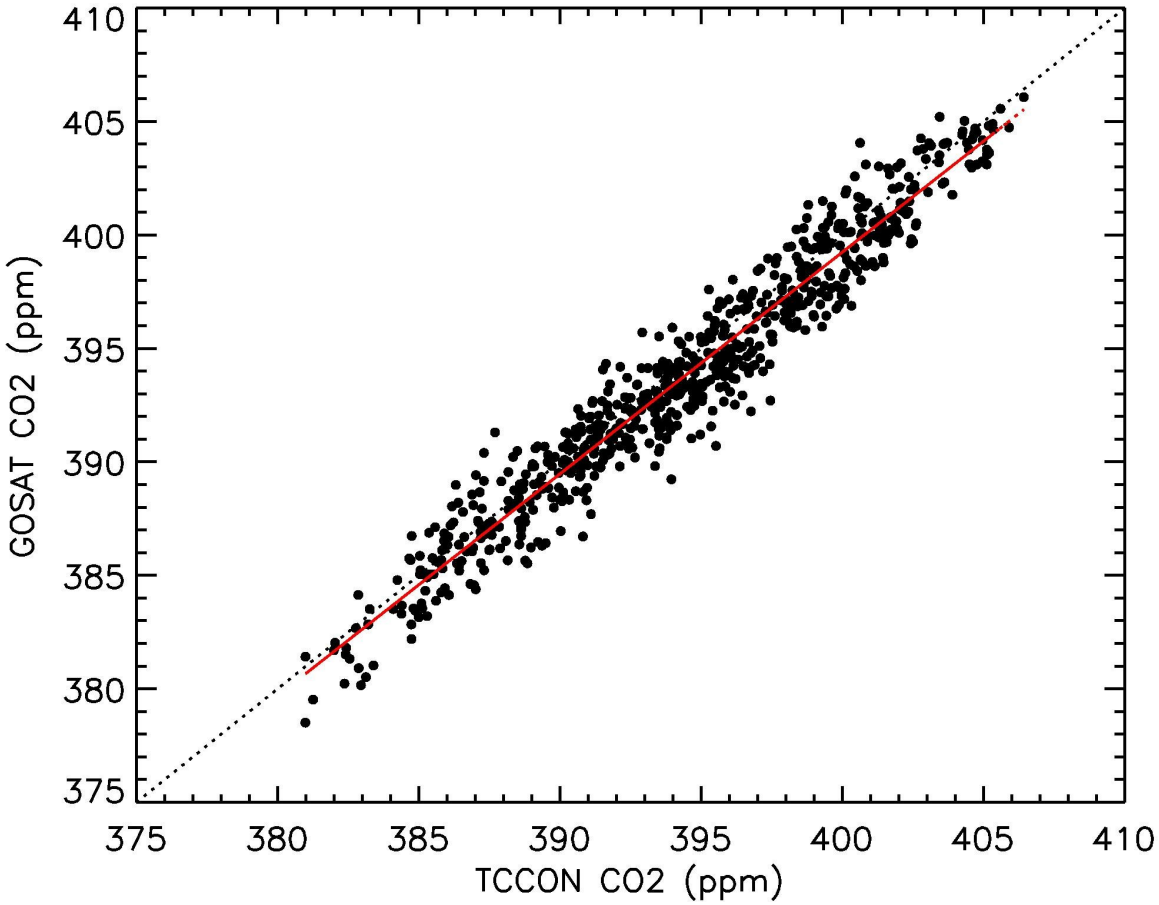

Figure 2.9: Scatter plot of GOSAT CO_2 and TCCON CO_2. Red line is the linear fitting line of the data. Black dotted line is a reference line with a slope of 1. Units are ppm.

The probability density function of CO_2 differences between GOSAT column CO_2 retrievals and TCCON column CO_2 is shown as the black solid line in Figure 2.10. The Gaussian probability density function is overlaid as the red dashed line in Figure 2.10. As shown in Figure 2.10, the differences of GOSAT column CO_2 retrievals and TCCON column CO_2 follow a Gaussian distribution. The errors in GOSAT column CO_2 are random errors, which will cancel each other when we average GOSAT column CO_2 retrievals.

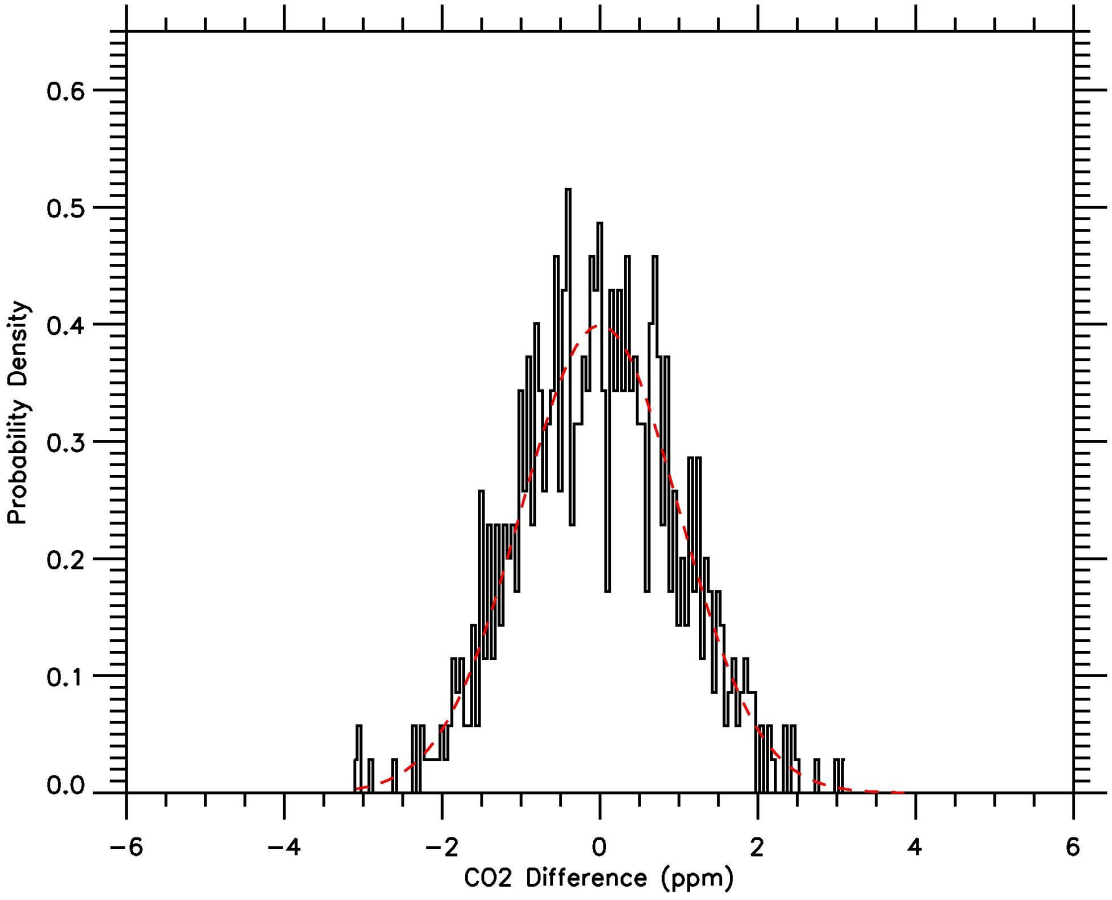

Figure 2.10: Probability density function of CO_2 difference between GOSAT retrievals and TCCON CO_2 (black solid line). Gaussian probability density is plotted as the red dashed line.

2.4 Conclusions

In this chapter, two satellite CO_2 data sets (OCO-2 CO_2 and GOSAT CO_2) were validated with *in situ* TCCON CO_2 measurements. Twelve TCCON CO_2 stations were chosen in this comparison, where the data records were long and overlapped with satellite CO_2 retrievals. These twelve stations covered from 45°S to 53.2°N. The difference of OCO-2 column CO_2 and TCCON column CO_2 at twelve stations is 0.228 ppm with a standard deviation of 0.921 ppm. The difference of GOSAT column CO_2 and TCCON column CO_2 at twelve stations is -0.632 ppm with a standard deviation of 1.349 ppm. Probability density functions were explored for the CO_2 differences between satellite CO_2 (e.g., OCO-2 and GOSAT) and TCCON CO_2. It was found that both OCO-2 and GOSAT CO_2 errors follow a Gaussian (normal) distribution, which suggested that the satellite CO_2 retrievals would decrease when we averaged data.

A detailed comparison between satellite column CO_2 with TCCON column CO_2 data further revealed that the two data sets were close at all stations. Both the satellite column CO_2 and TCCON column CO_2 captured CO_2 annual cycles and positive trends at these twelve stations. CO_2 annual cycle amplitudes are larger in the Northern Hemisphere than the Southern Hemisphere. The data quality of OCO-2 column CO_2 and GOSAT column CO_2 are equally as good in the Northern Hemisphere; while the data quality of OCO-2 column CO_2 is better than the GOSAT column CO_2 in the Southern Hemisphere. Results obtained in this Chapter are important for investigating CO_2 variability in future studies and research.

2.5 Acknowledgements

TCCON data is available at http://www.tccon.caltech.edu/. The OCO-2 column CO_2 are available at http://disc.sci.gsfc.nasa.gov/uui/dataset?keywords=OCO%20ACOS. GOSAT data is available at from http://disc.sci.gsfc.nasa.gov/acdisc/data-holdings/acos-data-holdings. This project is supported by NASA grants NNX13AC04G, NNX13AK34G, NNX16AG46G, and NNX15AI85G.

Chapter 3: Analysis of CO_2 annual cycle to explore the variability of CO_2 using GOSAT and OCO-2

3.1 Introduction

The terrestrial biosphere acts as a major sink for atmospheric CO_2 and sequesters on average 4 Pg C yr^{-1} [*Pan et al*., 2011]. This amount offsets about half of all anthropogenic emissions from fossil fuels and cement production [*Pan et al*., 2011]. Changes in climate affect photosynthesis and respiration, two factors that impact the net ecosystem exchange of CO_2 [*Richardson et al*., 2007].

As mentioned in the previous chapter, increases in fossil fuel emissions over the past several decades have caused atmospheric CO_2 to attain a positive trend that varies year to year with a range of 1.5 – 2 ppm from 1960 to 2014 [*Keeling et al*., 1995; *Sarmiento and Wolsy*, 1999; *Tans and Keeling*, 2014]. Overlaid on this trend is an annual cycle resulting from the uptake and release of the biosphere [*Pearman and Hyson*, 1980, 1981; *Cleveland et al*., 1983; *Bascastow et al*., 1985; *Keeling et al*., 1996; *Buermann et al*., 2007].

In the past, ground-based CO_2 measurement networks were utilized to monitor the CO_2 concentrations and their trends at the surface [GLOBALVIEW-CO2, 2010]. There are more than one hundred surface stations from National Oceanic and Atmospheric Administration - Earth System Research Laboratory (NOAA-ESRL), which monitor surface CO_2 concentrations. Yet, ground-based systems were lacking,

without the resolution or coverage needed to understand fluxes and transport in atmospheric column and around the globe. New remote sensing techniques allow scientists to study the variation of CO_2 over the global domain [e.g., *Chahine et al*., 2008; *Strow and Hannon*, 2008; *Crevoisier et al*., 2009; *Yokota et al*., 2009; *Kulawik et al*., 2010; *Rinsland et al*., 2010; *Foucher et al*., 2011; *Boesch et al*., 2011; *Crisp et al*., 2012; *Nguyen et al*., 2014; *Crisp et al*., 2016].

In addition to the increasing trend of CO_2 and the annual cycle from the biosphere interaction, atmospheric CO_2 also exhibits cycles from synoptic scales to interannual timescales [*Bacastow,* 1976*; Bacastow et al.,* 1980*; Keeling and Revelle*, 1985*; Keeling et al.,* 1995*; Enting*, 1987*; Feely et al.,* 1987*; Dettinger and Ghil,* 1998*; Dargaville et al.,* 2000*; Jiang et al.,* 2010*; Keppel-Aleks et al.,* 2011*; Wang et al.,* 2011*; Jiang et al.,* 2013a]. By combining remotely sensed data from satellites with ground-based *in situ* measurements and numerical models, it was found that the Madden-Julian Oscillation (MJO), Semiannual Oscillation (SAO), El Niño-Southern Oscillation (ENSO), monsoon, Northern Annular Mode (NAM), and South Atlantic Walker Circulation can influence CO_2 concentrations in the middle troposphere [*Li et al*., 2010; *Jiang et al*., 2010; *Wang et al*., 2011; *Jiang et al*., 2012, 2013a, 2015]. Keenan et al. [2014] presented that, although terrestrial models are capable of reproducing the magnitude of interannual variability, they are not consistent with the timing of observations of this variability in surface-atmosphere exchanges of CO_2 in mid-latitude forests in North America. It has been determined that terrestrial biosphere models are usually unable to properly explain the interannual variability in

deciduous canopy phenology [*Richardson et al.,* 2012] and that variability of spring Gross Primary Product (GPP) often drives variability in net ecosystem exchange on an interannual basis. [*Krishnan et al.,* 2008, 2009].

Satellite missions provide global measurements of the atmospheric CO_2 [*Chahine et al*., 2008; *Kulawik et al*., 2010; *Yokata et al*., 2009; *Boesch et al*., 2011; *Reuter et al*., 2011; *Pagano et al*., 2014]. This new global and continuous data allows a new opportunity to explore the CO_2 variability at different altitudes. In this chapter, we study the annual cycle of CO_2 using the Greenhouse Gases Observing SATellite (GOSAT), Orbiting Carbon Observatory-2 (OCO-2), Tropospheric Emission Spectrometer (TES), and Atmospheric Infrared Sounder (AIRS) to establish a better understanding of the CO_2 annual cycles at different altitudes globally. These results lead to a better understanding of the vertical structures for the CO_2 annual cycle, which is necessary to understanding the carbon budget.

3.2 Data

In this section, satellite-retrieved CO_2 concentrations and surface measurements were utilized to analyze its annual cycle to explore the variability of CO_2 in the atmosphere.

3.2.1 GOSAT

GOSAT column CO_2 retrieved by the OCO-2 science team were used in this chapter. GOSAT uses optimal estimate approach developed by the Orbiting Carbon Observatory, or OCO [*Boesch et al*., 2006; *Connor et al*., 2008] to retrieve column CO_2. GOSAT TANSO-FTS collects high-resolution spectroscopic observations of reflected sunlight in the CO_2 bands near 1.6 and 2.06 μm and by the 0.765 μm O_2 A band.

It was found that the GOSAT version B3.4 column CO_2 has negligible bias in column CO_2 retrievals [*Wunch et al*., 2011; *Crisp et al*., 2012]. GOSAT data is further mentioned in Section 2.2.1.

GOSAT B3.4 X_{CO2} data used here have passed a preliminary quality filter and are recommended for use in scientific analysis. In Chapter 2, we found that the error of GOSAT X_{CO2} is about -0.632±1.349 ppm when we compared GOSAT column CO_2 to TCCON column CO_2. In our study, we changed the grid of GOSAT CO_2 to 2^o latitude by 2^o longitude.

3.2.2 OCO-2

OCO-2 column CO_2 data was also used in Chapter 3. OCO-2 data is described in length in Section 2.2.2 and is summarized in Table 3.1.

3.2.3 AIRS Mid-tropospheric CO_2

AIRS is a cross-track scanning grating spectrometer aboard the Aqua satellite with 2378 channels from 3.7 to 15.4 μm with a 45 km × 45 km field of view at nadir [*Aumann et al*., 2003]. The mixing ratios of AIRS mid-tropospheric CO_2 are retrieved using the Vanishing Partial Derivative (VPD) method [*Chahine et al*., 2005, 2008; *Olsen and Licata*, 2015]. AIRS mid-tropospheric CO_2 retrievals are available over land and ocean under clear and cloudy conditions at 2° (latitude) × 2.5° (longitude) from September 2002 to December 2016. The maximum sensitivity of AIRS mid-tropospheric CO_2 retrieval is from 500 hPa to 300 hPa [*Chahine et al*., 2008]. The mid-tropospheric CO_2 retrieved via the VPD method captures the correct CO_2 annual cycle and trend and agrees well with the aircraft CO_2 from CONTRAIL [*Chahine et al*., 2005], INTEX-NA, and SPURT with a precision ~ 1–2 ppm [*Olsen et al*., 2008].

3.2.4 TES Mid-tropospheric CO_2

Tropospheric Emission Spectrometer (TES) is an imaging infrared FTS aboard on the Aura satellite, which was launched in July 2004. The TES spectral region extends from 660 cm^{-1} to 2260 cm^{-1} with a spectral resolution of 0.06 cm^{-1} [*Beer*, 2006; *Bowman et al*., 2006]. Mid-tropospheric CO_2 data from this instrument are available from 40°S to 45°N and from September 2004 to June 2011. Peak sensitivity of TES mid-tropospheric CO_2 data is at 511 hPa. The estimated error for TES mid-tropospheric CO_2 is ~10 ppm for a single target and ~1.3 ppm for the monthly mean on spatial scales of 20° (latitude) × 30° (longitude) [*Kulawik et al*.,

2010]. Comparison between TES CO_2 with ocean surface stations from GLOBALVIEW-CO2 reveals a correlation of 0.6. TES mid-tropospheric CO_2 measurements capture the correct CO_2 latitudinal gradient [*Kulawik et al*., 2010]. Kulawik et al. [2010] compared TES mid-tropospheric CO_2 to CONTRAIL aircraft CO_2, AIRS mid-tropospheric CO_2, and CarbonTracker model CO_2 and found similar annual cycles between TES mid-tropospheric CO_2 and others. TES mid-tropospheric CO_2 also correlates well with the Carbon Tracker model CO_2 at the surface and 5 km [*Kulawik et al*., 2010].

3.2.5 Surface Measurements

In addition to the satellite CO_2 data sets, precise *in situ* CO_2 measurements from surface flask measurements from the NOAA Earth System Research Laboratory (ESRL) network [*Tans et al*., 1998] and TCCON [*Washenfelder et al*., 2006; *Macatangay et al*., 2008; *Wunch et al*., 2011] were utilized in this study. Site information for the NOAA ESRL surface CO_2 is available at http://www.esrl.noaa.gov/gmd/dv/site/site_table.html.

TCCON stations use a high spectral resolution FTS to record the absorption of direct sunlight by CO_2, O_2, and other gases. Under clear sky conditions, measurement precision for the TCCON column CO_2 is ~0.1% [*Washenfelder et al*., 2006]. There are 20 operational sites between Ny Alesund, Norway (79°N), and Lauder, New

Zealand (45°S) (http://www.tccon.caltech.edu/). Table 3.1 summarizes time periods and spatial coverage for all datasets.

Type	Data	Time Period	Latitude Range
Satellite CO_2	OCO-2 X_{CO2} [Eldering *et al.*, 2017]	Jul 2014 – Dec 2016	60°S - 80°N
	GOSAT X_{CO2} [Crisp *et al.*, 2012]	Jun 2009 – Dec 2016	50°S - 82°N
	TES Mid-tropospheric CO_2 [Kulawik *et al.*, 2010]	Sep 2004 – Jun 2011	40°S - 45°N
	AIRS Mid-tropospheric CO_2 [Chahine *et al.*, 2008]	Sep 2002 – Dec 2016	60°S - 90°N
Surface CO_2	NOAA ESRL CO_2 [GLOBALVIEW-CO_2, 2010]	Different time periods for different stations	90°S - 85°N
	TCCON CO_2 [Washenfelder *et al.*, 2006]	Different time periods for different stations	45°S - 79°N

Table 3.1: Summary of time periods and spatial coverage for different CO_2 datasets.

3.3 Methodology

The decomposition of atmospheric time series into different components is critical for identifying and pinpointing variations of interest from the dataset. Analysis of the individual components has been widely used to obtain information about sources, sinks, and trends in greenhouse gases. Atmospheric data reflects a combination of long-term trends, short-term trends, and different oscillations from the observations. Due to the complicated periodic and random nature of trends, both long-and short-term, analyzing large atmospheric datasets is a very complex process [*Fernández-Duque et al.*, 2017].

Long-term, increasing trends in our study of CO_2 are mainly due to emisisons from fossil fuel burning and land use changes, overlapping with a large interannual variability related to climate-driven changes in sources and sinks [*Pickers et al*., 2015; *Artuso et al*., 2009]. Studying the data trend requires subtracting the seasonal component from the time series with a deseasonalization process through fitting appropriate mathematical functions to the data [*Pickers et al*., 2015].

Scientists have previously applied harmonic functions to describe the behavior of pollutants in the troposphere [*Artuso et al*., 2009; *Anderson-Cook et al*., 2000; *Sánchez et al.,* 2010; *Fernández-Duque et al*., 2017]. Regression techniques can offer considerable insights into air pollution analysis. Cleveland et al. [1979] suggested local regression methods could be used to obtain visual information from scatterplots [*Pérez et al*., 2017].

3.3.1 Multiple Regression Method

Column CO_2 retrievals from GOSAT and OCO-2 were combined with other satellite CO_2 data (e.g., AIRS and TES) and *in situ* measurements (e.g., surface CO_2 from NOAA- ESRL and TCCON column CO_2) to explore the annual cycle of CO_2. We used a multiple regression method to separate the CO_2 annual cycle from other variability.

To reveal CO_2 annual cycle amplitudes as a function of latitude, a multiple regression method was applied to all the data sets. CO_2 data were decomposed to the

trend, annual cycle, and semiannual cycle by the multiple regression method. CO_2 concentration at each location, X, was decomposed using the following empirical model [*Jiang et al*., 2013a]:

$$X(t) = A_0 + A_1 N P_1\left(\frac{t}{N}-1\right) + A_2 N^2 P_2\left(\frac{t}{n}-1\right) + A_3 N^3 P_3\left(\frac{t}{N}-1\right) + C_1\cos(2\pi t) + S_1\sin(2\pi t) + C_2\cos(4\pi t) + S_2\sin(4\pi t)$$

where t is time, N is the half length of the time period, the values P_1, P_2, and P_3 are the first, second, and third Legendre polynomials. The coefficients A_0, A_1, A_2, and A_3 are the mean value, the trend, the acceleration in the trend, and the coefficient for P_3, respectively. We added the third Legendre function to better fit the data sets. Annual and semiannual cycles are represented by harmonic functions. $C_1$and S_1 are the amplitudes of the annual cycle, while C_2 and S_2 are the amplitudes of the semiannual cycle. Satellite CO_2 seasonal cycle amplitude were be plotted against *in situ* measurements as a function of latitude. The amplitudes for the CO_2 annual cycle were then estimated by $\sqrt{C_1^2 + S_1^2}$. The amplitude for the CO_2 semiannual cycle is $\sqrt{C_2^2 + S_2^2}$.

3.4 Results

To explore the annual cycle of column CO_2 from GOSAT, a multiple regression method was applied to this data at different locations. An example of the multiple regression result for GOSAT column CO_2 at 38°N, 91°W is shown in Figure 3.1. GOSAT column CO_2 at 38°N, 91°W are shown as red dots in Figure 3.1a. The positive linear trend is shown as dotted line in Figure 3.1a. The multiple regression

result, defined as the sum of Legendre functions, semiannual cycle, and annual cycle, is shown as dashed line in Figure 3.1a. As shown in Figure 3.1a, the multiple regression result (dashed line) fits the raw data (red dots) very well. CO_2 annual cycle amplitude and CO_2 semiannual cycle amplitude obtained by the multiple regression method are shown in Figures 3.1b and 3.1c. Figure 3.1b shows that the 3 ppm CO_2 annual cycle is ~ ±3 ppm, with +3 ppm CO_2 occurring during the winter months, and -3 ppm occurring during the summer months, reflecting the CO_2 biosphere interaction when the active biosphere during growing seasons acts as a CO_2 sink.

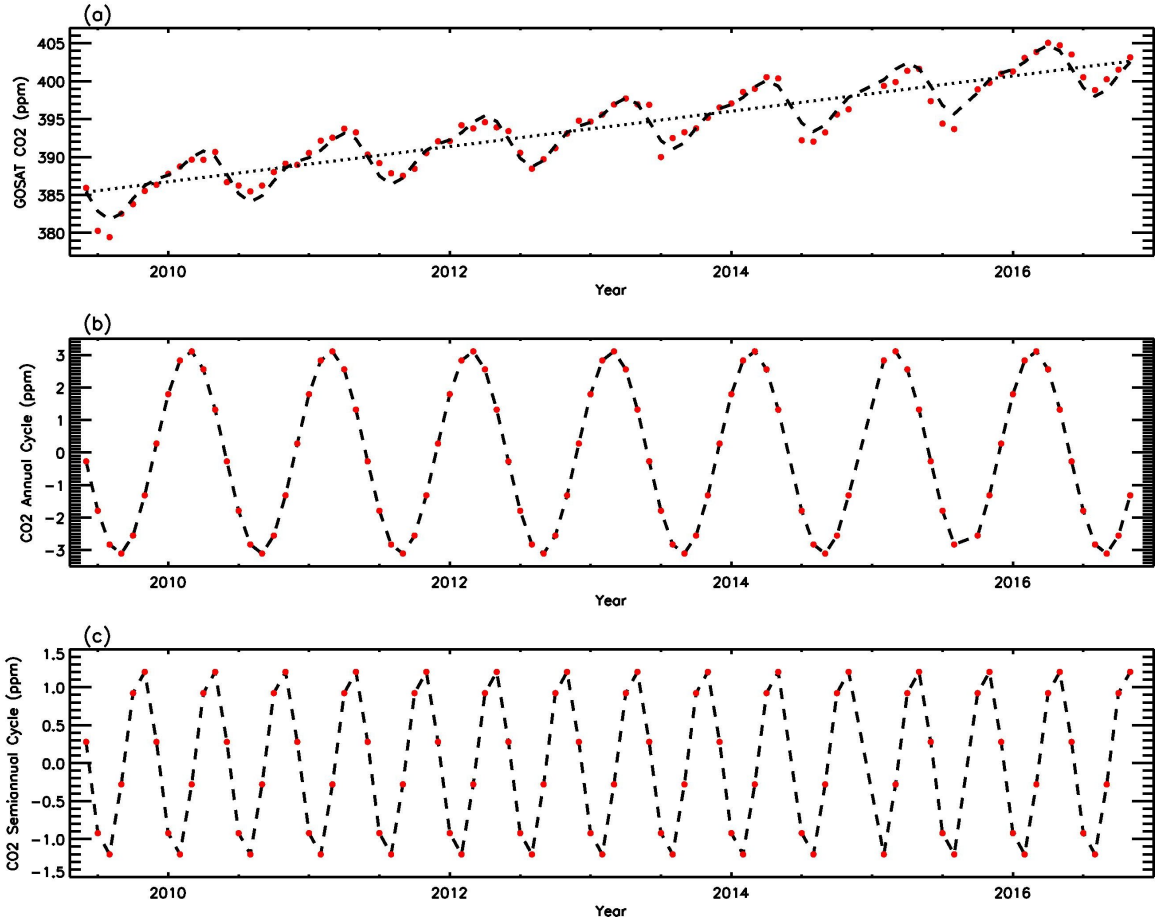

Figure 3.1: (a) GOSAT CO_2 at 91°W and 38°N (Red dots), linear trend (Dotted line), and multiple regression fit (Dashed line). (b) CO_2 annual cycle calculated from the multiple regression. (c) CO_2 semiannual cycle calculated from the multiple regression. Units are ppm.

For the next step, the CO_2 trend was calculated using a multiple regression method from 50°N to 50°S where GOSAT satellite data was available. As shown in Figure 3.2, there is between 1.8 to 2.5 ppm/year increase of CO_2 in the study region. CO_2 trend is smaller over the ocean than the land, because there is no anthropogenic source for CO_2 over the ocean. Over the equatorial region, the lower end of the linear trend range can be seen. This is probably because there is more complete ocean

coverage in the equatorial region and there is less CO_2 from the anthropogenic sources in these areas.

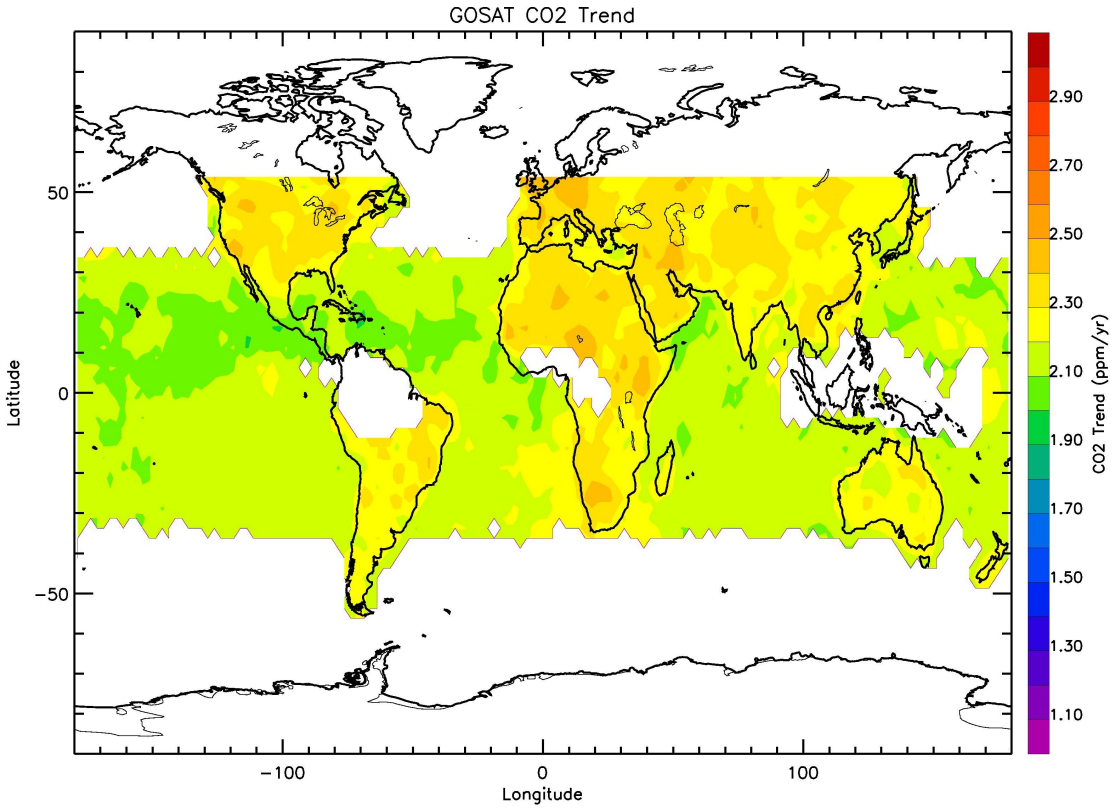

Figure 3.2: GOSAT CO_2 trend calculated from the multiple regression. Units are ppm/yr.

Annual cycle amplitudes for GOSAT column CO_2 were estimated by the multiple regression method over different locations. Results are shown in Figure 3.3. As shown in Figure 3.3, the annual cycle amplitudes of CO_2 are between 0.40 ppm and 4.40 ppm The lowest annual cycle is shown in the Southern Hemisphere over the landmasses from 0^o and 50^oS. The highest CO_2 annual cycle can be seen in the Northern Hemisphere landmasses with values around 4 ppm, as shown in Figure 3.3. The CO_2 annual cycle amplitudes are larger in the Northern Hemisphere than that in the Southern Hemisphere, because the amplitudes of the CO_2 annual cycles from the

biosphere's photosynthesis and respiration are larger in the Northern Hemisphere than that in the Southern Hemisphere [*Cleveland et al.*, 1983].

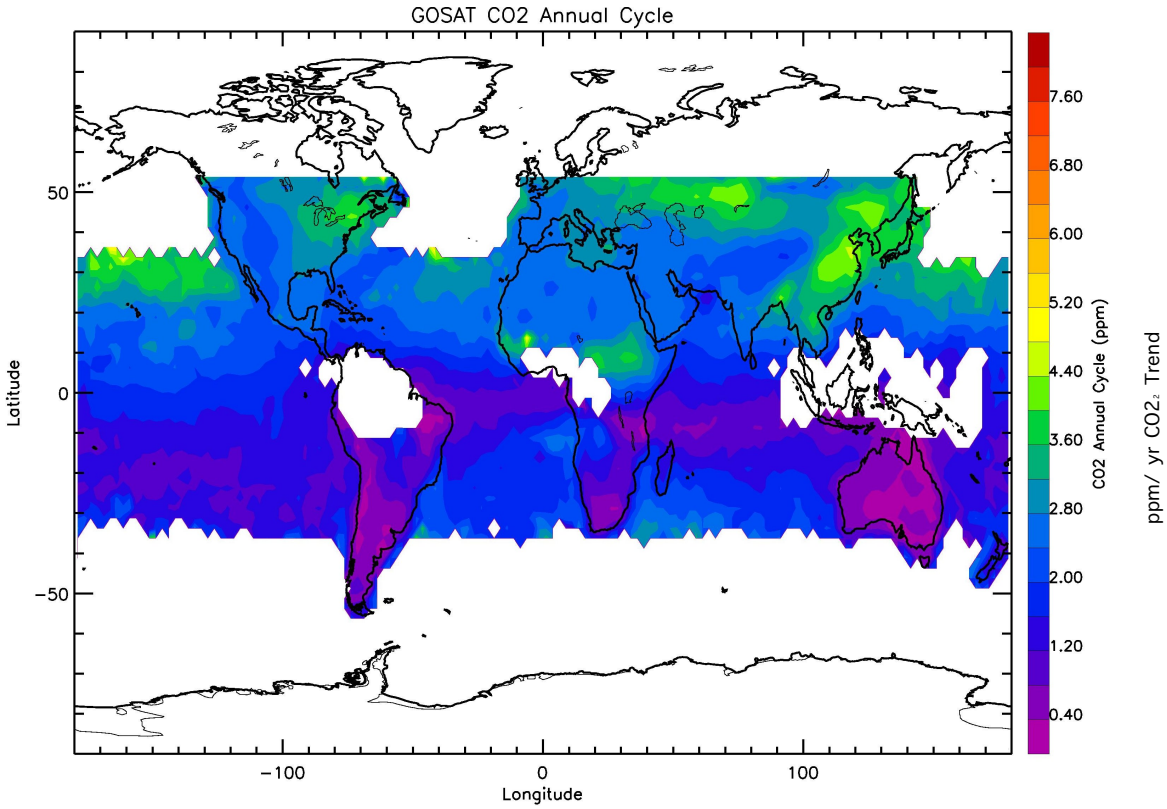

Figure 3.3: GOSAT CO_2 annual cycle amplitudes calculated from the multiple regression. Units are ppm.

Additionally, the CO_2 annual cycle was considered using OCO-2 retrieved X_{CO2} data using the multiple regression method. As shown in Figure 3.4, CO_2 annual cycle amplitudes are from 0.40 to 4.40 ppm. The lowest annual cycle can be seen at the Southern Hemisphere over the ocean, where there is smaller contribution from biospheric photosynthesis and respiration.

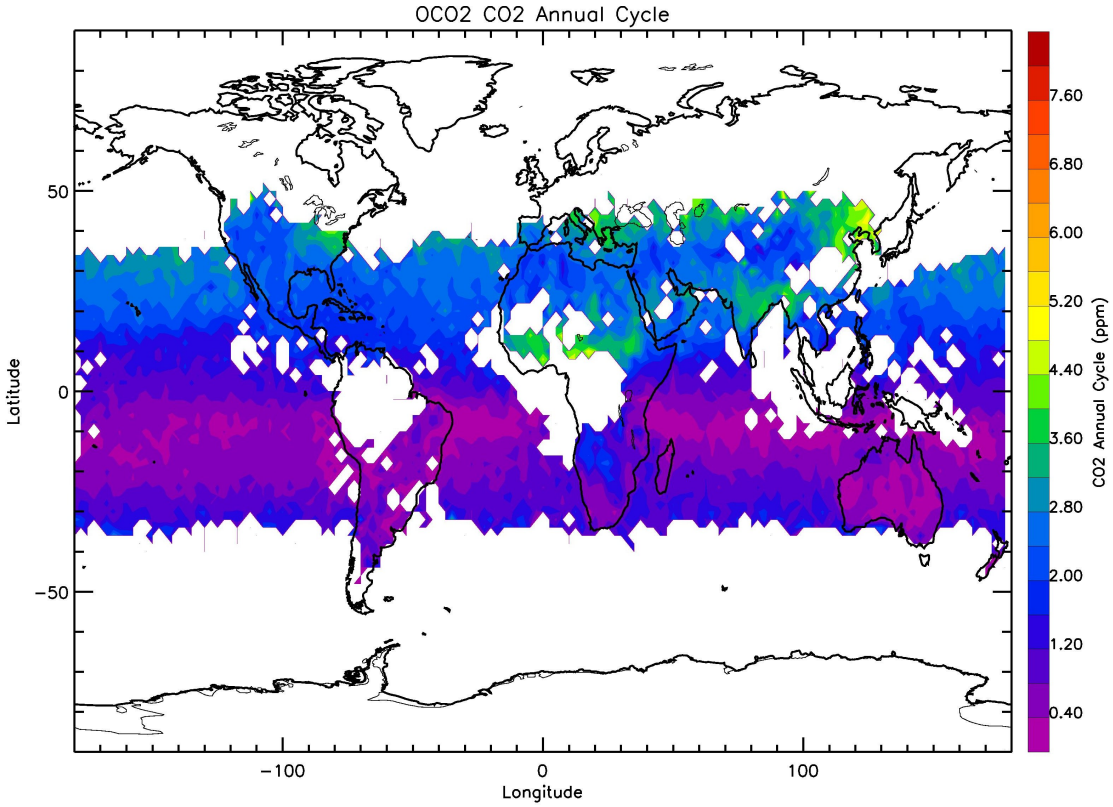

Figure 3.4: OCO-2 CO_2 annual cycle amplitudes calculated from the multiple regression. Units are ppm.

OCO-2 CO_2 and GOSAT CO_2 annual cycles were compared on latitudinal bands, as shown in Figure 3.5. The highest agreement between the OCO-2 and GOSAT satellite CO_2 annual cycle is in the latitudinal bands from both 0^o to 25^oN and 0^o to 25°S. The linear fit is not exactly 1:1 with a slope of 0.94, meaning GOSAT estimates the CO_2 annual cycle greater than the OCO-2 annual cycle.

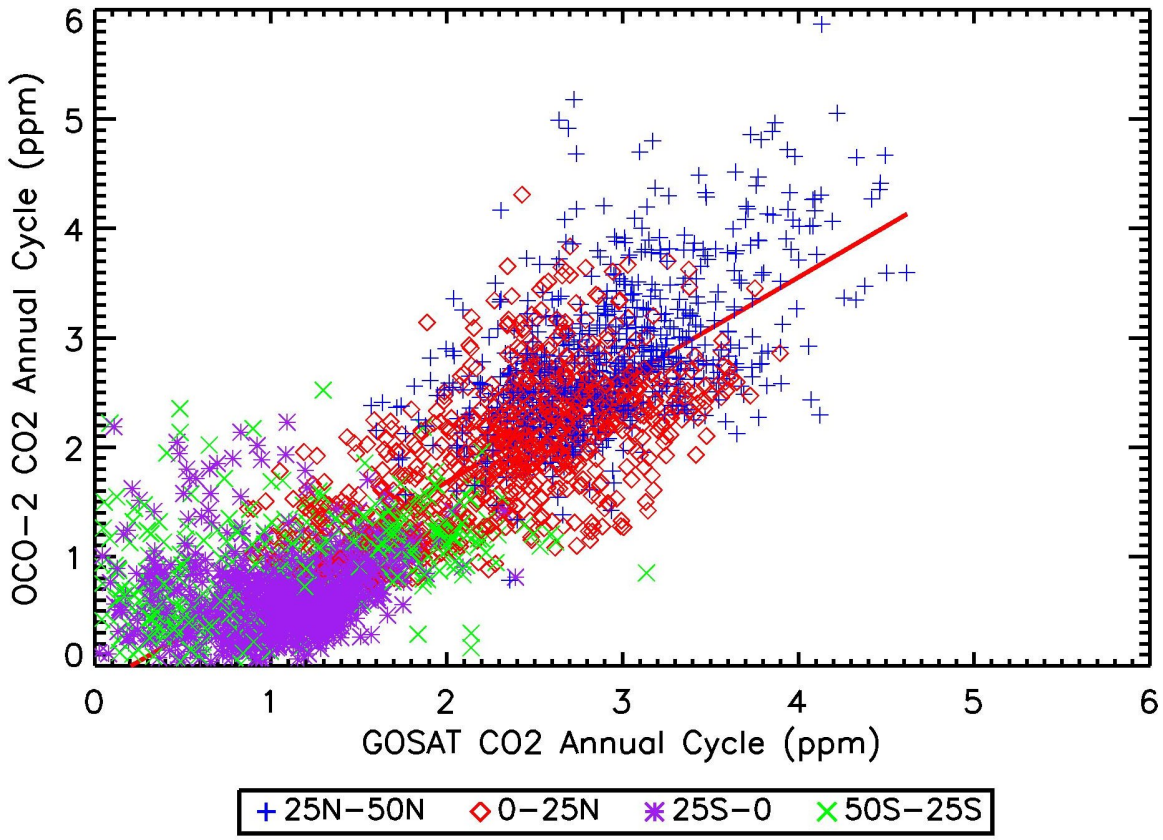

Figure 3.5: Comparison of CO_2 annual cycle amplitudes between GOSAT and OCO-2. Units are ppm. Data at different latitude bands are plotted as different symbols. Red line is a linear fit of the scatter plot.

Finally, the CO_2 annual cycle amplitude was studied as a function of latitude, as presented in Figure 3.6. CO_2 annual cycles from OCO-2 column CO_2 and GOSAT column CO_2 were compared to those from other CO_2 data sets, such as surface CO_2 measurements from NOAA-ESRL, TCCON column CO_2, AIRS mid-tropospheric CO_2, and TES mid-tropospheric CO_2. As shown in Figure 3.6, the CO_2 annual amplitude is larger in NOAA-ESRL surface CO_2 data than any of the studied remotely satellite-retrieved CO_2 annual cycle amplitudes and TCCON column CO_2 annual cycle amplitude. This is because the CO_2 annual cycle is related to CO_2 exchange between the biosphere and atmosphere, thus the CO_2 annual cycle

amplitude is the largest at the surface. The CO_2 annual cycle amplitudes are ~5-10 ppm for the NOAA-ESRL surface CO_2 in the Northern Hemisphere. The annual cycle amplitudes of the OCO-2 column CO_2 are consistent with those from GOSAT column CO_2 and TCCON column CO_2 in the Northern Hemisphere with amplitudes of 2-3 ppm. The Northern HemisphericHemispheric CO_2 annual cycle amplitude is smallest in the AIRS mid-tropospheric CO_2 with amplitudes of 1-2.5 ppm.

All data sets show higher annual cycle CO_2 amplitudes in the Northern Hemisphere when compared to the Southern Hemisphere values. AIRS (blue line in Figure 3.6) retrieved the lowest annual cycle of CO_2 at all latitudes other than 45^o S, where TCCON CO_2 calculated the lowest annual CO_2 cycle. TES (red line in Figure 3.6), GOSAT (green line in Figure 3.6), and OCO-2 (black line in Figure 3.6) all demonstrated similar CO_2 annual cycles. In the Southern Hemisphere, the annual CO_2 cycle amplitudes are much smaller, when compared to the Northern Hemisphere. Since the CO_2 annual cycle amplitudes are small in the Southern Hemisphere, the differences of CO_2 annual cycle amplitudes between different satellite CO_2 retrievals are correspondingly small.

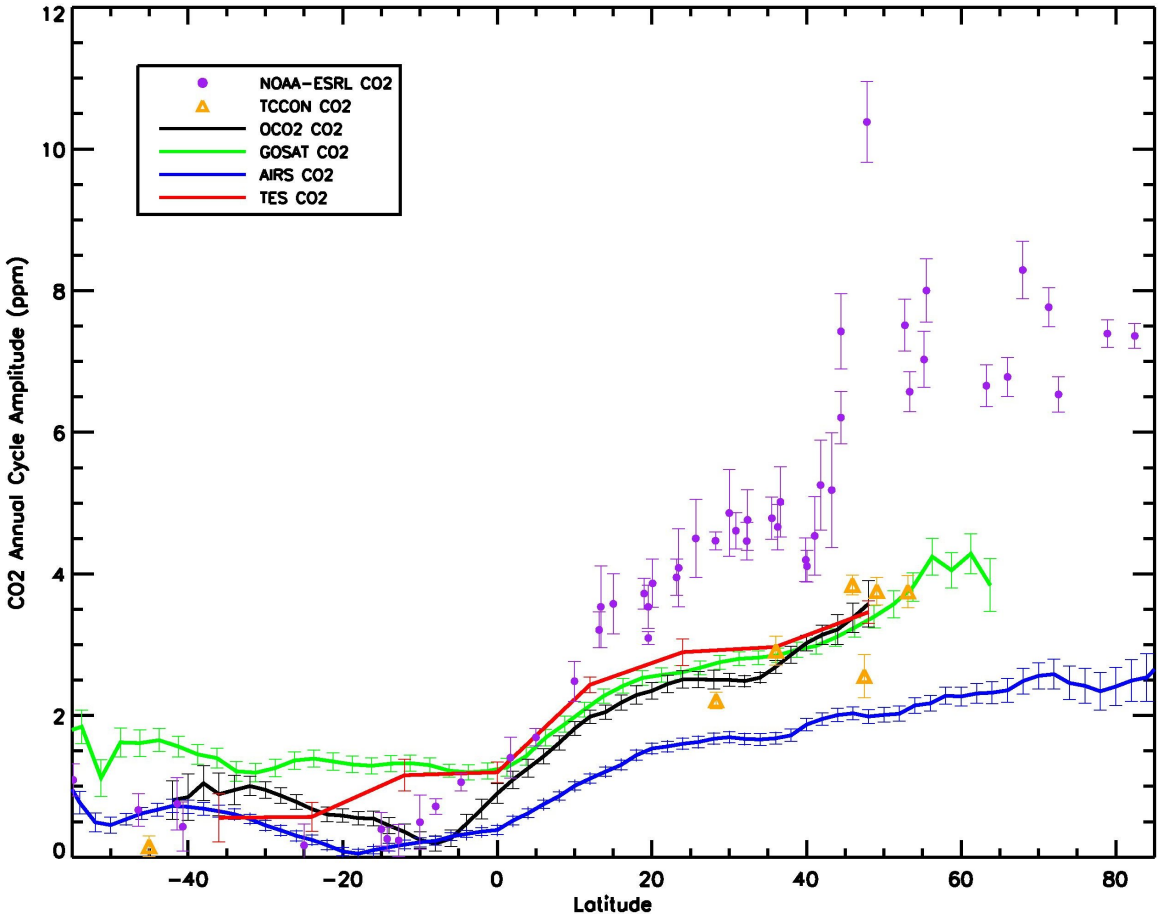

Figure 3.6: Latitudinal distributions of CO_2 annual cycle amplitudes. Black lines are results from OCO-2 X_{CO2}. Green lines are results from GOSAT X_{CO2}. Red lines are results from TES mid-tropospheric CO_2. Blue lines are results from AIRS mid-tropospheric CO_2. Purple dots are results from NOAA-ESRL surface CO_2. Orange triangles are results from TCCON X_{CO2}. Error bars are the uncertainties of CO_2 annual cycle amplitudes derived from the multiple regressions.

3.5 Conclusions

Recent satellite CO_2 retrievals allow a new opportunity to study CO_2 variability at different altitudes [*Crisp et al.,* 2012*; Chahine et al.,* 2008*; Kulawik et al.,* 2010]. In this chapter, the annual cycle and trend of CO_2 using GOSAT and OCO-2 satellite retrievals was analyzed. A multiple regression method was utilized to decompose CO_2 data to trend, annual cycle, and semi-annual cycle. Positive CO_2

trends were seen in the GOSAT column CO_2 data with amplitudes between 1.8 to 2.5 ppm/year. CO_2 trends are larger over the land than the ocean, because there are higher levels of CO_2 surface emissions over the land than the ocean. The CO_2 annual cycle amplitudes from OCO-2 and GOSAT column CO_2 were estimated. GOSAT column CO_2 annual cycle amplitudes are slightly higher than those from OCO-2 column CO_2.

The latitudinal distribution of CO_2 annual cycle amplitudes from different data sets (e.g., OCO-2 column CO_2, GOSAT column CO_2, TCCON column CO_2, NOAA-ESRL surface CO_2) was estimated. The CO_2 annual cycle amplitudes are consistent among OCO-2 column CO_2, GOSAT column CO_2, and TCCON column CO_2. The magnitude of column CO_2 annual cycle is smaller than those in the NOAA-ESRL surface CO_2 data. The CO_2 annual cycle amplitudes are smallest in the AIRS mid-tropospheric CO_2 in the Northern Hemisphere. The amplitudes for the CO_2 annual cycle from OCO-2, GOSAT, TCCON, AIRS, TES, and NOAA-ESRL CO_2 are small and comparable to each other in the Southern Hemisphere. The CO_2 annual cycle amplitudes are larger in the Northern Hemisphere than that in the Southern Hemisphere. Results obtained in this study can help us better understand the information contents of the satellite CO_2 retrievals and vertical structure for the CO_2 annual cycle. These results can also help better understand the interaction between biosphere and atmosphere and how the CO_2 annual cycle change as a function of altitudes.

3.6 Acknowledgments

AIRS Version 6 CH_4 data are available at http://disc.sci.gsfc.nasa.gov/AIRS/data-holdings. GOSAT data is available at from http://disc.sci.gsfc.nasa.gov/acdisc/data-holdings/acos-data-holdings. The OCO-2 column CO_2 are available at http://disc.sci.gsfc.nasa.gov/uui/dataset?keywords=OCO%20ACOS. This project is supported by NASA grants NNX13AC04G, NNX13AK34G, NNX16AG46G, and NNX15AI85G.

Chapter 4: Analysis of Solar-Induced Fluorescence (SIF), Carbon Dioxide, and Water Using OCO-2 and TRMM

4.1 Introduction

It is necessary to identify and quantify the spatiotemporal patterns of variability of CO_2 to further study global CO_2 sources and sinks associated with anthropogenic contributions. Continuous and global-distributed data gives scientists the opportunity to explore CO_2 variability at different time scales, as well as to identify CO_2 correlations with precipitation, along with interactions with the biosphere.

When plants are healthy and active, they engage in photosynthesis, absorbing sunlight and carbon dioxide to produce food for the plant and oxygen as a byproduct. The biosphere as a whole, acts as a carbon sink for anthropogenic CO_2 [*Pearman and Hyson,* 1980, 1981]. The chlorophyll in leaves absorbs sunlight that then creates food, is lost as heat, or is absorbed light that is then reemitted as near-infrared light. This reemitted light is measured by OCO-2 and is called solar-induced fluorescence, or SIF. SIF data provides a direct, physiology-based measure of global photosynthesis activity [*Frankenberg et al.,* 2011] Satellite-based detection of solar-induced florescence is an important remote sensing tool used to assess the biosphere and to monitor the environment [*Raychaudhuri* 2014]. Chlorophyll molecules of active green plants exhibit fluorescent emissions in red and near-infrared wavelengths when

excited by radiation of shorter wavelengths, such as that of solar radiation [*Papageorgiou et. al*., 2004; *Baker et. al.,* 2008]. SIF lends a keen insight into the physiological property of vegetation and can be correlated with photosynthetic activity, and furthermore, is correlated with the oxygencarbon dioxide balance in the atmosphere [*Raychaudhuri* 2014].

Estimating SIF from any distance is challenging due to the weak signal. Space- based detection of SIF is currently growing in popularity due to its revolutionary correlations and analysis potential. Current space-based measurement techniques include Medium Resolution Imaging Spectrometer (MERIS) sensor of the Environmental Satellite Platform [*Guanter el al.,* 2007] and Fourier Transform Spectrometer sensor of Greenhouse Gases Observing Satellite (GOSAT) platform [*Joiner et al.,* 2011; *Guanter et al.,* 2012] and more recent satellite sensors like OCO-2, which was used in this research. [*Frankenberg et al.,* 2014]

Recently, it has been shown that the OCO-2 can measure SIF as a proxy for gross primary production (GPP, carbon uptake through photosynthesis) accurately from space using high spectral resolution radiances in the 750 nm range from the Japanese GOSAT and European GOME-2 instruments [*Frankenberg et al.,* 2014]. Photosynthesis uptake of carbon dioxide by vegetation is driven by photosynthetically active radiation absorbed in the 400 – 700 nm wavelength region. Once absorbed, it can then to reemitted as heat, or a small fraction is reemitted at longer wavelengths (660- 800 nm). This reemitted energy, or solar-induced fluorescence, has been widely

used in photosynthesis research for decades and can lead to more mechanistic understanding of ecosystem carbon exchange [*Frankenberg, Fisher et al.,* 2011]

In the past, SIF data was retrieved using high-resolution spectra of the oxygen A-band region from the Tanso Fourier Transform Spectrometer onboard of the Japanese GOSAT satellite [*Hamazak et al.,* 2005; *Kuze et. al.,* 2009]. Later, Joiner et al., [2012] proved that even moderate spectral resolution can be used to infer SIF using either a very broad solar absorption features at the 866 nm or applying a larger spectral range from 715 to 780 nm using GOME-2 [*Joiner et al.,* 2013]. Usually, there was a trade-off between spectral resolution and spatiotemporal sampling. On one side, high spectral resolution leads to robust and accurate SIF retrievals, but conversely, it limits sample size [*Frankenburg et al.,* 2014]. GOSAT retrievals, for example, are well characterized but cannot provide the spatial mapping of GOME-2. OCO-2 does not provide full spatial mapping even though it records about 8 times more spectra than GOME-2. GOSAT SIF retrievals have been helpful in the analysis of carbon exchange in the tropical Amazon [*Lee et al.,* 2013; *Parazoo et. al.,* 2013].

The OCO-2 data will alleviate some of the shortcomings of the current SIF data by combining the advantages of GOSAT and GOME-2. OCO-2 will acquire 24 spectra per second instead of one every 4 seconds; this about 100-fold increase in data density when compared to GOSAT is also combined with much smaller ground-pixels. Therefore, OCO-2 has the potential to significantly advance SIF retrievals [*Frankenberg et al.,* 2014].

4.2 Methodology and Data

4.2.1 Tropical Rainfall Measuring Mission (TRMM) precipitation data

Tropical Rainfall Measuring Mission (TRMM) precipitation will be used in this chapter. TRMM data is available from 1998 to present at latitudes 50^{o}N –50^{o}S. The data has a 3-hour temporal resolution and a horizontal resolution 0.25^{o} x 0.25^{o} in latitude x longitude. TRMM calibrated precipitation data combine precipitation estimates from gauge data and different instruments, such as the Microwave Imager (TMI), Special Sensor Microwave Imager (SSM/I), the Advanced Microwave Scanning Radiometer-Earth Observing System (AMSR-E), and the Advanced Microwave Sounding Unit-B (AMSU-B) [*Huffman et al*., 2007].

4.2.2 OCO-2 SIF data

Solar-induced fluorescence, or SIF, will be used to investigate CO_2 contributions from the biosphere. SIF data from OCO-2 will be used to study the vegetative photosynthesis process in this chapter. OCO-2 is a 3-channel grating spectrometer in a sun-synchronous orbit. It has a 3 Hz readout rate and will record high-resolution spectra of the O_2 A-band, a weak CO_2 band, and a strong CO_2 band with eight independent along-slit focal plane array readouts. OCO-2 has a spatial footprint of 1.3 x 2.25 km^2 with all eight individual footprints covering a 10.3 km full swath width. The recent SIF data from OCO-2 provides a direct, physiology-based measure of global photosynthesis activity [*Frankenberg et al*., 2011]. Plants absorb radiation at 400-700 nm wavelength to drive photosynthesis, and then re-radiate

radiation at 660-800 nm, which is called fluorescence. Satellite can measure the fluorescence signal at Fraunhofer lines within 660-800 nm [*Frankenberg et al*., 2011]. A Singular Value Decomposition (SVD) fluorescence fitting approach is used to enable fast retrievals and determining singular vectors explaining most of the variances. Then, a least square fitting technique is used to retrieve SIF from OCO-2 instrument [*Frankenberg et al*., 2011; *Frankenberg et al*., 2014].

OCO-2 SIF data are available from September 2014 to present. SIF data has a latitude (longitude) resolution of 2.25 km (1.29 km) and a temporal resolution of 16 days. SIF data can be downloaded at https://oco.jpl.nasa.gov/science/OCO2DataCenter/. Interactive OCO-2 SIF data is available at http://habitable-planet.caltech.edu/gpps/Apps/gppis.html.

4.2.3 Column CO_2 Retrievals from OCO-2

The OCO-2 instrument provides CO_2 with precision, resolution, and coverage needed to characterize CO_2 sources and sinks on the regional scale [*Crisp et al.*, 2004; *Miller et al.*, 2007]. It employs high-resolution spectra of reflected sunlight taken simultaneously in near-infrared (NIR) CO_2 (1.58-μm and 2.06-μm) and O_2 (0.76-μm) bands to retrieve the column-averaged CO_2 dry air volume-mixing ratio X_{CO2} from space [*Kuang et al*., 2002; *Crisp et al*., 2004]. Precision for the OCO-2 CO_2 measurements is approximately 0.3% (1 ppm) [*Miller et al.*, 2007]. The OCO-2 column CO_2 mixing ratios are available from September 2014 to present. The column CO_2 data from the OCO-2 has a latitude (longitude) resolution of 2.25 km (1.29 km)

and a temporal resolution of 16 days. OCO-2 column CO_2 are available at http://disc.sci.gsfc.nasa.gov/uui/datasets?keywords=OCO%20ACOS.

4.2.4 ECMWF Evaporation data

Evaporation data from European Centre for Medium-Range Weather Forecasts (ECMWF) is used in this chapter. ECMWF evaporation data is available from 1979 to present covering from 90^oN- 90^oS. It has a 3-hour temporal resolution and a horizontal resolution 0.75^o x 0.75^o in latitude x longitude. ECMWF evaporation data are available at http://apps.ecmwf.int/datasets/data/interim-full-daily/levtype=sfc/.

4.3 Results

Since SIF represents the photosynthesis from the biosphere and photosynthesis is the major sink for atmospheric CO_2, we explore the relationship between SIF and atmospheric CO_2 in different seasons (JFM and JJA). To understand the relationship between SIF and CO_2 in January, February, and March, OCO-2 SIF data from January to March in 2015 and 2016 was averaged (Figure 4.1a) and the OCO-2 CO_2 from January to March in 2015 and 2016 (Figure 4.1b). During January, February, and March, the Northern Hemisphere is experiencing winter, while the Southern Hemisphere is experiencing summer. During summers, the biosphere is more productive while plants grow under the seasonally sunny conditions. In Figure 4.1, high OCO-2 SIF values can be seen in the Southern Hemisphere, from the

equator to about 40° S. Similarly, low atmospheric CO_2 values can be seen in Figure 4.1b in the SH from the equator to around 40°S. This is congruent with the understanding of the biosphere's interaction with the carbon cycle. During January, February, and March the Northern Hemisphere is experiencing winter, therefore the biosphere is less productive, and consequently SIF values were expected to be low. When plants are not undergoing photosynthesis, SIF levels will be low, as will the uptake of CO_2; therefore, leading to a higher levels of atmospheric CO_2, as shown in Figure 4.1b.

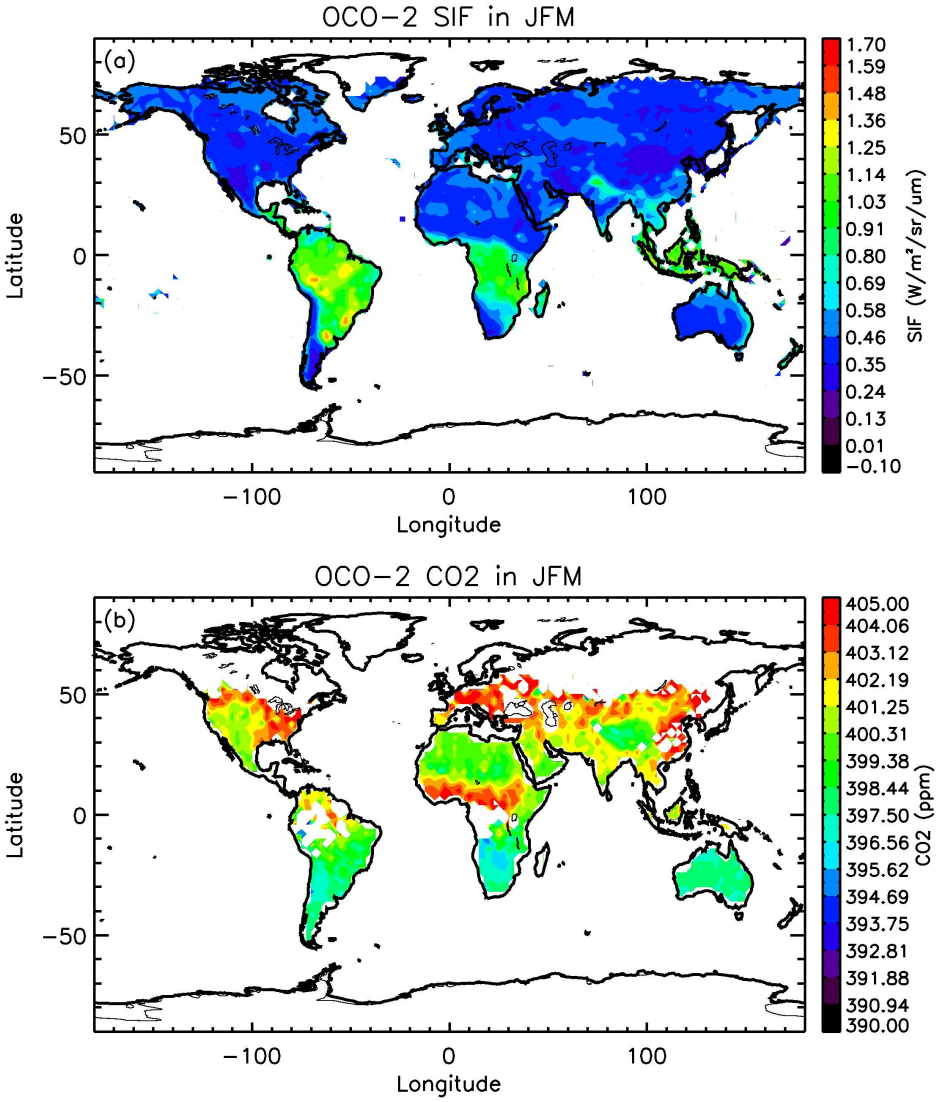

Figure 4.1: (a) OCO-2 SIF data averaged from January to March in 2015-2016. Units are W/m^2/sr/µm. (b) OCO-2 column CO_2 data averaged from January to March in 2015-2016. Units are ppm.

In Figure 4.2, SIF and CO_2 were averaged in June, July, and August from 2015-2016. During these months, the Northern Hemisphere experiences summer, where the biosphere is productive so SIF values are expected to be high. Figure 4.2a, shows exactly that, high SIF data in the Northern Hemisphere during June, July, and August from about the equator to 60^{o}N. Conversely, Figure 4.2b shows low

atmospheric CO_2 values in the Northern Hemisphere. This is due to the active photosynthesis from the biosphere acting as a carbon sink. The Southern Hemisphere experiences winter during June, July and August, therefore, the biosphere is inactive. As shown in Figure 4.2a, SIF data is low in the Southern Hemisphere.

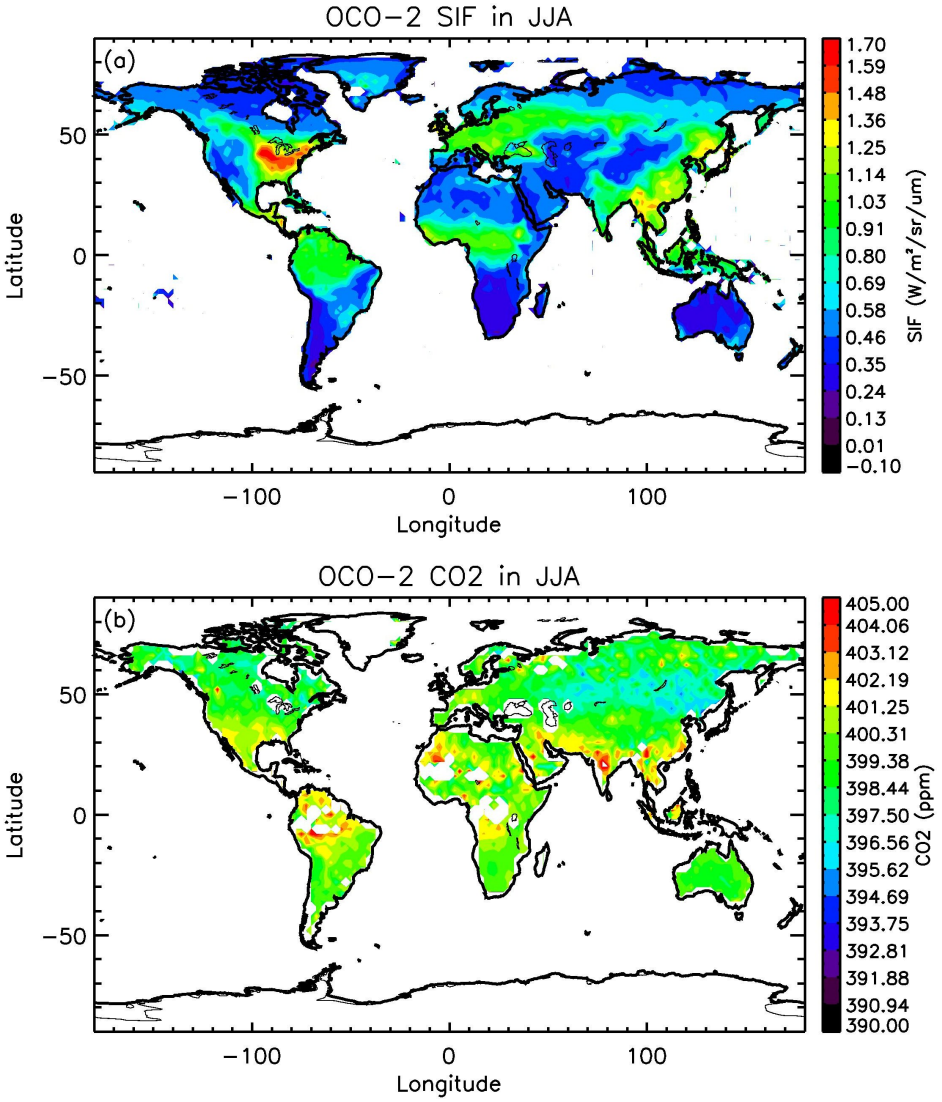

Figure 4.2: (a) OCO-2 SIF data averaged from June to August in 2015-2016. Units are $W/m^2/sr/\mu m$. (b) OCO-2 column CO_2 data averaged from June to August in 2015-2016. Units are ppm.

Because the photosynthesis is related to water available to plants, we compared SIF in January, February, and March to available water. Available water is estimated as the difference between TRMM precipitation and ECMWF evaporation. In Figure 4.3b, precipitation minus evaporation, measured in mm/month, are averaged over January, February, and March in 2015 and 2016. When there is more precipitation than evaporation (e.g., Southern Hemisphere in Figure 4.3b), there are high SIF values in the Southern Hemisphere as shown in Figure 4.3a. This is due to the fact that plants will be more photochemically productive and healthy when there is more water available.

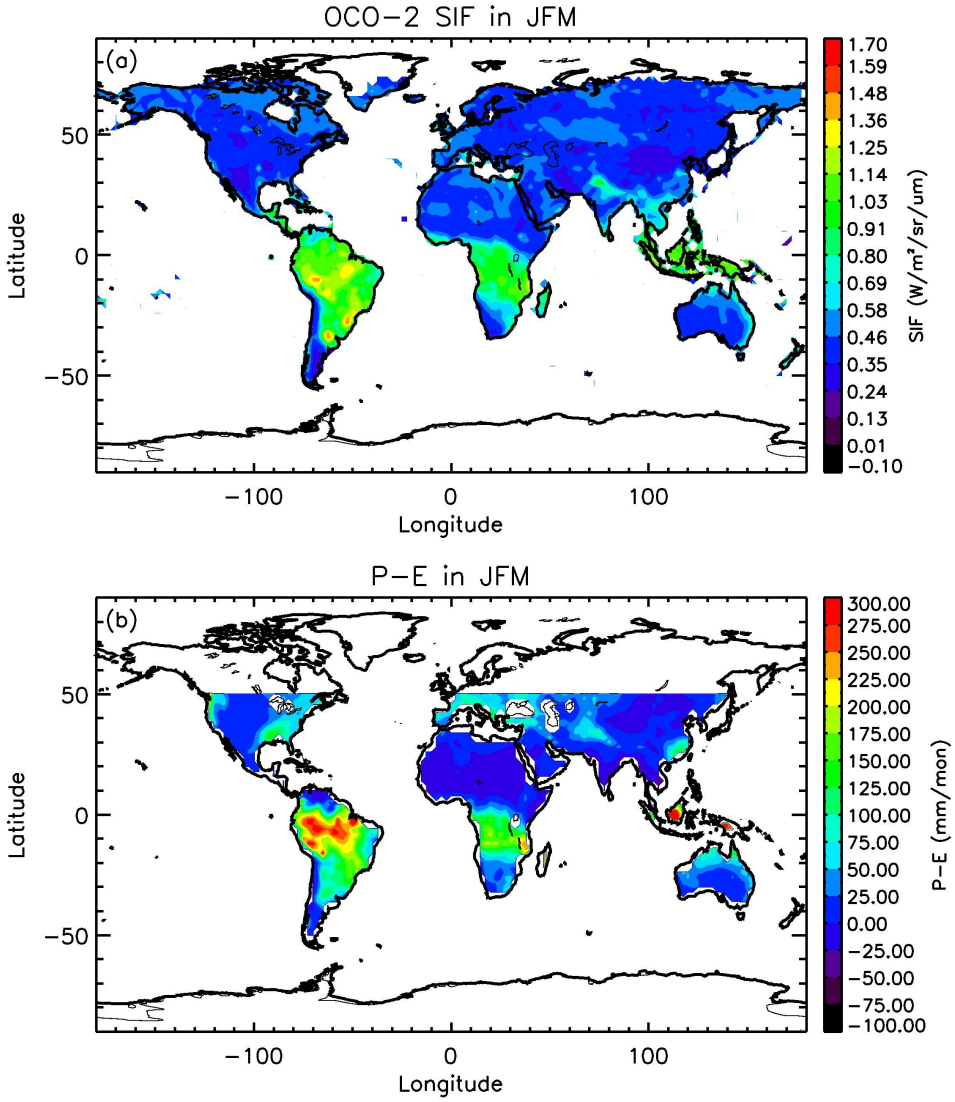

Figure 4.3: (a) OCO-2 SIF data averaged from January to March in 2015-2016. Units are W/m^2/sr/µm. (b) Difference of precipitation and evaporation averaged from January to March in 2015-2016. Units are mm/month.

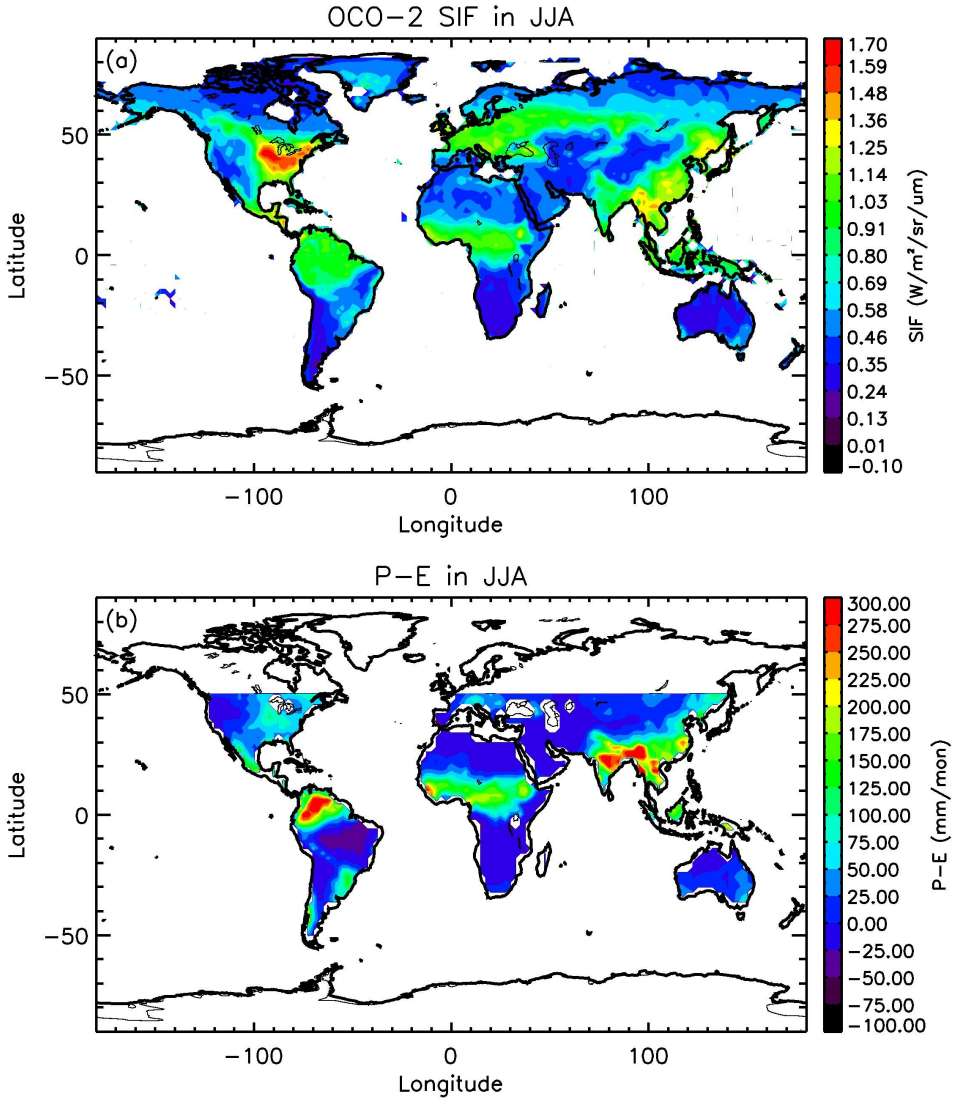

Figure 4.4: (a) OCO-2 SIF data averaged from June to August in 2015-2016. Units are W/m^2/sr/µm. (b) Difference of precipitation and evaporation averaged from June to August in 2015-2016. Units are mm/month.

SIF and available water was additionally compared in June, July, and August of 2015 and 2016. Results are shown in Figure 4.4. As shown in Figure 4.4b, there is more precipitation than evaporation over some regions (e.g., North America and Southeast Asia) in the Northern Hemisphere. As a result, the SIF values are high over these regions.

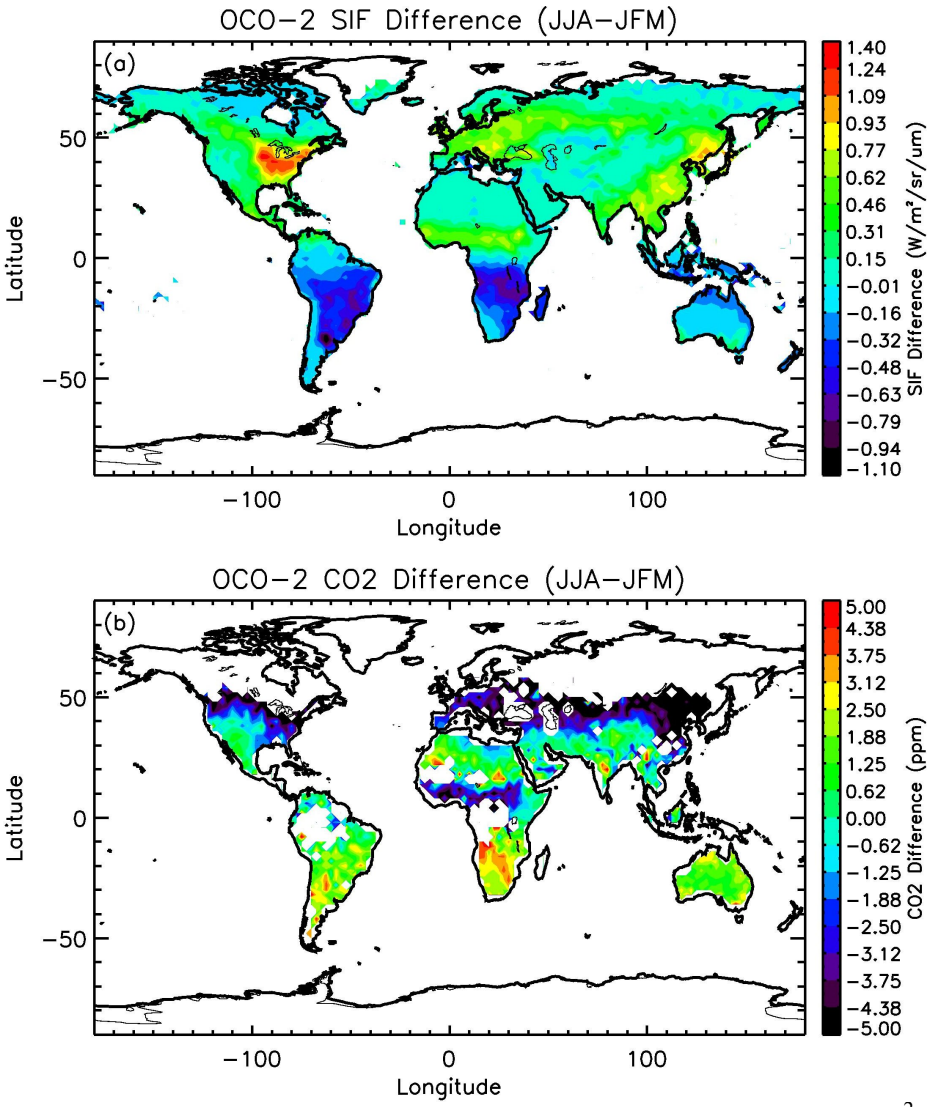

Figure 4.5: (a) OCO-2 SIF difference between JJA and JFM. Units are W/m^2/sr/μm. (b) OCO-2 column CO_2 difference between JJA and JFM. Units are ppm.

To better reveal the relationship between SIF and atmospheric CO_2, OCO-2 SIF difference and OCO-2 CO_2 difference between June-August and January-March were explored. Results are shown in Figure 4.5. As shown in Figure 4.5a, SIF difference (JJA-JFM) is positive over Northern Hemisphere, which suggest that there is more photosynthesis from biosphere during Northern Hemispheric summer season (JJA) than Northern cHemispheric winter season (JFM). SIF difference (JJA-JFM) is

negative over the Southern Hemisphere, which implies there is less photosynthesis from biosphere during Southern Hemispheric winter (JJA). Since SIF represents the photosynthesis, more SIF suggests more CO_2 uptake from biosphere, thus less CO_2 remaining in the atmosphere. As a result, OCO-2 column CO_2 difference (JJA-JFM) demonstrates negative value in the Northern Hemisphere, which results from more CO_2 uptake by photosynthesis over Northern Hemispheric summer (JJA) as shown in Figure 4.5b. The OCO-2 column CO_2 difference (JJA-JFM) is positive in Southern Hemispheric winter, which suggests there is less CO_2 uptake in the Southern Hemisphere winter (JJA).

A scatter plot was also created of SIF difference and CO_2 difference in Figure 4.6. There is a negative correlation between OCO-2 SIF difference (JJA-JFM) and OCO-2 CO_2 difference (JJA-JFM). SIF difference (JJA-JFM) is positive over North America and Asia, which means there is more CO_2 uptake due to the photosynthesis during JJA than JFM. As a result, there is less atmospheric CO_2 over North America and Asia. SIF difference (JJA-JFM) is negative over South America and Australia, which means there is less SIF (photosynthesis) during JJA than JFM over South America and Australia. As a result, there is more atmospheric CO_2 over South America and Australia during JJA than JFM.

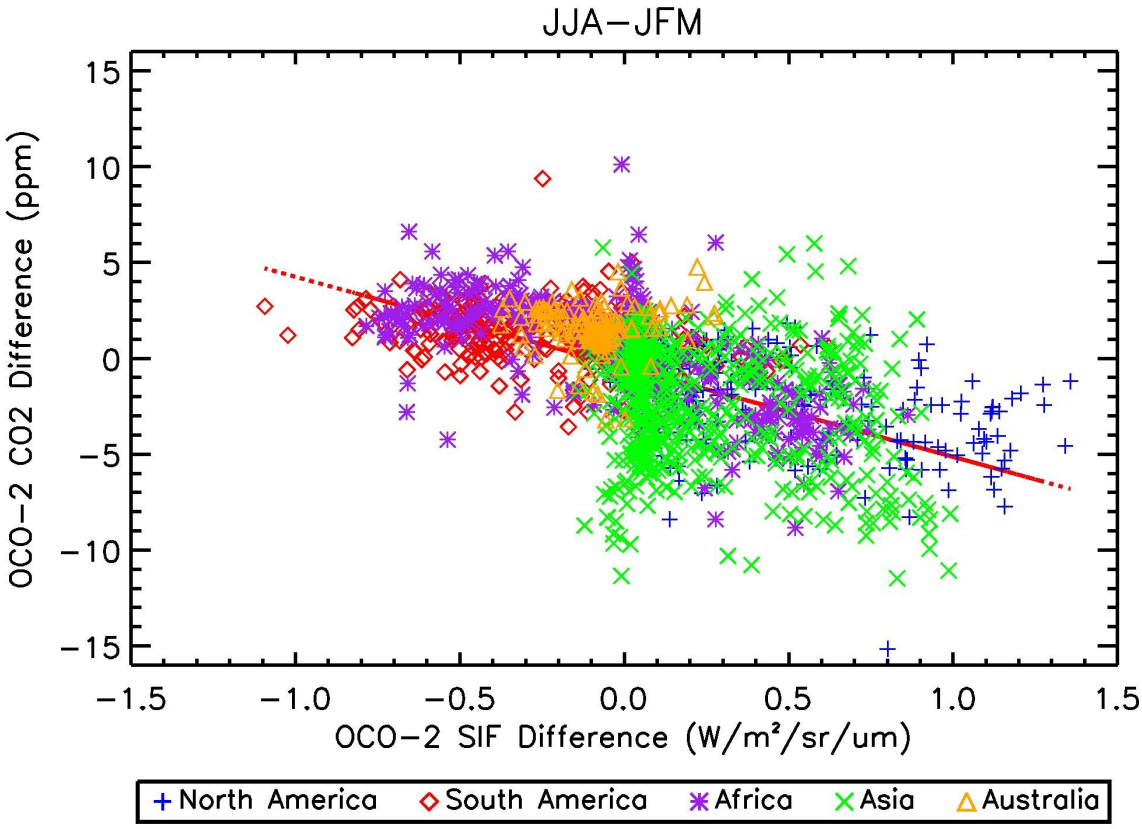

Figure 4.6: Scatter plot of OCO-2 SIF difference and OCO-2 column CO_2 difference between JJA and JFM.

Since photosynthesis is related to the amount of water available to the plants, we also explored the OCO-2 SIF difference versus available water difference for different seasons. The spatial patterns of SIF difference (JJA-JFM) and available water difference (JJA-JFM) are shown in Figure 4.7. As shown in Figure 4.7a, SIF difference (JJA-JFM) is positive over Northern Hemisphere, for there is more photosynthesis during JJA than JFM. There is more water available in the Northern Hemisphere in JJA than JFM, which will contribute to the positive SIF anomalies shown in Figure 4.7a.

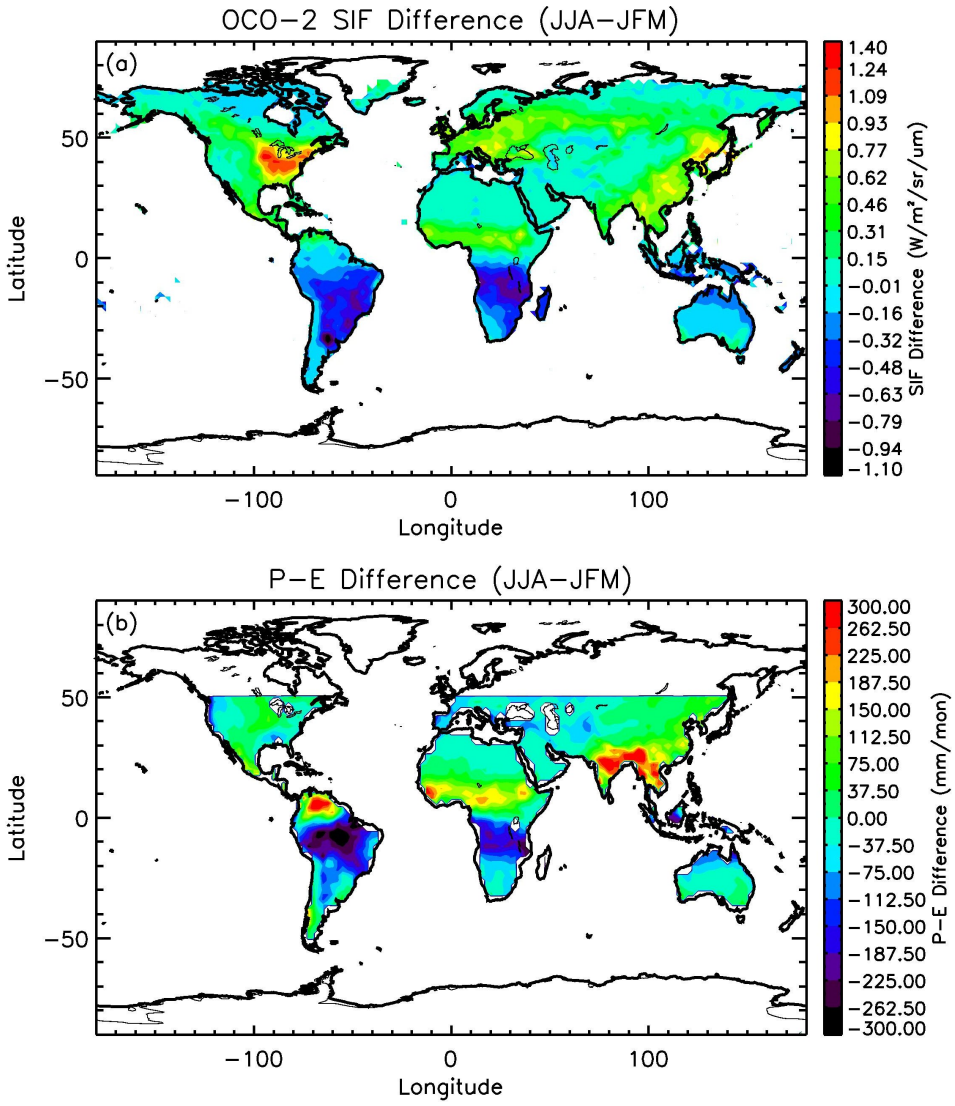

Figure 4.7: (a) OCO-2 SIF difference between JJA and JFM. Units are W/m^2/sr/μm. (b) Precipitation - Evaporation difference between JJA and JFM. Units are mm/month.

A further exploration is shown in the scatter plot of SIF difference (JJA-JFM) and available water (JJA-JFM). Result are shown in Figure 4.8. There is a positive correlation between SIF and precipitation and evaporation difference. SIF difference

(JJA-JFM) is positive when there is more precipitation than evaporation, suggesting there is more photosynthesis when there is more water available.

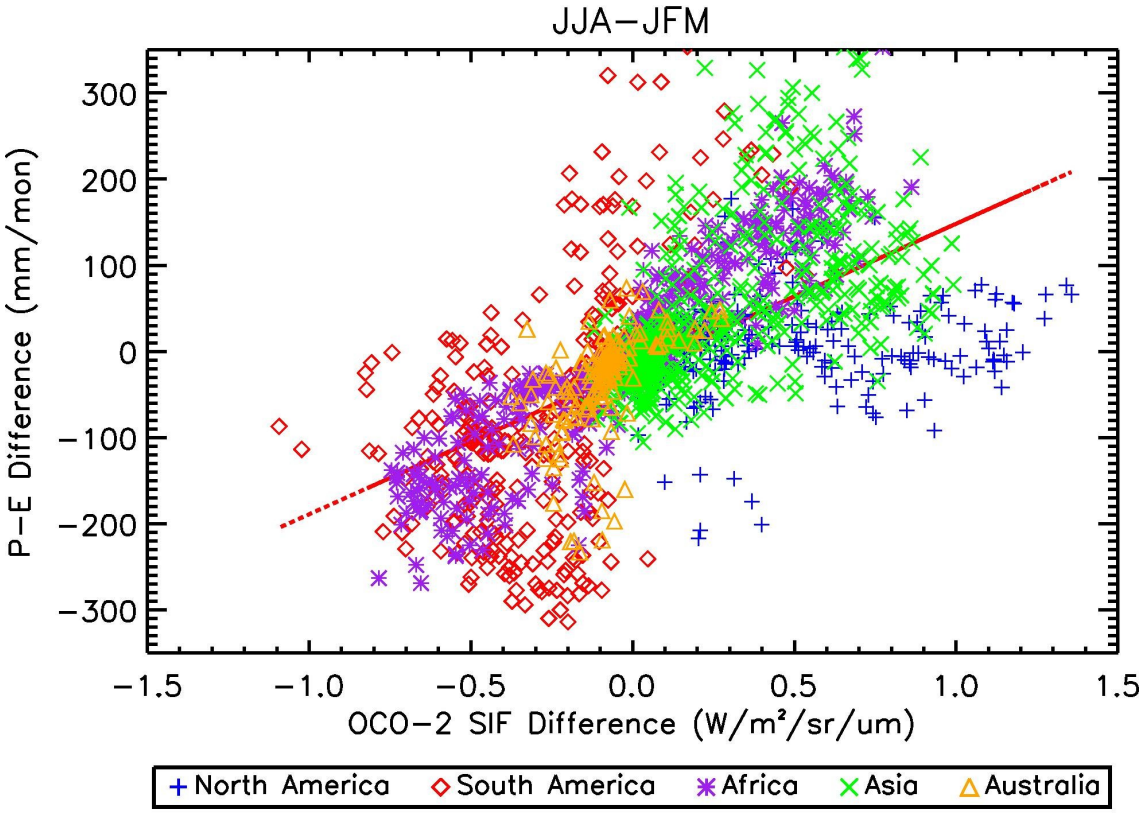

Figure 4.8: Scatter plot of OCO-2 SIF difference and (Precipitation – Evaporation) difference between JJA and JFM.

4.5 Conclusions

CO_2 uptake by photosynthesis will lead to high SIF value, which will further decrease atmospheric CO_2 concentrations. A high level of anti-correlation is found between SIF and atmospheric CO_2 retrievals from OCO-2. SIF is higher (lower) in JJA in the Northern Hemisphere (Southern Hemisphere). SIF has a positive

correlation with (Precipitation – Evaporation), meaning when there is high available water for plants, there is more SIF.

4.6 Acknowledgements

This project is supported by NASA grants NNX13AC04G, NNX13AK34G, NNX16AG46G, and NNX15AI85G. There is an interactive OCO-2 SIF data at http://habitable-planet.caltech.edu/gpps/Apps/gppis.html. ECMWF evaporation data are available at http://apps.ecmwf.int/datasets/data/interim-full-daily/levtype=sfc/.

.

Chapter 5: Modulation of Mid-tropospheric Methane by El Niño

Corbett, A., X. Jiang, X. Xiong, A. Kao, and L. Li (2017), Modulation of midtropospheric methane by El Niño, Earth and Space Science, 4, doi:10.1002/2017EA000281.

5.1 Introduction

As one of the most important greenhouse gases, methane (CH_4) is ~28 times more effective than carbon dioxide in heating the atmosphere [*Myhre et al*., 2014]. CH_4 also has an important role in atmospheric chemistry [*Myhre et al*., 2014]. Anthropogenic sources of CH_4 include fossil fuel production and distribution, agriculture and livestock, biomass burning, and landfills [*Myhre et al*., 2014]. Removal of CH_4 from the atmosphere includes reactions with the hydroxyl radical and free chlorine [*Platt et al*., 2004; *Allen et al*., 2005; *Born et al*., 1990].

Global CH_4 ground-based measurements have been recorded since early 1980s, but due to the inconsistent spatial grid and extremely difficult measurement conditions, ground-based measurements are limited spatially and cannot adequately represent the global concentrations [*Dlugokencky et al*., 1994]. Additionally, ground-based measurements left many locations across the globe unmeasured, one particularly noteworthy example are the oceans [*Dlugokencky et al*., 1994; *Dlugokencky et al*., 1995]. NOAA/GMD operated 40 surface measurements of CH_4

over the globe, which resulted in a global average CH_4 concentration ~1,774.62±1.22 ppb [*Dlugokencky et al.,* 2005]. Measurements of atmospheric CH_4 concentration report an increase over a twenty-year period; however, the growth rate of CH_4 is not constant [*Dlugokencky et al*., 2003]. For example, the growth rate of CH_4 has decreased substantially from the 1970s and early 1980s and had a significant increase during 1998 [*Blake et al*., 1988]. Dlugokencky et al. [2003] attributes the increase in concentration in 1998 to the boreal biomass burning emission, which is further correlated to the warmest surface temperature in 1998 [*Dlugokencky et al*., 2003]. Additionally, Butler et al. [2005] also suggests unusually high biomass burning contributed to the rise in 1998. The increase in methane concentration was low after 2000 [*Dlugokencky et al*., 2003] but then rapidly increased in 2007 [*Bousquet et al*., 2011]. As suggested by two atmospheric inversions, a positive anomaly of tropical emission is a contributor for the global CH_4 emission anomalies (~60-80%) in 2007 [*Bousquet et al*., 2011]. In addition, increased CH_4 emissions from wetlands and fossil fuel production and combustion could also be a contributing factor in the rapid increase of methane concentrations in 2007 [*Kirschke et a*l., 2013]. Using satellite retrievals and surface observations, it has been found that CH_4 emissions increased >30% in the United States from 2002 to 2014 [*Turner et al*., 2016].

Global space-borne measurements allow the study of global variations of CH_4 with a better spatial coverage than ever before. Additionally, satellite measurements allow a better understanding of the vertical variation of CH_4. More knowledge of the changes in vertical structure of CH_4 can help us better understand its impacts on

current and future climate change. Schoeberl et al. [1995] and Park et al. [2004] utilized CH_4 data from the Halogen Occultation Experiment (HALOE) and found CH_4 seasonal cycle in the tropopause region. CH_4 measurements are available from many different satellites, including ADEOS, GOSAT, SCIAMACHY, AIRS, and IASI [*Clerbaux et al*., 2003; *Frankenberg et al*., 2005; *Frankenberg et al*., 2006; *Xiong et al*., 2008; *Razavi et al*., 2009; *Saitoh et al*., 2012; *Crevoisier et al*., 2013; *Xiong et al*., 2013].

Zhang et al. [2011] used CH_4 data from the Atmospheric Infrared Sounder (AIRS) to study mid-upper tropospheric methane and determined AIRS CH_4 agrees well with the Fourier transform infrared profiles in China [*Zhang et al*., 2011]. Xiong et al. [2009] found a strong CH_4 plume in the middle troposphere during South Asia monsoon seasons (July-September), providing evidence of strong upward transport moving CH_4 from the surface to middle troposphere [*Xiong et al*., 2009]. Results in Xiong et al. [2009] are further confirmed with the model tracer model version 3 (TM3), later satellite observations from IASI, and CARIBIC aircraft measurements [*Xiong et al*., 2009; *Crevoisier et al*., 2009; *Schuck et al*., 2012]. Enhanced upper tropospheric CH_4 anomalies were also seen during the TACTS aircraft campaign, which sampled from the surface to the upper troposphere during the South Asia monsoon season [*Vogel et al*., 2014].

El Niño-Southern Oscillation (ENSO) has an important influence on large-scale wind patterns, temperature, pressure, precipitation, and trace gases [*Gage et al.*, 1987; *Jiang et al*., 2010; 2013]. It was found that ENSO could influence

concentrations of CO_2 and ozone [*Jiang et al*., 2010; *Wang et al*., 2011]. However, there is no previous analysis on exploring the influence of ENSO on CH_4 in the middle troposphere. In this chapter, we explored possible relationships between ENSO and AIRS mid-tropospheric CH_4 for the first time.

5.2 Data

5.2.1 AIRS

In this study, AIRS Version 6 CH_4 data at 400 hPa was used to study possible relationship between ENSO and CH_4 in the middle troposphere. AIRS is an infrared spectrometer, which has 2378 channels at 649-2674 cm^{-1} [*Aumann et al*., 2003]. The satellite passes the equator twice a day at 1:30 AM and 1:30 PM local time [*Pagano et al*., 2003]. In addition to temperature [*Aumann et al*., 2003] and cloud cover [*Kahn et al*., 2014], AIRS also provides trace gas data products such as H_2O, CH_4, CO_2, and CO [*Fetzer et al*., 2006; *Xiong et al*., 2010, *Chahine et al*., 2008; *Warner et al*., 2014]. Channels near 7.6 μm are chosen to retrieve CH_4, which is the best channel and is most sensitive to the mid-tropospheric CH_4 retrieval [*Xiong et al*., 2008]. AIRS CH_4 data provides a global measurement of CH_4 about twice a day. AIRS methane data has already been validated by *insitu* aircraft observations and it agrees well with the aircraft data [*Xiong et al*., 2008; 2015]. Therefore, the retrievals of CH_4 from AIRS can help us better understand CH_4 global distributions and variations.

Linear trend and annual cycle will be removed from AIRS mid-tropospheric CH_4 data. To identify El Niño or La Niña months, the Southern Oscillation Index (SOI), defined by the difference of the sea level pressure between two locations

(Tahiti and Darwin, Australia) over the Pacific Ocean, will be used to identify El Niño or La Niña months from September 2002 to December 2014. When the SOI index is below (above) the mean value by one standard deviation of the SOI, the events are classified as an El Niño (La Niña) event.

5.2.2 HIPPO

In addition to AIRS mid-tropospheric CH_4 data, we will also analyze CH_4 aircraft profiles from the HIAPER Pole-to-Pole (HIPPO) aircraft campaign [*Wofsy et al*., 2011]. HIPPO aircraft CH_4 data are available on January 9, 2009, October 31, 2009, March 16, 2010, June 7 2011, and August 9, 2011. HIPPO aircraft CH_4 data cover from surface to 15 km and are available from 80ºN-70ºS [*Wofsy et al*., 2011].

5.2.3 NCEP2 Reanalysis Data

To explore the influence of circulation on the mid-tropospheric CH_4 distributions, 400 hPa meridional wind and vertical wind data from National Centers for Environmental Prediction 2 (NCEP2) Reanalysis [*Kistler et al*., 2001] are used in this chapter. The spatial resolution of NCEP2 meridional wind and vertical wind is $2.5^\circ \times 2.5^\circ$ (latitude by longitude). Data are available from January 1979 to present. Monthly mean data are available at http://www.esrl.noaa.gov/psd/data/gridded/data.ncep.reanalysis2.html.

5.3 Results

In order to explore the possible relationship between ENSO and CH_4, AIRS mid-tropospheric CH_4 data was separated to two groups (El Niño months and La Niña months). When SOI index is below (above) the mean value by one standard deviation of the SOI, it is classified as El Niño (La Niña) events. Following this definition, there are 18 El Niño months and 23 La Niña months from September 2002 to December 2014. The linear trend and annual cycle was removed from the AIRS mid-tropospheric CH_4 data AIRS detrended and deseasonalized CH_4 data were averaged over the El Niño and La Niña months, respectively. Results are shown in Figures 5.1a and 5.1b. During El Niño, there are positive sea surface temperature anomalies over the central Pacific As a result, there is rising air over the central Pacific [*Gage et al*., 1987]. Rising air over the central Pacific can bring low surface concentrations of CH_4 to the middle troposphere. Figure 5.1a demonstrates low concentrations of mid-tropospheric CH_4 over the central Pacific, which is related to the rising air over this region. Conversely, the sea surface temperature demonstrates positive anomalies in the western Pacific and there are anomalously rising motion over the western Pacific during La Niña months. Figure 5.1b shows that mid-tropospheric CH_4 concentrations are relatively low over the western Pacific during La Niña months. Low mid-tropospheric CH_4 is associated with the anomalously rising motion over this region, which can bring low concentrations of CH_4 from the surface to upper altitudes during La Niña months.

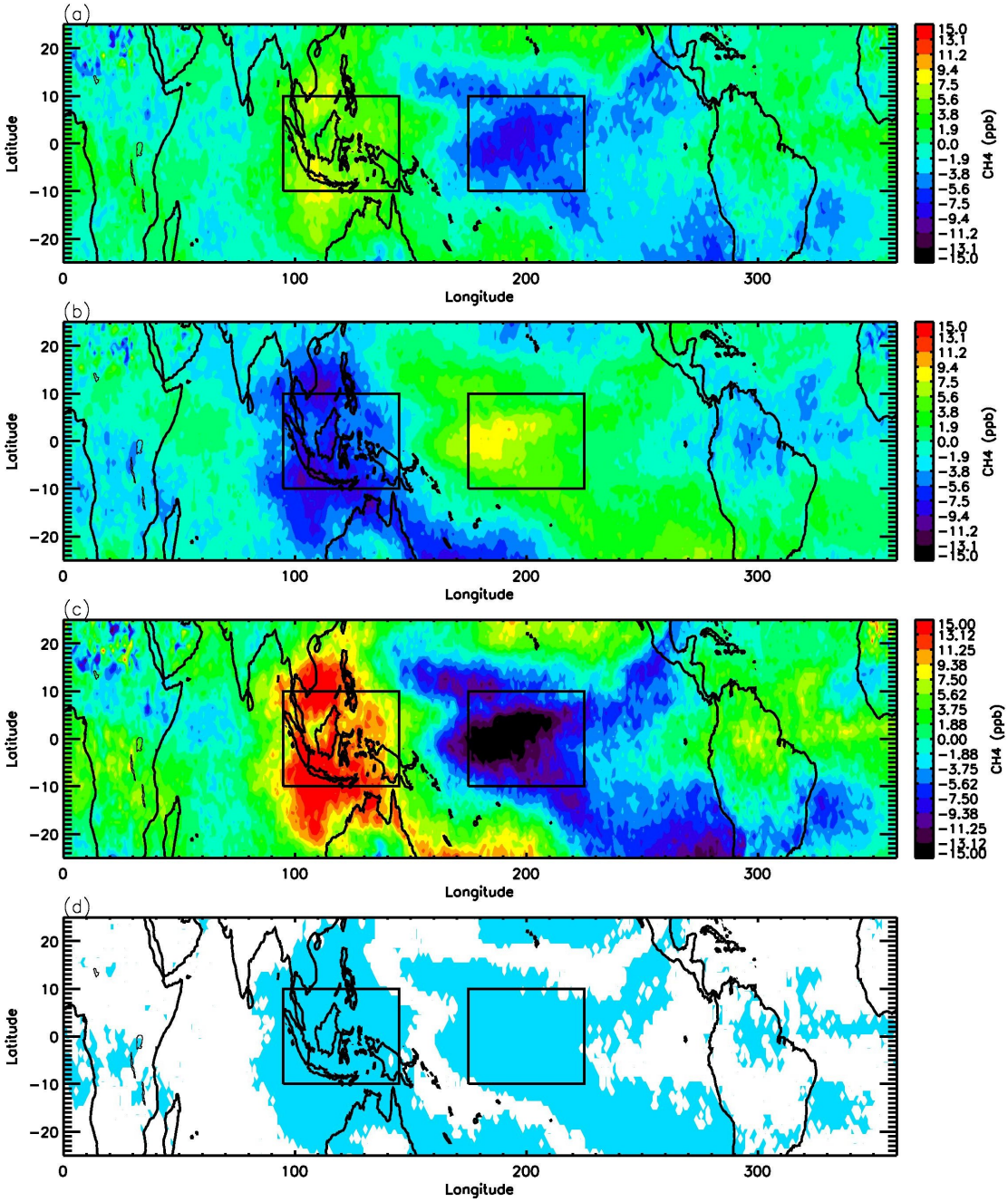

Figure 5.1: (a) AIRS detrended and deseasonalized mid-tropospheric CH_4 averaged for 18 El Niño months, (b) AIRS detrended and deseasonalized mid-tropospheric CH_4 averaged for 23 La Niña months, (c) AIRS mid-tropospheric CH_4 difference between El Niño and La Niña events, (d) CH_4 differences within 10% significance level are highlighted in blue. Data visualizations are produced using IDL version 8.3 (Exelis Visual Information Solutions, Boulder, Colorado; http://www.harrisgeospatial.com/).

Difference of AIRS CH_4 concentrations between El Niño and La Niña months is shown in Figure 5.1c. The difference is about -15 ppb (15 ppb) over the central (western) Pacific. Figure 5.1d show the statistical significance of the CH_4 difference between the two groups (El Niño/La Niña). Student-t test is utilized in estimating the significance [*Jiang et al*. 2010]. When CH_4 difference is within 10% significance level, it is highlighted as blue color in Figure 5.1d. Blue areas in Figure 5.1d mean the differences in Figure 5.1c are statistically significant.

The probability density functions of CH_4 difference between AIRS mid-tropospheric retrievals and convolved HIPPO aircraft CH_4 was estimated using the 941 HIPPO aircraft profiles. HIPPO aircraft CH_4 profiles were convolved with AIRS averaging kernels. The difference of CH_4 between AIRS mid-tropospheric retrievals and convolved aircraft CH_4 were used to generate the probability density function. The differences of AIRS mid-tropospheric CH_4 and aircraft convolved CH_4 are plotted as the black solid line, and the Gaussian probability density function is plotted as the red dashed line in Figure 5.2. As shown in Figure 5.2, the differences of AIRS mid-tropospheric CH_4 and aircraft convolved CH_4 follow a Gaussian distribution, which suggests that the errors in AIRS mid-tropospheric CH_4 are random errors. (Random errors are defined as errors moving in positive and negative directions and have a tendency to cancel each other.) When the number of observations increases, the errors will decrease. There are 3000-4000 CH_4 retrievals in each grid box for each group. The error for the mean CH_4 due to the random error is about 0.5 ppb, which is equal to the standard error (~25 ppb) divided by the square root of number of data

points [*Jiang et al*. 2015]. It is smaller than 15 ppb difference as shown in Figure 5.1c.

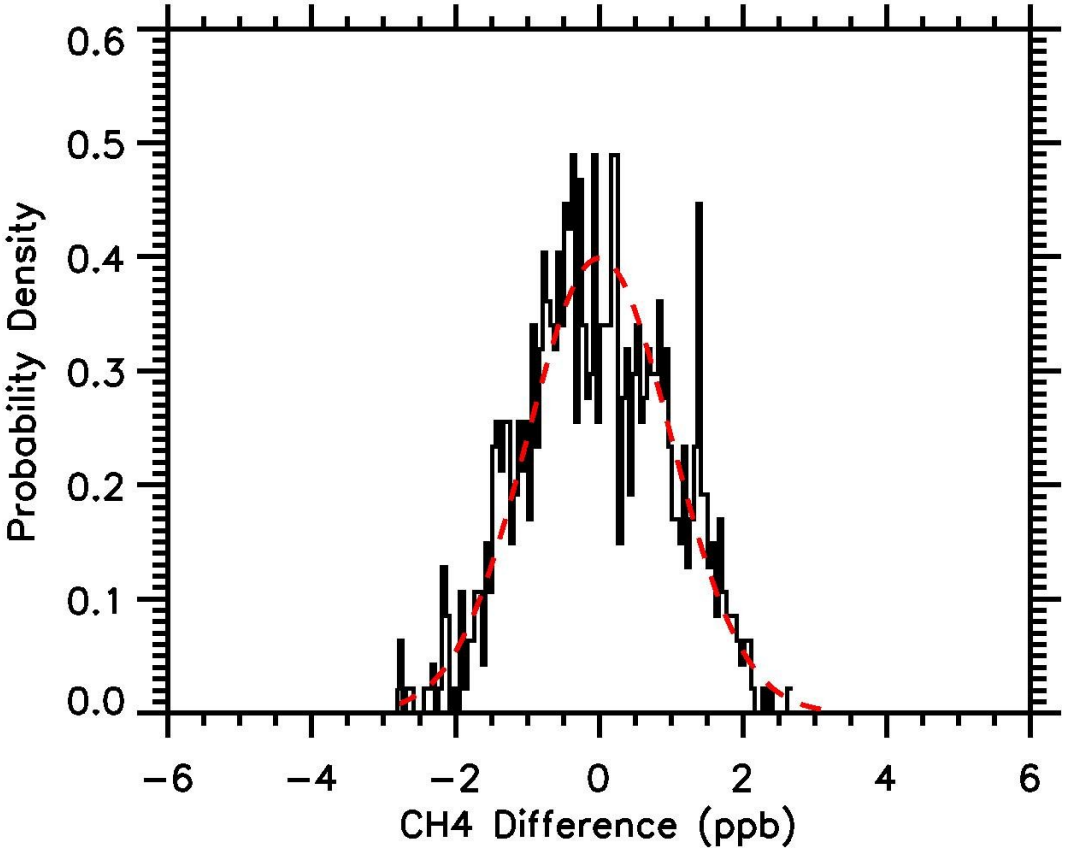

Figure 5.2: Probability density function of CH_4 difference between AIRS retrievals and aircraft convolved CH_4 (black solid line). 941 convolved aircraft data are used in this analysis. Gaussian probability density is plotted as the red dashed line.

In addition to exploring the spatial patterns of CH_4 at El Niño/La Niña months, an investigation into whether the ENSO can influence the temporal variations of CH_4 in the middle troposphere was carried out. Detrended difference of mid-tropospheric CH_4 between two regions (the central Pacific (175°E-225°E; 10°S-10°N) and the western Pacific (95°E-145°E, 10°S-10°N)) is calculated and shown in Figure 5.3a. Figure 5.3a also displays the detrended SOI (red dashed line). Figure

5.3a shows the CH_4 difference between the two regions is negative for El Niño events and positive for La Niña events, which is consistent with the spatial pattern results in Figure 5.1.

Using a Monte Carlo method [*Press et al*., 1992; *Devore et al*., 1982; *Jiang et al*., 2004], the correlation coefficient between the two-time series and the corresponding significance level in Figure 5.3a (i.e., CH_4 difference and SOI) was calculated. Correlations of 3,000 isospectral surrogate time series with the relevant indices are estimated. A distribution of correlations is generated and transformed into an approximately normal distribution by the Fisher transformation [*Devore et al*., 1982]. The significance level of the actual correlation within the normal distribution was then determined. Our analyses suggest that the correlation coefficient between the two time series (i.e., CH_4 difference and SOI) is 0.74. The significance level for the correlation coefficient is 1%, which suggests that the two time series in Figure 5.3a are correlated significantly. The interannual variability of the series is further investigated by filtering out high-frequency oscillations. All high frequency oscillations with period smaller than fifteen months are removed using a lowpass filter [*Jiang et al*., 2012]. As shown in Figure 5.3b, the two lowpass filtered time series correlate well, with a correlation coefficient of 0.96 (significance level 1%), which implies a significant correlation for the interannual signals in the two time series (CH_4 differences and SOI).

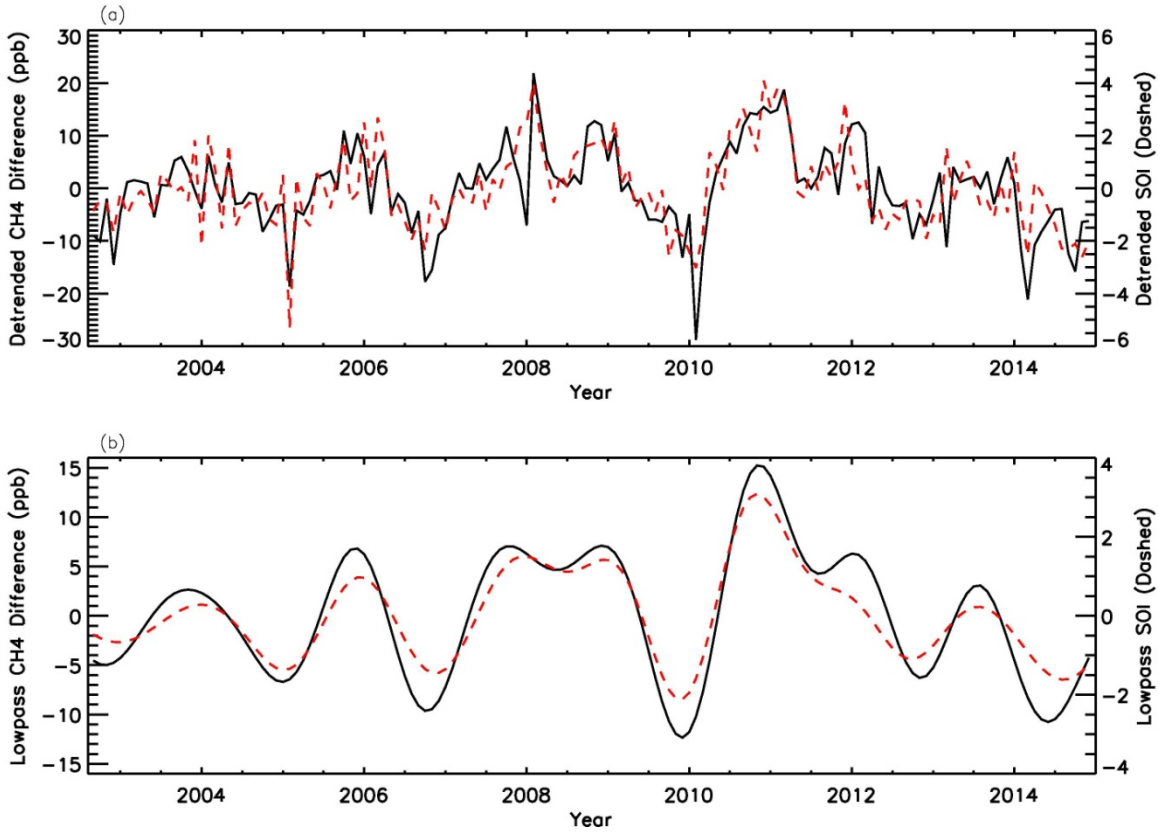

Figure 5.3: (a) Detrended AIRS mid-tropospheric CH_4 difference between central Pacific (175°E-225°E; 10°S-10°N) and western Pacific (95°E-145°E, 10°S-10°N) (black solid line) and detrended Southern Oscillation Index (red dashed line). Correlation coefficient between two time series is 0.74 (1% significance level). (b) Same as (a) but with a lowpass filter. Correlation coefficient between two lowpass filtered time series is 0.96 (1%).

In addition to the vertical transport, inter-hemispheric transport might also influence CH_4 concentrations. The NCEP2 400 hPa meridional winds were investigated during El Niño and La Niña months. Difference of meridional winds between El Niño and La Niña is shown in Figure 5.4a. Solid red contours refer to northward winds. Dashed red contours refer to southward winds. As shown in Figure 5.4a, there are more southward winds during El Niño than La Niña months over western Pacific Ocean, which can advect more CH_4 from the Northern Hemisphere to

the tropical region over the western Pacific Ocean during El Niño events. It can yield positive CH_4 anomalies over the western Pacific Ocean during El Niño events. Meridional wind differences between El Niño and La Niña are a little noisy over the central Pacific Ocean. The difference of vertical pressure velocity between El Niño and La Niña in Figure 5.4b was also assessed. Solid red contours refer to sinking air. Dashed red contours refer to rising air. There is more sinking air over the western Pacific Ocean and more rising air over the central Pacific Ocean during El Niño than La Niña, which can contribute to the CH_4 anomalies in Figure 5.1c.

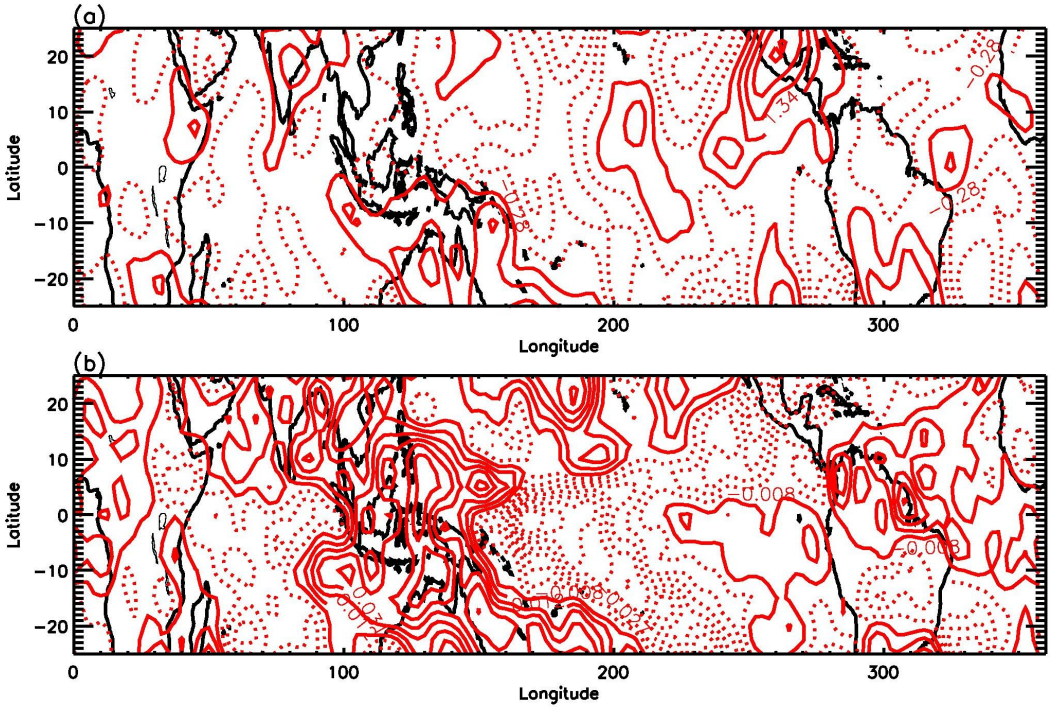

Figure 5.4: (a) NCEP2 400 hPa meridional wind difference between El Niño and La Niña events. Solid red contours refer to northward winds. Dashed red contours refer to southward winds. (b) NCEP2 400 hPa vertical pressure velocity difference between El Niño and La Niña events. Solid red contours refer to sinking air. Dashed red contours refer to rising air.

Some impacts to CH_4 anomaly in the mid-upper troposphere can be from surface emissions and the photochemical reaction. Major variants of surface emissions can result from surface temperature, biomass burning, and water level in rice paddies at Thailand, Indonesia and Malaysia, which can be modulated by El Niño/La Niña events. Even with some small change in the surface emission, their impact on CH_4 in the middle troposphere is still a secondary factor [*Xiong et al*., 2009]. During El Niño, there are more biomass burnings, which can influence OH concentrations [*Duncan et al*., 2003; *Levine et al*., 1996; *Van der Werf et al*., 2006; *Kaiser et al*., 2012]. The change of OH concentration in the atmosphere during El Niño/La Niña events can lead to the CH_4 destruction in the atmosphere, but it is hard to estimate such impact. This is because the OH concentration can either increase or decrease in different areas after including biomass burning in the model and there is not any evidence for this change of OH over the global scale during El Niño/La Niña [*Levine et al*., 1996]. The cross-correlation of monthly mean AIRS mid-tropospheric CH_4 difference and detrended Southern Oscillation Index was estimated in Figure 5.3a. The maximum correlation is 0.74 when the lag is 0 month. Vertical motion can bring air from the surface to mid-troposphere about one day [*Li et al*., 2010] and the lifetime of CH_4 with reacting with OH in the free troposphere is about 9-10 years [*Jacob*, 1999], which suggest that impact of large-scale circulation on mid-tropospheric CH_4 is more dominant than the contribution from OH. We will explore the impact of the surface emission on the mid-upper tropospheric CH_4 when we have good CH_4 surface emission data over the ocean in the future.

This analysis reveals the influence of large-scale circulation on atmospheric CH_4 over the tropical ocean during El Niño and La Niña. To better understand the vertical structure of CH_4, an analysis of CH_4 aircraft profiles from the HIPPO aircraft campaign over the tropical ocean. Vertical profiles for HIPPO aircraft CH_4 over the Pacific Ocean are shown as grey lines in Figure 5.5. Mean value and standard deviation of all HIPPO aircraft CH_4 over the Pacific Ocean are estimated and shown as red lines in Figure 5.5. As shown in Figure 5.5, CH_4 concentrations are lower near the surface than in the mid-troposphere, as there is no CH_4 surface emission source over the ocean. The HIPPO aircraft CH_4 data was separated into Northern Hemisphere and Southern Hemisphere over the Pacific Ocean, and found mean CH_4 concentrations are lower near the surface than the mid-troposphere for both regions. These results are consistent with previous CH_4 vertical profile results from IASI and HIPPO over Pacific Ocean as suggested by Xiong et al. [2013]. The relatively low CH_4 concentrations at the surface than the mid-troposphere coupled with changes in the circulation during El Niño/La Niña events lead to mid-tropospheric CH_4 anomalies as shown in Figure 5.1c.

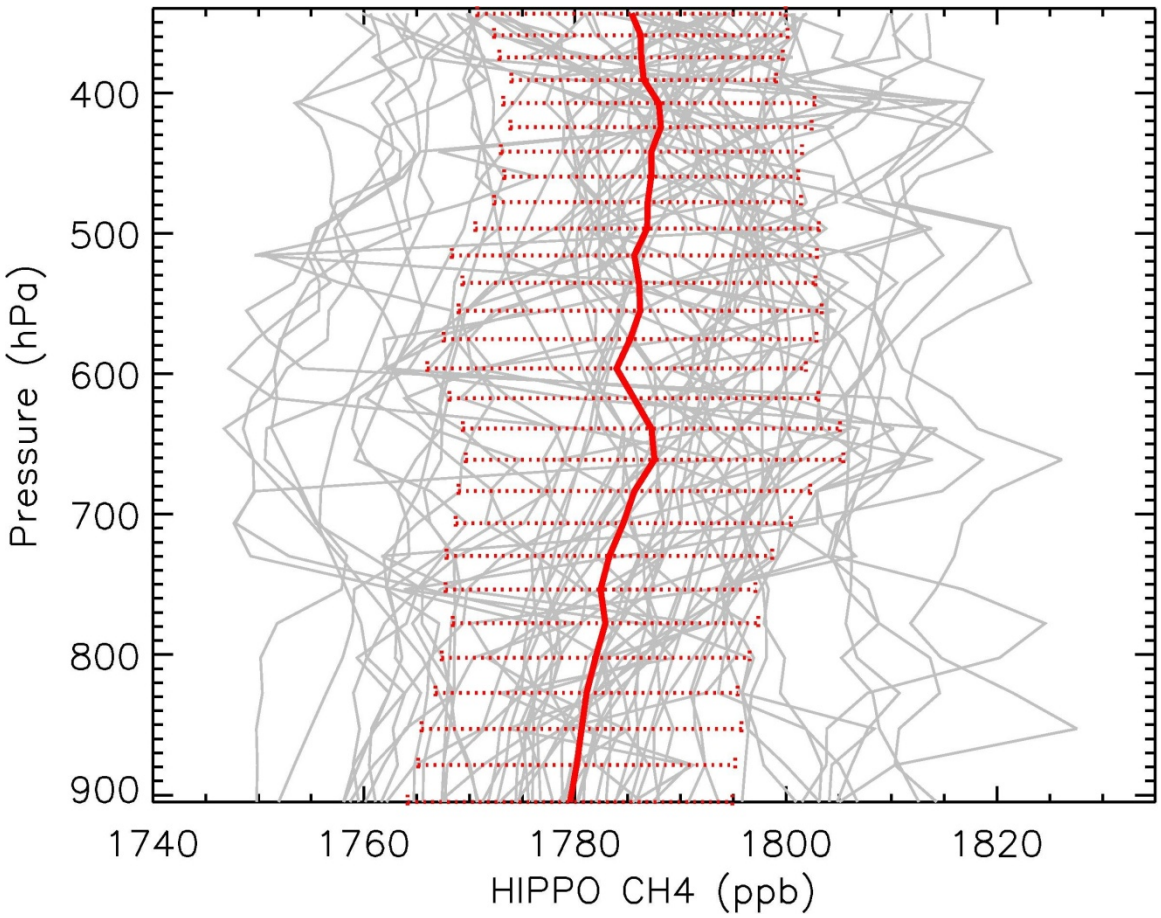

Figure 5.5: HIPPO CH_4 aircraft vertical profiles over Pacific Ocean (Grey lines). Red line is the mean value for all aircraft profiles. Error bars are standard deviations of CH_4 at different altitudes.

5.4 Conclusions

Using AIRS Version 6 data, mid-tropospheric methane concentrations were explored at the tropical Pacific region and this research investigated the influence of El Niño/La Niña on CH_4 for the first time. Enhanced rising air at the central Pacific in El Niño months can bring low surface concentrations of CH_4 over the ocean to the middle troposphere, so there is less CH_4 over the central Pacific than the western

Pacific. Rising air can bring low surface concentrations of CH_4 to the middle troposphere over the western Pacific in La Niña months, so there is less CH_4 over western Pacific than the central Pacific. In addition to the vertical transport, inter-hemispheric transport can also modulate CH_4 concentrations. The differences of NCEP2 400 hPa meridional winds (El Niño - La Niña) reveal that there are stronger southward winds during El Niño months over the western Pacific Ocean than La Niña months. It can contribute to the high CH_4 concentrations over the western Pacific Ocean in El Niño.

In addition to the spatial pattern, an analysis of the temporal variation of mid-tropospheric CH_4 difference between two regions of Pacific Ocean (central Pacific and western Pacific) was also executed in this chapter. The analysis reveals that the CH_4 difference between the two regions has a significant correlation to the SOI index. Results obtained from this study suggest that mid-tropospheric CH_4 concentrations can be modulated by ENSO. When we have good CH_4 surface emission data over the ocean in the future, we will explore the impact of the surface emission on the mid-upper tropospheric CH_4.

Due to its potency, methane is critical to understand climate change and global warming. In this chapter, the conclusion that mid-tropospheric CH_4 concentrations can be modulated by ENSO was demonstrated for the first time. The investigations of the spatiotemporal variations of methane will help better resolve the heating/cooling rates related to methane, and its roles in adjusting the global temperature. The anomalously vertical winds and southward winds can redistribute

methane over the tropics during El Niño events. Meanwhile, the observed variations of mid-tropospheric methane can help us identify possible deficiencies in the general circulation models and help modelers to better constrain/modify the large-scale vertical motion as a passive tracer. The correlation between methane anomaly and ENSO also provides one more way to monitor the ENSO events from satellite observations. Finally, the spatiotemporal characteristics of methane are helpful for better simulating the influence of ENSO on tracers, because such observational characteristics provide constraints on numerical simulations.

5.5 Acknowledgements

This project is supported by NASA grant NNX13AK34G and NASA ROSES Cassini Data Analysis Program. AIRS Version 6 CH_4 data are available at http://disc.sci.gsfc.nasa.gov/AIRS/data-holdings. NCEP2 Reanalysis data are available at http://www.esrl.noaa.gov/psd/data/gridded/data.ncep.reanalysis2.html.

Chapter 6: Conclusions

This work utilized *in situ* measurements and satellite-retrieved measurements of greenhouse gases to analyze atmospheric concentrations, movement, and sequestration.

First, revolutionary satellite-retrieved CO_2 data from the OCO-2 and GOSAT satellite missions were validated by comparing with TCCON *in situ* measurements. This crucial first step is prerequisite to the understanding of quality of the data, so it can be used appropriately in the future. It was found, when comparing CO_2 remotely retrieved from satellite to TCCON column CO_2, that satellite column CO_2 data matched well to the TCCON column CO_2 at all stations. Both data sources captured CO_2 annual cycles and positive trends. There is a larger CO_2 annual cycle amplitude in the Northern Hemisphere than the Southern Hemisphere. These results achieved in Chapter 2 are important for investigating CO_2 variability in future studies and research.

Second, the CO_2 annual cycle was studied to understand the variability of CO_2 in the atmosphere. Positive CO_2 trends were seen in the GOSAT column CO_2 data with amplitudes between 1.8 to 2.5 ppm/year. CO_2 trends are larger over the land than the ocean, because there are more CO_2 surface emissions over the land than the ocean. It was found that GOSAT column CO_2 annual cycle amplitudes are slightly higher than those from OCO-2 column CO_2. Additionally, latitude effects on CO_2 annual cycle amplitudes were explored. Annual cycle amplitudes are coherent among OCO-2 column CO_2, GOSAT column CO_2, and TCCON column CO_2; however, the

magnitude of column CO_2 annual cycle is smaller than those in the NOAA-ESRL surface CO_2 data. AIRS mid-tropospheric CO_2 annual cycle amplitudes are smallest in the Northern Hemisphere. However, in the Southern Hemisphere, the amplitudes for the CO_2 annual cycle from OCO-2, GOSAT, TCCON, AIRS, TES, and NOAA-ESRL CO_2 are small and comparable to each other. The CO_2 annual cycle amplitudes are larger in the Northern Hemisphere than that in the Southern Hemisphere. Results obtained from this research aid in an era of confident satellite retrievals and comprehensive understanding of vertical profiles of the CO_2 annual cycle. Understanding the CO_2 annual cycle allows scientists to better understand the biosphere-atmosphere interaction.

Third, the connection between solar-induced fluorescence (SIF) and atmospheric CO_2 was explored and found an inverse correlation. Chapter 4's groundbreaking conclusion allows for a better understanding of the carbon cycle and offers a new quantitative understanding of the biosphere carbon interaction. Photosynthesis happens when CO_2 is taken up by plants and leads to a high SIF value. As the biosphere takes up CO_2, the atmospheric CO_2 concentrations decrease. An anti-correlation can be seen between SIF and atmospheric CO2 concentrations retrieved from OCO-2. Finally, during Northern Hemisphere summer months of June, July, and August, SIF is high. Additionally, SIF has a positive correlation with (Precipitation – Evaporation), meaning when there is high available water for plants there is more SIF.

Finally, how mid-tropospheric methane is affected by El Niño-Southern Oscillation in the tropical Pacific region was studied by using AIRS Version 6 data for the first time. Heightened rising air at the central Pacific in El Niño months can bring low surface concentrations of CH_4 over the ocean to the middle troposphere, leading to less CH_4 over the central Pacific than the western Pacific. Rising air can bring low surface concentrations of CH_4 to the middle troposphere over the western Pacific in La Niña months, so there is less CH_4 over western Pacific than the central Pacific. In addition to the vertical transport, inter-hemispheric transport may regulate CH_4 concentrations. The differences of NCEP2 400 hPa meridional winds (El Niño - La Niña) reveal that there are stronger southward winds during El Niño months over the western Pacific Ocean than La Niña months. It can contribute to the high CH_4 concentrations over the western Pacific Ocean in El Niño. Outcomes gained in Chapter 5 suggest that mid-tropospheric CH_4 concentrations can be modulated by ENSO. This is the first time it was found that midtropospheric CH_4 concentration can be modulated by ENSO.

With increasing concentrations of greenhouse gasses like carbon dioxide and methane, understanding the atmospheric concentration, modulation, and sequestration of these gases has increased importance more now than ever before. In order to move forward in an era of positive interaction with the climate and mitigation of anthropogenic sources, we must first understand and quantify the emissions. This research leads to a greater understanding of CO_2 and CH_4 concentrations, modulations, and variability.

References

A. Kuze, H. Suto, M. Nakajima, T. HamazakiThermal and near infrared sensor for carbon observation Fourier-transform spectrometer on the Greenhouse Gases Observing Satellite for greenhouse gases monitoring. Applied Optics, 48 (2009), pp. 6716-6733

Allan, R., Lindesay, J. and Parker, D. (1996). El Niño-Southern Oscillation and Climatic Variability. CSIRO Publishing, Victoria, 416pp.

Allan, W. et al. Interannual variation of 13C in tropospheric methane: Implications for a possible atomic chlorine sink in the marine boundary layer. J. Geophys. Res. 110, D11306 (2005).

Anderson-Cook, C.M. A second order model for cylindrical data. J. Stat. Comput. Simul. 2000, 66, 51–65.

Artuso, F.; Chamard, P.; Piacentino, S.; Sferlazzo, D.M.; De Silvestri, L.; di Sarra, A.; Meloni, D.; Monteleone, F. Influence of transport and trends in atmospheric CO2 at Lampedusa. Atmos. Environ. 2009, 43, 3044–3051, doi:10.1016/j.atmosenv.2009.03.027.

Asaf, D., et al. (2013). Ecosystem photosynthesis inferred from measurements of carbonyl sulphide flux, Nature Geoscience, 6, 186-190.

Aumann, H. H. et al. AIRS/AMSU/HSB on the Aqua mission: Design, science objectives, data products, and processing systems. IEEE Trans. Geosci. Remote Sens. 41, 253–264 (2003).

Aumann, H. H., et al. (2003), AIRS/AMSU/HSB on the Aqua mission: Design, science objectives, data products, and processing systems, IEEE Trans. Geosci. Remote Sens., 41, 253–264

Avis, C., and ACOS Science Data Operations System (2010), README Document for ACOS Level 2 Standard Product.

Bacastow, R. (1976), Modulation of atmospheric carbon dioxide by the Southern Oscillation, Nature, 261, 116-118.

Bacastow, R. B., C. D. Keeling, and T. P. Whorf (1985), Seasonal amplitude increase in atmospheric CO2 concentration at Mauna Loa, Hawaii, Bacastow, R. B., C. D. Keeling, and T. P. Whorf (1985), Seasonal amplitude increase in atmospheric CO2 concentration at Mauna Loa, Hawaii, 1959–1982, J. Geophys. Res., 90, 10,529–10,540, doi:10.1029/JD090iD06p10529.

Baker, D.F.; Doney, S.C.; Schimel, D.S. Variational data assimilation for atmospheric CO2. Tellus Ser. B 2006, 8, 359–365

Baker, D.F.; Boesch, H.; Doney, S.C.; O'Brien, D.; Schimel, D.S. Carbon source/sink information provided by column CO2 measurements from the Orbiting Carbon Observatory. Atmos. Chem. Phys. 2010, 10, 4145–4165.

Baker, N. R. 2008. "Chlorophyll Fluorescence: A Probe of Photosynthesis in Vivo." The Annual Review of Plant Biology59: 89–113. doi:10.1146/annurev.arplant.59.032607.092759.

Beer, R. (2006), TES on the Aura mission: Scientific objectives, measurements, and analysis overview, IEEE T. Geosci. Remote, 44, 1102–1105

Blake, D. & Rowland F. Continuing worldwide increase in tropospheric methane, 1978 to 1987. Science 239, 1129–1131 (1988).

Bloom, S., et al. (2005), The Goddard Earth Observation System Data Assimilation System, GEOS DAS Version 4.0.3: Documentation and Validation, NASA TM-2005-104606, 26, 166pp.

Boesch, H., et al. (2006), Space-based near-infrared CO2 measurements: Testing the Orbiting Carbon Observatory retrieval algorithm and validation concept using SCIAMACHY observations over Park Falls, Wisconsin, J. Geophys. Res., 111, doi:10.1029/2006JD007080.

Boesch, H., et al. (2011), Global characterization of CO2 column retrievals from shortwave-infrared satellite observations of the Orbiting Carbon Observatory-2 Mission, Remote Sensing, 3, 270-304.

Born, M., Dorr, H. & Levin, I. Methane consumption in aerated soils of the temperate zone. Tellus 42, 2–8 (1990).

Bouma, M.J. and Dye, C. (1997). Cycles of malaria associated with El Niño in Venezuela. Journal of the American Medical Association 278: 1772–1774.

Bousquet, P. et al. Source attribution of the changes in atmospheric methane for 2006-2008. Atmos. Chem. Phys. 11, 3689-3700 (2011).

Bowman, K. W., et al. (2006), Tropospheric emission spectrometer: Retrieval method and error analysis, IEEE T. Geosci. Remote, 44, 1297–1307

Buermann, W., B. Lintner, C. Koven, A. Angert, J. E. Pinzon, C. J. Tucker, and I. Fung (2007), The changing carbon cycle at the Mauna Loa Observatory, Proc. Nat. Acad. Sci., 104, 4249-4254.

Buermann, W., B. Lintner, C. Koven, A. Angert, J. E. Pinzon, C. J. Tucker, and I. Fung (2007), The changing carbon cycle at the Mauna Loa Observatory, Proc. Natl. Acad. Sci., 104, 4249–4254.

Butler, T. M. et al. Simultaneous mass balance inverse modeling of methane and carbon monoxide. J. Geophys. Res. 110, D21310 (2005).

Campbell, J. E., et al. (2008), Photosynthetic control of atmospheric carbonyl sulfide during the growing season, Science, 322, 1085-1088.

Callaghan, J. and Power, S.B. (2012). Variability and decline in the number of severe tropical cyclones making land-fall over eastern Australia since the late nineteenth century. Climate Dynamics 37: 647-662. DOI: 10.1007/s00382-010-0883-2.

Chahine, M. T. et al. Satellite Remote Sounding of mid-tropospheric CO2. Geophys. Res. Lett. 35, doi:10.1029/2008GL035022 (2008).

Chahine, M., L. Chen, P. Dimotakis, X. Jiang, Q. Li, E. T. Olsen, T. Pagano, J. Randerson, and Y. L. Yung (2008), Satellite remote sounding of mid-tropospheric CO2, Geophys. Res. Lett., 35, L17807, doi:10.1029/2008GL035022.

Chahine, M.T., et al. (2005), On the determination of atmospheric minor gases by the method of vanishing partial derivatives with application to CO2, Geophys. Res. Lett., 32, L22803, doi:10.1029/2005GL024165.

Chahine, M.T., et al. (2008), Satellite Remote Sounding of Mid-Tropospheric CO2, Geophys. Res. Lett., 35, L17807, doi:10.1029/2008GL035022.

Chevallier,F.;Fisher,M.;Peylin,P.;Bousquet,S.S.;Breon,F.M.;Chedin,A.;Ciais,P.Inferring CO2 sources and sinks from satellite observations: Method and application to TOVS data. J. Geophys. Res. 2005, 110, D24309, doi:10.1029/2005JD006390.

Chevallier, F.; Engelen, R.J.; Peylin, P. The contribution of AIRS data to the estimation of CO2 sources and sinks. J. Geophys. Res. 2005, 32, L23801, doi:10.1029/2005GL024229.

Chevallier, F.; Breon, F.M.; Rayner, P.J. Contribution of the Orbiting Carbon Observatory to the estimation of CO2 sources and sinks: Theoretical study in a variational data assimilation framework. J. Geophys. Res. 2007, 112, D09307, doi:10.1029/2006JD007375.

Clerbaux, C. et al. Trace gas measurements from infrared satellite for chemistry and climate applications. Atmos. Chem. Phys. 3, 1495–1508 (2003).

Cleveland, M. S., A. E. Freeny, and T. E. Graedel (1983), The seasonal component of atmospheric CO2: Information from new approaches to the decomposition of seasonal time series, J. Geophys. Res., 88, 10,934–10,946, doi:10.1029/JC088iC15p10934.

Cleveland, M. S., A. E. Freeny, and T. E. Graedel (1983), The seasonal component of atmospheric CO2: Information from new approaches to the decomposition of seasonal time series, J. Geophys. Res., 88, 10934-10946.

Cleveland, W.S. Robust locally weighted regression and smoothing scatterplots. J. Am. Stat. Assoc. 1979, 74, 829–836, doi:10.1080/01621459.1979.10481038

Connor, B. J., H. Boesch, G. Toon, B. Sen, C. Miller, and D. Crisp (2008), Orbiting Carbon Observatory: Inverse method and prospective error analysis, J. Geophys. Res., 113, doi:10.1029/2006JD08336.

Crevoisier, C. et al. The 2007-2011 evolution of tropical methane in the mid-troposphere as seen from space by MetOp-A/IASI. Atmos. Chem. Phys. 13, 4279-4289 (2013).

Crevoisier, C. et al. Tropospheric methane in the tropics – first year from IASI hyperspectral infrared observations. Atmos. Chem. Phys. 9, 6337-6350 (2009).

Crisp, D., B. M. Fisher, C. O'Dell, C. Frankenberg, R. Basilio, H. Bosch, L. R. Brown, R. Castano, B. Connor, N. M. Deutscher, A. Eldering, D. Griffith, M. Gunson, A. Kuze, L. Mandrake, J. McDuffie, J. Messerschmidt, C. E. Miller, I. Morino, V. Natraj, J. Notholt, D. O'Brien, F. Oyafuso, I. Polonsky, J. Robinson, R. Salawitch, V. Sherlock, M. Smyth, H. Suto, T. Taylor, D. R. Thompson, P. O. Wennberg, D. Wunch, and Y. L. Yung, (2012), The ACOS X_{CO2} retrieval algorithm, Part 2: Global X_{CO2} data characterization, Atmos. Meas. Tech., 5, 687-707.

Crisp, D., R. M. Atlas, F. M. Breon, L. R. Brown, J. P. Burrows, P. Ciais, B. J. Connor, S. C. Doney, I. Y. Fung, D. J. Jacob, C. E. Miller, D. O'Brien, S. Pawson, J. T. Randerson, P. Rayner, R. J. Salawitch, S. P. Sander, B. Sen, G. L. Stephens, P. P. Tans, G. C. Toon, P. O. Wennberg, S. C. Wofsy, Y. L. Yung, Z. Kuang, B. Chudasama, G. Sprague, B. Weiss, R. Pollock, D. Kenyon, and S. Schroll (2004), The orbiting carbon observatory (OCO) mission, Adv. in Space Res., 34, 700-709.

Dargaville, R. J., R. M. Law, and F. Pribac (2000), Implications of interannual variability in atmospheric circulation on modeled CO2 concentrations and source estimates, Glob. Biogeochem. Cyc., 14, 931–943.

Dettinger, M. D., and M. Ghil (1998), Seasonal and interannual variations of atmospheric CO2 and climate, Tellus, ser. B, 50, 1–24.

Devore, J. L. Probability and statistics for Engineering and the Sciences, 1st ed. (Brooks/Cole, 1982).

Dickinson, R. E., and R. J. Cicerone (1986), Future global warming from atmospheric trace gases, Nature, 319, 109-115.

Dlugokencky, E. J. et al. Atmospheric methane at Mauna Loa and Barrow observatories: Presentation and analysis of in situ measurements. J. Geophys. Res. 100, 23103 – 23113 (1995).

Dlugokencky, E. J. et al. Atmospheric methane levels off: Temporary pause or a new steady-state. Geophys. Res. Lett. 30, doi:10.1029/2003GL018126 (2003).

Dlugokencky, E. J. et al. Conversion of NOAA CMDL atmospheric dry air CH4 mole fractions to a gravimetrically prepared standard scale. J. Geophys. Res. 110, D18306 (2005).

Dlugokencky, E. J. et al. The growth rate and distribution of atmospheric methane. J. Geophys. Res. 99, 17021-17043 (1994).

Duncan, B. N. et al. Interannual and seasonal variability of biomass burning emissions constrained by satellite observations. J. Geophys. Res. 108, doi:10.1029/2002JD002378 (2003).

Enting, I. G. (1987), The interannual variation in the seasonal cycle of carbon dioxide concentration at Mauna Loa, J. Geophys. Res., 92, 5497– 5504, 1987.

Feely, R. A., R. H. Gammon, B. A. Taft, P. E. Pullen, L. S. Waterman, T. J. Conway, J. F. Gendron, and D. P. Wisegarver (1987), Distribution of chemical tracers in the eastern equatorial Pacific during and after the 1982/1983 ENSO event, J. Geophys. Res., 92, 6545–6558.

Feng, L.; Palmer, P.I.; Boesch, H.; Dance, S. Estimating surface CO2 fluxes from space-borne CO2 dry air mole fraction observations using an ensemble Kalman Filter. Atmos. Chem. Phys. 2009, 9, 2619–2633.

Fernández-Duque, B.; Pérez, I.A.; Sánchez, M.L.; García, M.Á.; Pardo, N. Temporal patterns of CO2 and CH4 in a rural area in northern Spain described by a harmonic equation over 2010–2016. Sci. Total. Environ. 2017, 593, 1–9, doi:10.1016/j.scitotenv.2017.03.132.

Fernandez-Duque, Beatriz, et al. “Trend Assessment for a CO2 and CH4 Data Series in the North of Spain.” Proceedings of The 2nd International Electronic Conference on Atmospheric Sciences, vol. 1, no. 146, 2017, doi:10.3390/ecas2017-04147.

Fetzer, E. J. et al. Biases in total precipitable water vapor climatologies from Atmospheric Infrared Sounder and Advanced Microwave Scanning Radiometer. J. Geophys. Res. 111, doi:10.1029/2005JD006598 (2006).

Forster, P.; Ramaswamy, V.; Artaxo, P.; Berntsen, T.; Betts, R.; Fahey, D.W.; Haywood, J.; Lean, J.; Lowe, D.C.; Myhre, G.; Nganga, J.; Prinn, R.; Raga, G.; Schulz, M.; Van Dorland, R. Changes in atmospheric constituents and in radiative forcing. In Climate Change 2007: The Physical Science Basis. Contribution of Working Group I to the Fourth Assessment Report of the Intergovernmental Panel on Climate Change; Solomon, S., Qin, D., Manning, M., Chen, Z., Marquis, M., Averyt, K.B., Tignor, M., Miller, H.L., Eds.; Cambridge University Press: Cambridge, UK and New York, NY, USA, 2007.

Frankenberg, C. et al. Assessing methane emissions from global space-borne observations. Science 308, 1010–1014 (2005).

Frankenberg, C. et al. Satellite chartography of atmospheric methane from SCIAMACHY on board ENVISAT: Analysis of the years 2003 and 2004. J. Geophys. Res. 111, D07303 (2006).

Frankenberg, C., C. O'Dell, J. Berry, L. Guanter, J. Joiner, P. Kohler, R. Pollock, and T. E. Taylor. 2014. "Prospects for Chlorophyll Fluorescence Remote Sensing from the Orbiting Carbon Observatory-2." Remote Sensing of Environment147: 1–12. doi:10.1016/j.rse.2014.02.007.

Frankenberg, C., et al. (2011), New global observations of the terrestrial carbon cycle from GOSAT: Patterns of plant fluorescence with gross primary productivity, Geophys. Res. Lett., 38, L17706.

Frankenberg, C., et al. (2011), New global observations of the terrestrial carbon cycle from GOSAT: Patterns of plant fluorescence with gross primary productivity, Geophys. Res. Lett., 38, L17706.

Frankenberg, Christian, et al. "Prospects for Chlorophyll Fluorescence Remote Sensing from the Orbiting Carbon Observatory-2." Remote Sensing of Environment, vol. 147, 2014, pp. 1–12., doi:10.1016/j.rse.2014.02.007.

Gage, K. S. & Reid, G. C. Longitudinal variations in tropical tropopause properties in relation to tropical convection and El Niño–Southern Oscillation events. J. Geophys. Res. 92, 14197–14203 (1987).

Geophysical Research Letters, 40 (2013), pp. 2829-2833, 10.1002/grl.50452

Giglio, L., G. R. van der Werf, J. T. Randerson, G. J. Collatz, and P. S. Kasibhatla (2006), Global estimation of burned area using MODIS active fire observations, Atmos. Chem. Phys., 6, 957-974.

GLOBALVIEW-CO2 (2010), Cooperative atmospheric data integration project: Carbon dioxide [CD-ROM], NOAA ESRL Boulder Colorado. [Available on

Internet via anonymous FTP to ftp.cmdl.noaa.gov, Path: ccg/co2/GLOBALVIEW.]

GLOBALVIEW-CO2 (2010), Cooperative Atmospheric Data Integration Project: Carbon Dioxide [CD-ROM], NOAA ESRL, Boulder, Colorado (Also available on Internet via anonymous FTP to ftp.cmdl.noaa.gov, Path: ccg/co2/GLOBALVIEW).

Guanter, L., C. Frankenberg, A. Dudhia, P. E. Lewis, J. Gomez-Dans, A. Kuze, H. Suto, and R. G. Grainger. 2012. "Retrieval and Global Assessment of Terrestrial Chlorophyll Fluorescence from GOSAT Space Measurements."Remote Sensing of Environment 121: 236–251. doi:10.1016/j.rse.2012.02.006.

Guanter, L., L. Alonso, L. Gomez-Chova, J. Amoros-Lopez, J. Vila, and J. Moreno. 2007. "Estimation of Solar-Induced Vegetation Fluorescence from Space measurements." Geophysical Research Letters 34: L08401. doi:10.1029/2007GL029289.

Hammer, G., Mitchell, C. and Nicholls, N. (2000), Applications of Seasonal Climate Forecasts to Agricultural and Natural Systems, 469 pp., Kluwer Acad., Norwell, Mass.

Holbrook, N.J., Chan, P.S-L. and Venegas, S.A. (2005a). Oscillatory and propagating modes of temperature variability at the 3—3.5- and 4—4.5-yr time scales in the upper southwest Pacific Ocean. Journal of Climate 18: 719-736.

Holbrook, N.J. et al. (2012) El Niño-Southern Oscillation. In A Marine Climate Change Impacts and Adaptation Report Card for Australia 2012 (Eds. E.S. Poloczanska, A.J. Hobday and A.J. Richardson). <http://www.oceanclimatechange.org.au>. ISBN: 978-0-643-10928-5

Holmgren, M., Scheffer, M., Ezcurra, E., Gutierrez, J.R. and Mohren, G.M.J. (2001). El Niño effects on the dynamics of terrestrial ecosystems, Trends in Ecology and Evolution 16: 89–94.

Houweling, S.; Hartmann, W.; Aben, I.; Schrijver, H.; Skidmore, J.; Roelofs, G.J.; Breon, F.M. Evidence of systematic errors in SCIAMACHY-observed CO2 due to aerosols. Atmos. Chem. Phys. 2005, 5, 3003–3013.

J. Joiner, L. Guanter, R. Lindstrot, M. Voigt, A.P. Vasilkov, E.M. Middleton, et al. Global monitoring of terrestrial chlorophyll fluorescence from moderate spectral resolution near-infrared satellite measurements: methodology, simulations, and application to GOME-2 Atmospheric Measurement Techniques Discussions, 6 (2013), pp. 3883-3930, 10.5194/amtd-6-3883-2013

J. Joiner, Y. Yoshida, A.P. Vasilkov, E.M. Middleton, P.K.E. Campbell, Y.Yoshida, e t al.Filling-in of near-infrared solar lines by terrestrial fluorescence and other geophysical effects: Simulations and space-based observations from SCIAMACHY and GOSAT. Atmospheric Measurement Techniques, 5 (2012), pp. 809-829

J.E. Lee, C. Frankenberg, C. van der Tol, J.A. Berry, L. Guanter, C.K. Boyce, et al. Forest productivity and water stress in Amazonia: Observations from GOSAT

chlorophyll fluorescence Proceedings of the Royal Society B: Biological Sciences, 280 (2013), 10.1098/rspb.2013.0171

Jacob, D. J. Introduction to Atmospheric Chemistry. Princeton University Press (1999).

Jiang, X. et al. Influence of El Niño on mid-tropospheric CO2 from Atmospheric Infrared Sounder and model. J. Atmos. Sci., 223-230 (2013).

Jiang, X. et al. Interannual Variaiblity of mid-tropospheric CO2 from Atmospheric Infrared Sounder. Geophys. Res. Lett. 37, doi:10.1029/2010GL042823 (2010).

Jiang, X. et al. Modulation of mid-tropospheric CO2 by the South Atlantic Circulation. J. Atmos. Sci., doi:10.1175/JAS-D-14-0340.1 (2015).

Jiang, X. et al. Quasi-biennial oscillation and quasi-biennial oscillation-annual beat in the tropical total column ozone: A two-dimensional model simulation. J. Geophys. Res. 109, D16305 (2004).

Jiang, X., D. Crisp, E. T. Olsen, S. S. Kulawik, C. E. Miller, T. S. Pagano, M. Liang, and Y. L. Yung (2016), CO2 annual and semiannual cycles from multiple satellite retrievals and models, Earth and Space Science, 3, doi:10.1002/2014EA000045.

Jiang, X., E. T. Olsen, T. S. Pagano, H. Su, and Y. L. Yung (2015), Modulation of midtropospheric CO2 by the South Atlantic Walker Circulation, J. Atmos. Sci., 72, 2241–2247.

Jiang, X., et al. (2008a), Simulation of Upper Troposphere CO2 from two-dimensional and three-dimensional models, Global Biogeochemical Cycles, 22, doi:10.1029/2007GB003049.

Jiang, X., J. Wang, E. T. Olsen, M. Liang, T. S. Pagano, L. Chen, S. J. Licata, and Y. L. Yung (2013), Influence of El Nino on mid-tropospheric CO2 from Atmospheric Infrared Sounder and Model, J. Atmos. Sci., 70, 223-230.

Jiang, X., M. T. Chahine, E. T. Olsen, L. Chen, and Y. L. Yung (2010), Interannual variability of mid-tropospheric CO2 from atmospheric infrared sounder, Geophys. Res. Lett., 37, L13801, doi:10.1029/2010GL042823.

Jiang, X., M. T. Chahine, E. T. Olsen, L. L. Chen, and Y. L. Yung (2010), Interannual Variability of Mid-tropospheric CO2 from Atmospheric Infrared Sounder, Geophys. Res. Lett., 37, doi: 10.1029/2010GL042823.

Jiang, X., M. T. Chahine, Q. Li, M. Liang, E. T. Olsen, L. Chen, J. Wang, and Y. L. Yung (2012), CO2 semi-annual oscillation in the middle troposphere and at the surface, Global Biogeochem. Cycles, 26, GB3006, doi:10.1029/2011GB004118.

Jiang, X., Q. Li, M. T. Chahine, and Y. L. Yung (2012), CO2 semi-annual oscillation in the middle troposphere and at the surface, Global Biogeochem. Cycles, 26, doi:10.1029/2011GB004118.

Joiner, J., L. Guanter, R. Lindstrot, M. Voigt, A. P. Vasilkov, E. M. Middleton, K. F. Huemmrich, Y. Yoshida, and C.Frankenberg. 2013. “Global Monitoring of Terrestrial Chlorophyll Fluorescence from Moderate-Spectral-Resolution

Near-Infrared Satellite Measurements: Methodology, Simulations, and Application to GOME-2." Atmospheric Measurement Techniques 6: 2803–2823. doi:10.5194/amt-6-2803-2013.

Joiner, J., Y. Yoshida, A. P. Vasilkov, L. A. Corp, and E. M. Middleton. 2011. "First Observations of Global and Seasonal Terrestrial Chlorophyll Fluorescence from Space." Biogeosciences 8: 637–651. doi:10.5194/bg-8-637-2011.

Kahn, B. H. et al. The Atmospheric Infrared Sounder version 6 cloud products. Atmos. Chem. Phys. 14, 399-426 (2014).

Kahya, E. and Dracup, J.A. (1993). U.S. streamflow patterns in relation to the El Niño/Southern Oscillation, Water Resources Research 29: 2491–2504.

Kaiser, J. W. et al. Biomass burning emissions estimated with a global fire assimilation system based on observed fire radiative power. Biogeosciences 9, 527-554 (2012).

Keeling, C. D., and R. Revelle (1985), Effects of ENSO on the atmospheric content of CO2, Meteroritics, 20, 437–450.

Keeling, C. D., J. F. S. Chin, and T. P. Whorf (1996), Increased activity of Northern Hemispheric vegetation inferred from atmospheric CO2 measurements, Nature, 382, 146-149.

Keeling, C. D., J. F. S. Chin, and T. P. Whorf (1996), Increased activity of Northern Hemispheric vegetation inferred from atmospheric CO2 measurements, Nature, 382, 146–149.

Keeling, C. D., T. P. Whorf, M. Wahlen, and J. Vanderplicht (1995), Interannual extremes in the rate of rise of atmospheric carbon dioxide since

Keeling, C. D., T. P. Whorf, M. Wahlen, and J. Vanderplicht (1995), Interannual extremes in the rate of rise of atmospheric carbon dioxide since 1980, Nature, 375, 666-670.

Keenan, Trevor F., Gray, Josh, Friedl, Mark A., Toomey, Michael, Bohrer, Gil, Y. Hollinger, David, Munger, J. William, O'Keefe, John, Schmid, Hans Peter, Wing, Ian Sue, Yang, Bai, Richardson, Andrew D. (2014), Net carbon uptake has increased through warming-induced changes in temperate forest phenology, Nature Climate Change, 4, pages 598–604 (2014). doi:10.1038/nclimate2253

Keppel-Aleks, G., P. O. Wennberg, and T. Schneider (2011), Sources of variations in total column carbon dioxide, Atmos. Chem. Phys., 11, 3581-3593.

Kirschke, S. et al. Three decades of global methane sources and sinks. Nature Geoscience 6, 813-823 (2013).

Kuai, L., et al. (2015), Estimate of Carbonyl Sulfide tropical oceanic surface fluxes using Aura tropospheric emission spectrometer observations, J. Geophys. Res., 120, 11012-11023.

Kuang, Z. M., J. Margolis, G. Toon, D. Crisp, and Y. L. Yung (2002), Spaceborne Measurements of Atmospheric CO2 by High-resolution NIR Spectrometry of Reflected Sunlight: An Introductory Study, Geophys. Res. Lett., 29, 1716, doi:10.1029/2001GL014298.

Kulawik, S. S., et al. (2010), Characterization of Tropospheric Emission Spectrometer (TES) CO2 for carbon cycle science, Atmos. Chem. Phys., 10, 5601–5623.

Kulawik, S. S., et al. (2010), Characterization of Tropospheric Emission Spectrometer (TES) CO2 for carbon cycle science, Atmos. Chem. Phys., 10, 5601–5623.

Kuze, A., H. Suto, M. Nakajima, and T. Hamazaki (2009), Thermal and near infrared sensor for carbon observation Fourier- transform spectrometer on the Greenhouse Gases Observing Satellite for greenhouse gases monitoring, Appl. Opt., 48, 6716–6733.

Le Quere, C.; Raupach, M.R.; Canadell, J.G.; Marland, G.; et al. Trends in the sources and sinks of carbon dioxide. Nature Geoscience 2009, 2, 831–836.

Levine, J. Biomass Burning and Global Change: Remote Sensing, modeling, and inventory development, and biomass burning in Africa, Volume 1, (MIT Press, 1996).

Li, K. F. et al. Tropical mid-tropospheric CO2 variability driven by the Madden-Julian Oscillation. Proc. Nat. Acad. Sci. USA 107, 19171-19175 (2010).

Li, K. F., B. Tian, D. E. Waliser, and Y. L. Yung (2010), Tropical mid-tropospheric CO2 variability driven by the Madden-Julian Oscillation, Proc. Natl. Acad. Sci. U.S.A., 107, 19,171–19,175.

Li, K. F., B. Tian, D. E. Waliser, and Y. L. Yung (2010), Tropical mid-tropospheric CO-2 variability driven by the Madden-Julian Oscillation, Proc. Nat. Acad. Sci., 107, 19171-19175.

Macatangay, R., T. Warneke, C. Gerbig, S. Korner, R. Ahmadov, M. Heimann, and J. Notholt (2008), A framework for comparing remotely sensed and in situ CO2 concentrations, Atmos. Chem. Phys., 8, 2555–2568.

Matsueda, H.; Inoue, H.Y.; Ishii, M. Aircraft observation of carbon dioxide at 8–13 km altitude over the western Pacific from 1993 to 1999. Tellus Ser. B 2002, 54, 1–21.

McPhaden, M.J., Zebiak, S.E. and Glantz, M.H. (2006). ENSO as an integrating concept in Earth science. Science 314: 1740-1745.

Merendo, J.A. (1995). Variations and change in South American stream flow. Climate Change 31: 99–117.

Miller, C. E., D. Crisp, P. L. DeCola, S. C. Olsen, J. T. Randerson, A. M. Michalak, A. Alkhaled, P. Rayner, D. J. Jacob, P. Suntharalingam, D. B. A. Jones, A. S. Denning, M. E. Nicholis, S. C. Doney, S. Pawson, H. Boesch, B. J. Connor, I. Y. Fung, D. O'Brien, R. J. Salawitch, S. P. Sander, B. Sen, P. Tans, G. C. Toon, P. O. Wennberg, S. C. Wofsy, Y. L. Yung, and R. M. Law (2007), Precision requirements for space-based X-CO2 data, J. Geophys. Res., 112, doi:10.1029/2006JD007659.

Morgan, C. G., et al. (2004), Isotopic fractionation of nitrous oxide in the stratosphere: Comparison between model and observations, J. Geophys. Res., 109, D04305.

Myhre, G. et al. Anthropogenic and natural radiative forcing. In: IPCC Climate Change 2014: Impacts, Adaptation, and Vulnerability. Jacob, D.,

Ravishankara, A. R. & Shine, K. (eds.), Cambridge University Press, Cambridge, United Kingdom and New York, NY, USA (2014).

NOAA/PMEL/TAO Project Office, Dr. Michael J. McPhaden, Director; http://www.reefresilience.org/images/Stressors_ENSO3_small.png

N.C. Parazoo, K. Bowman, C. Frankenberg, J.E. Lee, J.B. Fisher, J. Worden, et al. Interpreting seasonal changes in the carbon balance of southern Amazonia using measurements of XCO2 and chlorophyll fluorescence from GOSAT Geophysical Research Letters, 40 (2013), pp. 2829-2833, 10.1002/grl.50452

N.C. Parazoo, K. Bowman, C. Frankenberg, J.E. Lee, J.B. Fisher, J.Worden, et al.Interpreting seasonal changes in the carbon balance of southern Amazonia using measurements of XCO2 and chlorophyll fluorescence from GOSAT

Nguyen, H., et al. (2014), A method for collocating satellite XCO2 data to ground-based data and its application to ACOS-GOSAT and TCCON, Atmos. Meas. Tech., 7, 2631–2644.

Nicholls, N. (1984). The southern oscillation, sea-surface temperature, and interannual fluctuations in Australian tropical cyclone activity. International Journal of Climatology 4: 661-670.

Nicholls, N. (1985). Impact of the southern oscillation on Australian crops. Journal of Climatology 5: 553–560. doi: 10.1002/joc.3370050508.

Nicholls, N. (1993). El Niño-Southern Oscillation and vector-borne disease. Lancet 342: 1284-1285.

Olsen, E. T. (2011), Reaching for the middle troposphere and lower troposphere for AIRS CO2 retrievals – progress toward the retrieval of a profile, AIRS Science Team Meeting, Pasadena, April 26-28.

Olsen, E. T., and S. J. Licata (2015), AIRS Version 5 release tropospheric CO2 products, Jet Propulsion Laboratory, 38 pp. [Available online at http://disc.sci.gsfc.nasa.gov/AIRS/documentation/v5_docs/AIRS_V5_Release_User_Docs/AIRS-V5-Tropospheric-CO2-Products.pdf].

Olsen, E. T., and S. J. Licata (2015), AIRS version 5 release tropospheric CO2 products, Jet Propulsion Laboratory, 38 pp. [Available online at http://disc.sci.gsfc.nasa.gov/AIRS/documentation/v5_docs/AIRS_V5_Release_User_Docs/AIRS-V5-Tropospheric-CO2-Products.pdf]

Olsen, E. T., M. T. Chahine, L. Chen, X. Jiang, T. S. Pagano, and Y. L. Yung (2008), Validation of AIRS retrievals of CO2 via comparison to in situ measurements, Abstract A32B-04 presented at 2008 AGU Fall Meeting, AGU, San Francisco, Calif., 15-19 Dec

Olsen, E. T., M. T. Chahine, L. Chen, X. Jiang, T. S. Pagano, and Y. L. Yung (2008), Validation of AIRS Retrievals of CO2 via comparison to in situ measurements, AGU 2008 Fall Meeting, San Francisco, December 15-19.

Olsen, S. C., and J. T. Randerson (2004), Differences between surface and column atmospheric CO2 and implications for carbon cycle research, J. Geophys. Res., 109, doi:10.1029/2003JD003968.

Pagano, T. S. et al. Pre-launch and in-flight radiometric calibration of the Atmospheric Infrared Sounder (AIRS). IEEE Trans. Geosci. Remote Sens. 41, 265–273 (2003).

Pagano, T. S., et al. (2014), Global variability of midtropospheric carbon dioxide as measured by the Atmospheric Infrared Sounder, J. Appl. Remote Sens., 8, doi:10.1117/1.JRS.8.084984.

Pan, Y., et al. (2011), A large and persistent carbon sink in the World's forests, Science, 333, 988-993.

Papageorgiou, G. C., and Govindjee, eds. 2004. "Chlorophyll a Fluorescence: A Signature of Photosynthesis." InAdvances in Photosynthesis and Respiration. Vol. 19. Dordrecht: Kluwer Academic Publishers. doi:10.1007/978-1-4020-3218-9.

Park, M. et al. Seasonal variation of methane, water vapor, and nitrogen oxides near the tropopause: Satellite observations and model simulations. J. Geophys. Res. 109, D03302 (2004).

Pearman, G. I., and P. Hyson (1980), Activities of the global biosphere as reflected in atmospheric CO2 records, J. Geophys. Res., 85, 4457–4467, doi:10.1029/JC085iC08p04457.

Pearman, G. I., and P. Hyson (1981), The annual variation of atmospheric CO2 concentration observed in the Northern Hemisphere, J. Geophys. Res., 86, 9839–9843, doi:10.1029/JC086iC10p09839.

Pérez, I.A.; Sánchez, M.L.; García, M.Á.; Pardo, N. Trend analysis of CO2 and CH4 recorded at a semi- natural site in the northern plateau of the Iberian Peninsula. Atmos. Environ. 2017, 151, 24–33, doi:10.1016/j.atmosenv.2016.11.068.

Philander, S.G.H. (1990). El Niño, La Niña, and the Southern Oscillation. International Geophysics Series, Vol. 46, Academic Press, 293 pp.

Phillips, J.G., Cane, M.A. and Rosenzweig, C. (1998). ENSO, seasonal rainfall patterns and simulated maize yield variability in Zimbabwe, Agricultural and Forest Meteorology 90: 39–50.

Pickers, P.A.; Manning, A.C. Investigating bias in the application of curve fitting programs to atmospheric time series. Atmos. Meas. Tech. 2015, 8, 1469–1489, doi:10.5194/amt-8-1469-2015.

Platt, U., Allan, W. & Lowe, D. C. Hemispheric average Cl atom concentration from 13C/12C ratios in atmospheric methane. Atmos. Chem. Phys. 4, 2393–2399 (2004).

Power, S., Casey, T., Folland, C., Colman, A. and Mehta, V. (1999a). Inter-decadal modulation of the impact of ENSO on Australia. Climate Dynamics 15: 234-319.

Power, S., Tseitkin, F., Mehta, V., Lavery, B., Torok, S. and Holbrook, N. (1999b). Decadal climate variability in Australia during the twentieth century. International Journal of Climatology 19: 169-184.

Power, S., Tseitkin, F., Torok, S., Lavery, B., Dahni, R. and McAvaney, B. (1998). Australian temperature, Australian rainfall and the Southern Oscillation, 1910-1992: coherent variability and recent changes. Australian Meteorological Magazine 47: 85-101.

Press, W. et al. Numerical Recipes in Fortran 77: The Art of Scientific Computing. 2nd ed. (Cambridge Univ. Press, 1992).

Prince, S. D., and S. N. Goward (1995), Global primary production: A remote sensing approach, J. Biogeography, 22, 815-835.

Prinn, R. G., et al. (2000), A history of chemically and radiatively important gases in air deduced from ALE/GAGE/AGAGE, J. Geophys. Res., 105, 17751-17792.

Public Release of Concentration Data (Carbon Dioxide and Methane) Analyzed from GOSAT Observational Data; NIES: Tsukuba, Japan, 2010; Available online: http://www.gosat.nies.go.jp/eng/result/result.htm.

Randerson, J. T., et al. (2013), Global fire emissions database, Version 3 (GFEDv3.1), Data set available on line (http://daac.ornl.gov/) from Oak Ridge National Laboratory Distributed Active Archive Center, Oak Ridge, USA, doi:10.3334/ORNLDAAC/1191.

Raychaudhuri 2014

Rayner, P.J.; O'Brien, D. The utility of remotely sensed CO2 concentration data in surface source inversions. Geophys. Res. Lett. 2001, 28, 175–178.

Razavi, A. et al. Characterization of methane retrievals from the IASI space-borne sounder. Atmos. Chem. Phys. 9, 7889-7899 (2009).

Richardson AD, Hollinger DY (2007) A method to estimate the additional uncertainty in gap-filled NEE resulting from long gaps in the CO2 flux record. Agricultural and Forest Meteorology, 147, 199–208, doi: 10.1016/j.agrformet.2007.06.004.

Ropelewski, C.F. and Halpert, M.S. (1987). Global and regional scale precipitation patterns associated with El Niño/Southern Oscillation. Monthly Weather Review 115: 1606-1626.

Ropelewski, C.F. and Halpert, M.S. (1989). Precipitation patterns associated with high index phase of Southern Oscillation. Journal Climate 2: 268-284. Running, S. W., et al. (2004), A continuous satellite-derived measure of global terrestrial primary production, BioScience, 54, 547-560.

Saitoh, N. et al. Comparisons between XCH4 from GOSAT shortwave and thermal infrared spectra and aircraft CH4 measurements over Guam, Sci. Online Lett. Atmos. 8, 145-149 (2012).

Sánchez, M.L.; Pérez, I.A.; García, M.A. Study of CO2 variability at different temporal scales recorded in a rural Spanish site. Agric. For. Meteorol. 2010, 150, 1168–1173, doi:10.1016/j.agrformet.2010.04.018.

Sandoval-Soto, L., M. Stanimirov, M. von Hobe, V. Schmitt, J. Valdes, A. Wild, and J. Kesselmeier (2005), Global uptake of carbonyl sulfide (COS) by terrestrial vegetation: Estimates corrected by deposition velocities normalized to the uptake of carbon dioxide (CO2), Biogeosciences, 2, 125-132.

Sarmiento, J. L., and S. Wofsy (1999), A U. S. Carbon Cycle Science Plan—A report of the Carbon and Climate Working Group, U. S. Global Change Research Program.

Sarmiento, J. L., and S. Wofsy (1999), A U. S. Carbon Cycle Science Plan. A report of the Carbon and Climate Working Group. U. S. Global Change Research Program.

Schoeberl, M. R. et al. An analysis of the Antarctic Halogen Occultation Experiment trace gas observations. J. Geophys. Res. 100, 5159–5172 (1995).

Schuck, T. J. et al. Distribution of methane in the tropical upper troposphere measured by CARIBIC and CONTRAIL aircraft. J. Geophys. Res. 117, D19304 (2012).

Shiomi, K., et al. (2008), GOSAT Level 1 processing and in-orbit calibration plan, in Sensors, Systems, and Next-Generation Satellites XII, edited by R. Meynart et al., Proc. SPIE, 7106, doi:10.1117/12.800278.

Solow, A. and Nicholls, N. (1990). The relationship between the Southern Oscillation and tropical cyclone frequency in the Australian region. Journal of Climate 3: 1097-1101.

T. Hamazaki, Y. Kaneko, A. Kuze, K. KondoFourier transform spectrometer for greenhouse gases observing satellite (GOSAT). Proceedings of SPIE (2005), p. 73

Tans, P., and R. Keeling, (2014), Trends in Atmospheric Carbon Dioxide. http://www.esrl.noaa.gov/gmd/ccgg/trends/.

Tans, P.P., et al. (Eds.) (1998), Carbon Cycle, in Climate Monitoring and Diagnostics Laboratory No. 24 Summary Report 1996-1997, edited by D.J. Hoffmann et al., chap. 2, pp. 30-51, NOAA Environ. Res. Lab., Boulder Colo. (Data available from http://www.cmdl.noaa.gov/)

Tans, P.P., I. Y. Fung, and T. Takahashi (1990), Observational constrains on the global atmospheric CO2 budget, Science, 23, 1431-1438.

Turner, A. et al. A large increase in US methane emissions over the past decade inferred from satellite data and surface observations. Geophys. Res. Lett. 43, 2218-2224 (2016).

Van der Werf, G. R. et al. Interannual variability in global biomass burning emissions from 1997 to 2004. Atmos. Chem. Phys. 6, 3423-3441 (2006).

Vogel, B. et al. East transport from Southeast Asia boundary layer sources to northern Europe: rapid uplift in typhoons and eastward eddy shedding of the Asian monsoon anticyclone. Atmos. Chem. Phys. 14, 12745-12762 (2014).

Wang, J. et al. El Nino-Southern Oscillation in tropical and mid-latitude column ozone. J. Atmos. Sci. 68, 1911-1921 (2011).

Wang, J., X. Jiang, M. T. Chahine, M. C. Liang, E. T. Olsen, L. Chen, S. Licata, T. Pagano, and Y. L. Yung (2011), The influence of Tropospheric

Biennial Oscillation on mid-tropospheric CO2, Geophys. Res. Lett., 38, L20805, doi:10.1029/2011GL049288."

Wang, J., X. Jiang, M. T. Chahine, M. C. Liang, E. T. Olsen, L. Chen, S. Licata, T. Pagano, and Y. L. Yung (2011), The influence of Tropospheric Biennial

Oscillation in mid-tropospheric CO2, Geophys. Res. Lett., doi:10.1029/2011GL049288.

Wang, Y., et al. (2016), Towards understanding the variability in biospheric CO2 fluxes: using FTIR spectrometry and a chemical transport model to investigate the sources and sinks of carbonyl sulfide and its link to CO2, Atmos. Chem. Phys., 16, 2123-2138.

Warner, J. X. et al. Global carbon monoxide products from combined AIRS, TES, and MLS measurements on A-train satellites. Atmos. Chem. Phys. 14, 103-114 (2014).

Washenfelder, R. A., et al. (2006), Carbon dioxide column abundances at the Wisconsin Tall Tower site, J. Geophys. Res., 111, D22305, doi:10.1029/2006JD007154.

Washenfelder, R. A., G. C. Toon, J.-F. Blavier, Z. Yang, N. T. Allen, P. O. Wennberg, S. A. Vay, D. M. Matross, and B. C. Daube (2006), Carbon dioxide column abundances at the Wisconsin Tall Tower site, J. Geophys. Res., 111, D22305, doi:10.1029/2006JD007154.

Watanabe, H., H. Ishihara, K. Hayashi, F. Kawazoe, N. Kikuchi, N. Eguchi, T. Matsunaga, and T. Yokota (2008), Detailed design of the GOSAT DHF at NIES and data acquisition/processing/distribution strategy, in Sensors, Systems, and Next-Generation Satellites XII, edited by R. Meynart et al., Proc. SPIE, 7106, doi:10.1117/12.801238.

Wentz, F. J., and R. W. Spencer (1998), SSM/I rain retrievals within a unified all-weather ocean algorithm, Journal of Atmospheric Sciences, 55, 1613-1627.

Wernberg, T., Russell, B.D., Moore, P.J., Ling, S.D., Smale, D.A., Campbell, A., Coleman, M.A., Steinberg, P.D., Kendrick, G.A. and Connell, S.D. (2011).

Werner, A. and Holbrook, N.J. (2011). A Bayesian forecast model of Australian region tropical cyclone formation. Journal of Climate 24: 6114-6131.

Wofsy, S. C. et al. HIAPER Pole-to-Pole Observations (HIPPO): fine-grained, global-scale measurements of climatically important atmospheric gases and aerosols. Phil. Trans. R. Soc. A 369, 2073-2086.

Wofsy, S. C., the HIPPO Science Team and Cooperating Modelers and Satellite Teams (2011), HIAPER Pole-to-Pole Observations (HIPPO): fine-grained, global-scale measurements of climatically important atmospheric gases and aerosols, Philosophical Transactions of the Royal Society A, 28, doi:10.1098/rsta.2010.0313.

Wunch, D., et al. (2011), A method for evaluating bias in global measurement of CO2 total columns from space, Atmos. Chem. Phys., 11, 12,317–12,337.

Xiong, X. et al. Characterization and validation of methane products from the Atmospheric Infrared Sounder (AIRS). J. Geophys. Res. 113, doi:10.1029/2007JG000500 (2008).

Xiong, X. et al. Methane Plume over South Asia during the Monsoon Season: Satellite Observation and Model Simulation. Atmos. Chem. Phys. 9, 783-794 (2009).

Xiong, X. et al. Mid-upper tropospheric methane retrieval from IASI and its validation. Atmos. Meas. Tech. 6, 2255-2265 (2013).

Xiong, X. et al. Seven years' observation of mid-upper tropospheric methane from Atmospheric Infrared Sounder. Remote Sensing 2, 2509-2530 (2010).

Xiong, X., Weng, F., Liu, Q. & Olsen, E. Space-borne observation of methane from atmospheric infrared sounder version 6: validation and implications for data analysis. Atmos. Meas. Tech. Discuss. 8, 8563-8597 (2015).

Yokota, T., et al. (2009), Global concentrations of CO2 and CH4 retrieved from GOSAT: First preliminary results, SOLA, 5, 160-163.

Zhang, X. Y. et al. Spatiotemporal variations in mid-upper tropospheric methane over China from satellite observations. Chin. Sci. Bull. 56, 3321–3327 (2011).